Active and Passive Electronic Components

# Metamaterials, Plasmonics, and THz Frequency Photonic Components

Guest Editors: Yalin Lu, Weili Zhang, and Min Qiu

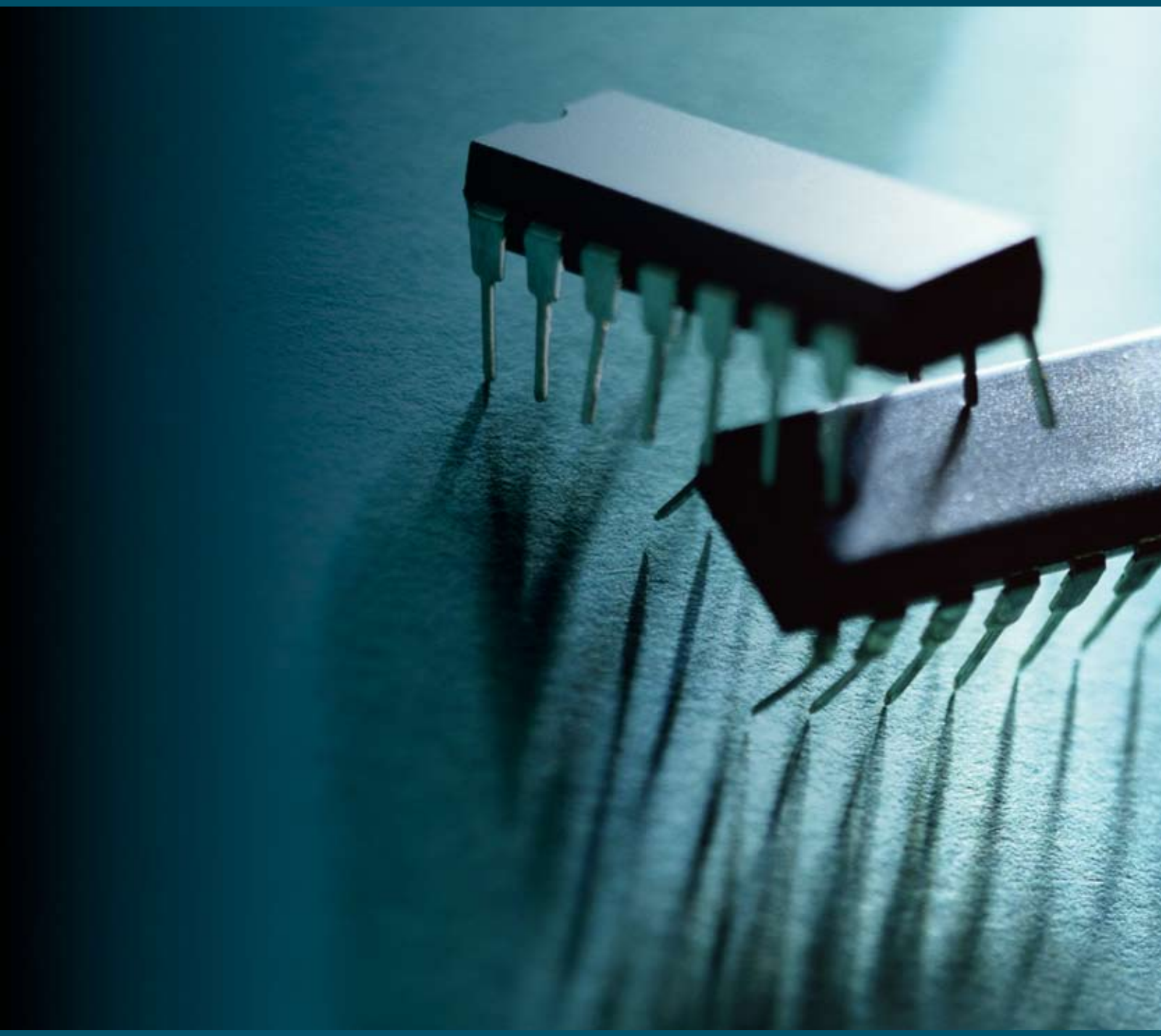

# Metamaterials, Plasmonics, and THz Frequency Photonic Components

# Metamaterials, Plasmonics, and THz Frequency Photonic Components

Guest Editors: Yalin Lu, Weili Zhang, and Min Qiu

# Contents

Hindawi Publishing Corporation
Active and Passive Electronic Components
Volume 2007, Article ID 80839, 2 pages
doi:10.1155/2007/80839

*Editorial*

# Metamaterials, Plasmonics, and THz Frequency Photonic Components

**Yalin Lu,[1] Weili Zhang,[2] and Min Qiu[3]**

[1] *Department of Physics, US Air Force Academy, Colorado Springs, CO 80840, USA*
[2] *School of Electrical and Computer Engineering, Oklahoma State University, Stillwater, OK 74078-5032, USA*
[3] *Department of Microelectronics and Applied Physics, Royal Institute of Technology (KTH), Electrum 229, 164 40 Kista, Sweden*

Received 20 April 2008; Accepted 20 April 2008



An emerging area of interest in application is the terahertz (THz) technology covering the frequency range from 0.1 to 30 THz. Potential applications of such THz technology are widespread, including military security, medical diagnosis, coherent imaging, material analysis, environmental protection, and space science. Development of new photonic components dynamically functioning over such THz frequencies is a subarea of major currently ongoing advanced research effort and is very crucially relying on the availability of new materials, new physical mechanisms, new device designs, and new fabrications/approaches. Effective and efficient integration of new metamaterials with unique surface plasmonic resonance behaviors, for example, could create a full basket of "new-conception" THz photonic components bearing new operation mechanisms including negative refraction, lossless transmission, dynamic tunability, and so forth. In this special issue focusing on both advanced metamaterial research and novel plasmonic study, we have invited a few papers that address such major issues, summarize some of those recent progresses, and discuss those emerging opportunities.

The first paper of this special issue "Plasmonics: manipulating light at the subwavelength scale" by C.-P. Huang and Y.-Y. Zhu summarizes recent progresses in studying surface plasmon-polariton waves, mainly relating to plasmonic waveguide and plasmonic transmission. The former is able to guide the light in a thin metallic surface layer with subwavelength lateral dimensions, and the later to support the enormous transmission when featuring a metal with a subwavelength hole array.

The discussion covers generally the broad photonic spectrum. More focusing, resonant excitation of surface plasmons and the extraordinary transmission specifically over the THz frequencies are reviewed in the second paper "Resonant excitation of terahertz surface plasmons in subwavelength metal holes" by W. Zhang et al. Effect of the hole shape, dimension, material selection, incident electromagnetic (EM) polarization, and metal film thickness on the resonant THz transmission is studied by the state-of-the-art THz time-domain spectroscopy, which reveals an extended potential over even using those poor metals such as lead.

In more details, the third paper "Effects of microstructure variations on macroscopic terahertz metafilm properties" by J. O'Hara et al. discusses the effect of slightly varying the split-ring microstructure design on macroscopic THz metallic film properties including transmission and reflection. This leads the research toward the more practical side on generating new THz photonic component designs as potential optical filters, modulators, and switches.

Moving forward to make THz photonic devices, the fourth paper "Extraordinary transmission and enhanced emission with metallic gratings having converging-diverging channels" by A. Battula et al. investigates the extraordinary transmission behavior when changing the hole from the direct through to a new converging-diverging channel (CDC) shape. By varying the gap size at the throat of the CDC, the spectral locations of the transmission resonance bands can be shifted close to each other and have the transmittance in a very narrow energy band. This indicates a great potential to make THz optical filters having the needed flat-top and narrow transmittance band.

Experimentally, the transmission behavior of THz wave in a one-dimensional metallic grating investigated by the unique time-domain THz spectroscopy is discussed in the fifth paper "Transmission properties of metallic grating with subwavelength slits in THz frequency region" by D. Liang et al. which opens up the potential of making highly polarization-discriminative photonic components.

The next two papers (the sixth and the seventh) "Compact optical waveguides based on hybrid index and surface-plasmon-polariton guidance mechanisms" by M. Yan and M. Qiu, and "Subwavelength-diameter silica wire and photonic crystal waveguide slow light coupling" by Z. Zhang et al. discuss the interesting optical propagation phenomena in two special waveguides: one is defined by a combination of the conventional index confinement and the surface-plasmon-plariton guiding mechanism, and the other is an integration of a subwavelength silica nanowire with a photonic crystal waveguide. The former expects a significant loss reduction when the light is beyond the diffraction limit (using those nanoscale guiding cores for visible wavelengths, e.g.) and the latter for slowing the light for potential applications including compact delay lines for photonic signal processing, dispersion management, and so forth.

The final paper of this special issue "The structural engineering strategy for photonic material research and device development" by Y. Lu actually touches both fabrication and material selection issues during making those THz photonic components, with the goal to enhance the efficiency in both structural and compositional optimizations by using a so-called structural and compositional combinatorial strategy. Details about the strategy are introduced, and its applications in making photonic sensors, dielectric tunable materials, and negative refraction superlattices are also discussed.

*Yalin Lu*
*Weili Zhang*
*Min Qiu*

Hindawi Publishing Corporation
Active and Passive Electronic Components
Volume 2007, Article ID 30946, 13 pages
doi:10.1155/2007/30946

*Review Article*

# Plasmonics: Manipulating Light at the Subwavelength Scale

**Cheng-Ping Huang and Yong-Yuan Zhu**

*National Laboratory of Solid State Microstructures, Nanjing University, Nanjing 210093, China*

Received 21 August 2007; Accepted 10 October 2007

Recommended by Yalin Lu

The coupling of light to collective oscillation of electrons on the metal surface allows the creation of surface plasmon-polariton wave. This surface wave is of central interest in the field of plasmonics. In this paper, we will present a brief review of this field, focusing on the plasmonic waveguide and plasmonic transmission. In the plasmonic waveguide, the light can be guided along the metal surface with subwavelength lateral dimensions, enabling the possibility of high-density integration of the optical elements. On the other hand, in the plasmonic transmission, the propagation of light through a metal surface can be tailored with the subwavelength holes, leading to the anomalous transmission behaviors which have received extensive investigations in recent years. In addition, as a supplement to plasmonics in the visible and near-infrared region, the study of THz plasmonics has also been discussed.



## 1. INTRODUCTION

Microelectronics based on semiconductors and integrated circuits has been well developed, which constructs a strong fundament for various applications, especially the information processing and transmission. However, further development demanded by the information transmission is always limited by the performance of electronic components as, for example, less data can be carried by the electrons. As an alternative, photonics employing the photons as the information carrier may offer a solution to this problem, where the photons travel faster with a larger information capacity. Compared with the electronic counterpart, unfortunately, the conventional photonic components such as the optical fiber are bulky in size (due to the diffraction limit of light), thus setting a great limit to the optical integration. This point holds, even for the photonic crystal, because the period and size of the photonic crystal are usually on the order of the electromagnetic wavelength.

Recently, it has been shown that the trade-off between the capacity and size mentioned above can be overcome by using the surface plasmon-based photonics or plasmonics. The key point is that the electromagnetic wave, which usually travels in a dielectric waveguide, can propagate along the metal surface in the form of surface plasmon-polariton (SPP) mode [1]. As a consequence, the fields can be strongly confined to the metal surface with the lateral dimensions much smaller than the wavelength. Therefore, plasmonic circuits possess both the capacity of photonics and miniaturization of electronics, opening a new way for the future applications [2].

Current interest in plasmonics is, actually, not limited to the investigation of plasmonic circuits. Some novel metallic structures and phenomena, such as the enhanced light transmission through perforated metal films, have also attracted much attention [3, 4], where the SPP modes are usually involved. By employing the highly enhanced plasmon field, a significant enhancement of Raman signal, molecular fluorescence, and nonlinear frequency conversion has been reported [5–7]. And by using the sensitivity of SPP mode to the environment, highly sensitive biosensors can be constructed [8]. Furthermore, plasmonics can also find its potential applications in plasmonic light sources, plasmonic nanolithography, and so on [9, 10].

Here, we review the progress in plasmonics, focusing on the plasmonic waveguide and plasmonic transmission. The paper is organized as follows. In Section 2, we give a simple introduction to the plasmon polariton. In Section 3, the plasmonic waveguide based on various configurations is presented, including the line defect created in periodic metal surface, metal stripe or nanowire, arrays of nanoparticles, and gap waveguide. Employing the gain media to compensate the propagation loss is also mentioned. In Section 4, the plasmonic transmission in various metallic systems, such as a single hole/slit in a metal film, a single hole/slit surrounded

by surface corrugations, and subwavelength hole arrays, has been discussed. And in Section 5, plasmonics of THz frequencies is reviewed, concerning about THz metamaterials, THz SPP mode, and waveguiding in various structures, as well as the THz transmission. A short summary is provided in Section 6.

## 2. PLASMON POLARITON

It is stressed here that it is the metal rather than the dielectric that plays a more important role in the plasmonics. The difference of metal from dielectric lies in not only electrical but also optical properties. In the metal, the presence of huge free electrons gives rise to a unique dielectric response described by the Drude model

$$\varepsilon_m = 1 - \frac{\omega_p^2}{\omega(\omega + i\gamma)}. \quad (1)$$

Here, $\omega_p$ is the bulk plasma frequency and $\gamma$ is the scattering rate of the electrons. For the convenience of discussion, we can neglect the damping of the metal ($\gamma = 0$). It is now clear that when $\omega > \omega_p$, the permittivity is positive and the light can propagate through the metal (with a dispersion relation $\omega^2 = \omega_p^2 + c^2k^2$). This propagating mode, which essentially involves the coupling between light and bulk free electrons, can be termed the bulk plasmon polariton (BPP). Conversely when $\omega < \omega_p$, which is usually satisfied in the considered frequency range, the permittivity is then negative and the light propagation in the metal is forbidden.

It is interesting to find that, even when the permittivity of metal is negative, the propagation of light can be allowed, but in the form of a surface wave on the metal. This is the so-called SPP mode mentioned above. To get knowledge about the character of SPP mode, we take the typical configuration of infinite metal/dielectric interface as an example (see Figure 1). The interaction between light and surface free charges yields, in this case, the following dispersion relation [11]:

$$k_{\text{spp}} = \frac{\omega}{c}\sqrt{\frac{\varepsilon_m\varepsilon_d}{\varepsilon_m + \varepsilon_d}}. \quad (2)$$

Here, $\varepsilon_d$ is the permittivity of dielectric. Notice that, to make $k_{\text{spp}}$ real, we have $\varepsilon_m + \varepsilon_d < 0$, and thus $\omega < \omega_{\text{sp}} \equiv \omega_p/\sqrt{1+\varepsilon_d}$, where $\omega_{\text{sp}}$ is the surface plasmon frequency. This is the frequency range for the existence of this surface mode. For convenience, the dispersion relation of BPP and SPP modes has been plotted schematically in Figure 1. Here, we summarize some features of SPP mode on the flat metal/dielectric interface as follows.

(1) The SPP mode is an electromagnetic wave coupled with the surface electron-density oscillations. The magnetic field of the mode is parallel to the metal surface and perpendicular to the propagation direction (TM mode). Instead, the electric field has both the normal ($E_\perp$) and tangent ($E_{//}$) components. On the dielectric side, $E_\perp/E_{//} = \sqrt{\varepsilon_m/\varepsilon_d}$; on the metal side, $E_\perp/E_{//} = -\sqrt{\varepsilon_d/\varepsilon_m}$. Thus, when the frequency is well below the plasma frequency, the electric field inside the metal is mainly tangent and the electrons move back and forth in the propagation direction, forming a longitudinal electron-density wave.

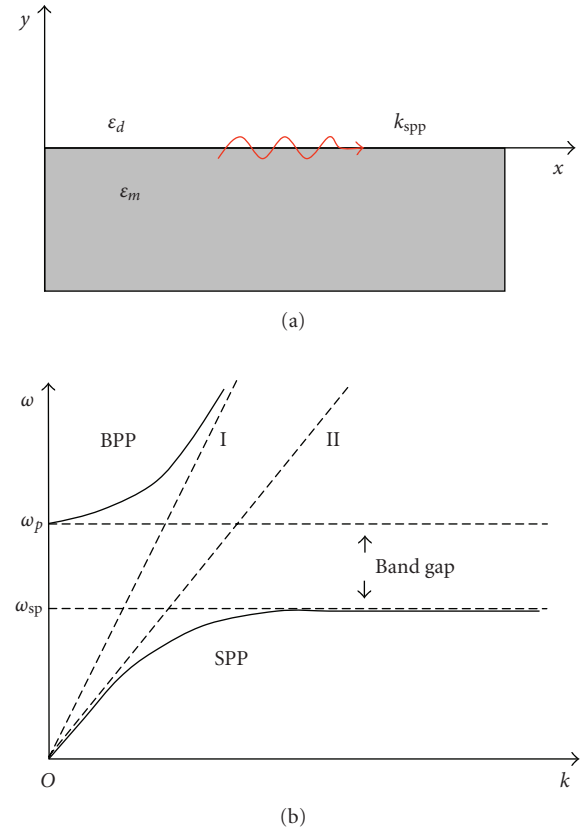


Figure 1: Plasmon-polariton mode associated with the metals: (a) schematic view of infinite metal/dielectric interface; (b) dispersion relation of bulk plasmon-polariton (BPP) and surface plasmon-polariton (SPP) modes. The dashed lines I and II denote the light dispersion $\omega = ck$ and , $\omega = ck/\sqrt{\varepsilon_d}$, respectively. The frequency range between $\omega_{\text{sp}}$ and $\omega_p$ corresponds to a gap where the electromagnetic wave cannot propagate via either bulk or surface modes.

(2) The SPP mode can propagate along the metal surface with a larger propagation constant ($k_{\text{spp}} > k_0\sqrt{\varepsilon_d}$). This means a reduced wavelength as well as a smaller propagation velocity of the electromagnetic wave. Considering of the absorption of the metal, however, the propagation length of SPP mode is finite. A detailed calculation shows that the energy propagation length can be expressed as $L_{\text{spp}} \approx \varepsilon_m'^2/k_0\varepsilon_m''\varepsilon_d^{3/2}$, where $\varepsilon_m'$ and $\varepsilon_m''$ are, respectively, the real and imaginary parts of permittivity of the metal. In the visible and near-infrared region, $L_{\text{spp}}$ is from several to hundreds of micrometers.

(3) The SPP mode is evanescent on either side of the interface due to the larger propagation constant. On the dielectric side, the decaying length of the field is $\delta_d \approx \sqrt{|\varepsilon_m'|}/k_0\varepsilon_d$; on the other side, the decaying length is $\delta_m \approx 1/k_0\sqrt{|\varepsilon_m'|}$. For the interface comprised by silver and glass and free-space wavelength of 800 nm, for example, the obtained decaying lengths are about 300 nm and 25 nm, respectively. This suggests that the wave is strongly confined to the metal surface,

which is just desired in practice. Note that a strong enhancement of fields near the surface can also be achieved.

Due to the larger propagation constant, the SPP mode cannot be excited directly by the incident light. To compensate the wavevector or phase mismatch between the SPP mode and incident light, some special techniques have been introduced [11], such as prism coupling or attenuated total reflection, waveguide coupling using an optical fiber, grating coupling employing the light diffraction, and near-field excitation with a near-field optical microscopy. In addition, a single surface defect, such as surface protuberance and subwavelength hole or slit, may act as an efficient source for the SPP mode [11–13], where some diffraction component or other can ensure the momentum conservation. On the other hand, a direct observation of SPP mode is relatively difficult because of its localized feature. This can be addressed with the use of near-field optical microscopy [14]. It is worthy of noticing that, by structuring the metal surface with nanoscale corrugations, the SPP mode will be scattered and some photons can escape from the surface. Thus the SPP mode can be mapped by recording the scattered light [15]. Recently, a method called fluorescence imaging has been proposed to observe the SPP mode [16], where the metal surface is covered with the fluorescence molecules which emit the radiation with the intensity proportional to the surface electric field. With this method, the reflection, beam splitting, and interference of SPP mode have been successfully observed [17].

It is mentioned that, besides the flat metal/dielectric interface, the SPP mode can also exists in other configurations with some parallel characteristics. As an example, in a thin metal film with the thickness typically of the skin depth, the SPP modes on both sides will couple strongly to each other, giving rise to a long-range SPP mode [18]. In addition, the current research interest in plasmon polariton has been extended from SPP to particle plasmon polariton, where the dimensions of metallic particle are much smaller than the electromagnetic wavelength. A detailed discussion on this topic can be found in [19].

## 3. PLASMONIC WAVEGUIDE

Plasmonic circuit chip would have the ability to have the plasmonic signal generation, transport, modulation, detection, and so forth integrated. And plasmonic waveguide is one of the most important components of plasmonic chip, with which the optical signal can be sent from one section to another. In practice, both smallness of mode profile and largeness of propagation length (or low propagation loss) are desired for a plasmonic waveguide. Although the light can be guided along a planar metal/dielectric interface, the confinement offered is only one-dimensional. Thus different configurations of waveguide have been proposed and investigated.

One method is to employ the plasmonic bandgap effect at the metal surface, with the underlying physics similar to that of a photonic crystal. This is achieved by corrugating the metal surface with the periodic protuberance and creating a line defect. Within a certain wavelength region, the SPP mode can propagate along the line channel but is prohibited from traveling in the periodic structure. With this method, Bozhevolnyi et al. have directly demonstrated the SPP guiding at the wavelength of 782 nm, where 200 nm-wide and 45 nm-high gold scatterers arranged in a triangular lattice of period 400 nm were employed [20]. For a 3.2 $\mu$m-wide line channel, the propagation length of SPP mode is found to be more than 18 $\mu$m. However, the propagation length will be drastically reduced when decreasing the channel width. This trade-off between mode size and propagation length is a basic feature of the plasmonic waveguide. In addition, the waveguiding, in this way, has also been realized at the telecom wavelength 1500 nm recently [21].

The second method is to use the metal stripe or nanowire as the plasmonic waveguide. A metal stripe embedded in a homogeneous dielectric is able to support ultralong-range SPP mode when both thickness and width of the metal film are properly selected (here, the width is much larger than the film thickness) [22]. At the wavelength 1550 nm, the experimentally reported propagation length for the silver waveguide is up to 13.6 mm [23]. This huge propagation length is, however, accompanied by a poor confinement of the mode, which has a spread of several micrometers in lateral dimensions. It is interesting to note that, although the long-range SPP mode is difficult to obtain with a metal stripe embedded in an asymmetric environment [24], a thin metal film sandwiched between a one-dimensional photonic crystal and an arbitrary medium can give rise to a long-range propagation of SPP mode of several millimeters [25]. On the other hand, the metallic nanowire (the width and thickness are both subwavelength) placed on the substrate can also be used to guide the light. Experimentally, a 200 nm-wide and 50 nm-thick gold wire has been fabricated and the propagation of SPP mode locally excited at the wavelength of 800 nm investigated [26]. The results show that the SPP mode is confined to a lateral extension even smaller than the width of nanowire (the full width at half-maximum of the mode is only 115 nm), thus demonstrating waveguiding on a scale below the diffraction limit. This characteristic is useful for realizing high-density integration of the photonic devices. Nonetheless, the subwavelength confinement of metallic nanowire yields a greatly reduced propagation length, which is typically of a few micrometers [26, 27]. Note that the long-range SPP mode also exists in the nanowire with a huge mode size when buried in a dielectric [28].

Cutting the nanowire into nanoparticles provides a third method for the plasmonic waveguiding. In the nanoparticle, an oscillating electric dipole moment can be resonantly excited by the incident light, setting up the particle plasmon-polariton resonance with the fields greatly enhanced and well confined to the particle. The resonance frequency is dependent on the particle shape and size. It was proposed that, when the particles are arranged in a linear chain with the subwavelength particle interspaces, electromagnetic energy transport below the diffraction limit can be reached via near-field coupling along the particle chain [29]. The theoretical prediction has been confirmed experimentally with the waveguide structure consisting of rod-shaped silver particles, where the waveguide was excited by the scan tip of a near-field microscope and energy transport probed with the

fluorescent nanospheres [30]. In this way, a small attenuation length of several hundred nanometers, as a result of high confinement of the fields, has been determined (the source wavelength is 570 nm). The propagation length can be substantially enlarged by using another waveguide structure, which is composed of two-dimensional particle arrays patterned on a silicon wafer [31]. To achieve the transverse confinement along the waveguide plane, a special design of the particle size has been adopted, that is, the particle size is reduced gradually from the center of waveguide to both edges. The plasmon fields are, indeed, concentrated near the waveguide center, showing a lateral confinement of the wavelength scale. Simultaneously, corresponding to the excitation wavelength of 1500 nm, a larger propagation length over 50 $\mu$m has been resulted. It is worthy of mentioning that the energy transport along a linear chain can also be accomplished by employing the magnetic plasmon polariton and split ring resonators [32], where the magnetic rather than electric field interacts strongly with the magnetic dipole moment or electron oscillations taking the form of conduction current in the metallic ring resonators.

Gap waveguide presents another scheme promising for the SPP waveguiding, where the mode is localized in the dielectric region surrounded by the metallic walls. Since the penetration length of electromagnetic fields into the metal is only of the skin depth, the mode profile is mainly determined by the size of dielectric gap. One simple example of gap waveguide is the subwavelength slit, in which the SPP modes on both metal surfaces will be coupled. To obtain two-dimensional confinement, the slit structures can be modified to V-shaped grooves. Numerical simulations has pointed out that, in such a groove, channel plasmon-polariton (CPP) mode confined to the bottom of groove could be supported with a low propagation loss [33]. Recently, V-shaped grooves have been milled into a metal and measurements have confirmed the existence of CPP mode [34]. For a groove with the width 600 nm and depth 1000 nm (the groove angle is about 25°), the propagation length is varying between 90 and 250 $\mu$m relying on the wavelength used (1425~1620 nm). Correspondingly, the full width at half-maximum of the mode is reported to be ~1150 nm, which is subwavelength but larger than the groove width, showing that the CPP mode spreads out of the groove significantly. Using this geometry, various waveguide components, including splitters, interferometers, and ring resonators, have been constructed [35].

Besides the aforementioned semiclosed gap waveguide, the guiding of light can be performed using a transversely closed waveguide structure. For example, a nanocoax similar to the conventional coaxial cable can support near the visible frequency region the plasmon-polariton mode (corresponding to TEM mode for the perfect conductors), which travels in the dielectric medium filled between the inner metallic wire and outer metallic cylinder without a cutoff. Very recently, such a nanocoaxial gap waveguide has been fabricated with the multiwalled carbon nanotube (center conductor with a radius 50 nm), metallic Cr (outer conductor), and the filling medium aluminum oxide (the thickness is 100 nm) [36]. Experimental observations with this subwavelength waveguide have revealed that the propagation length

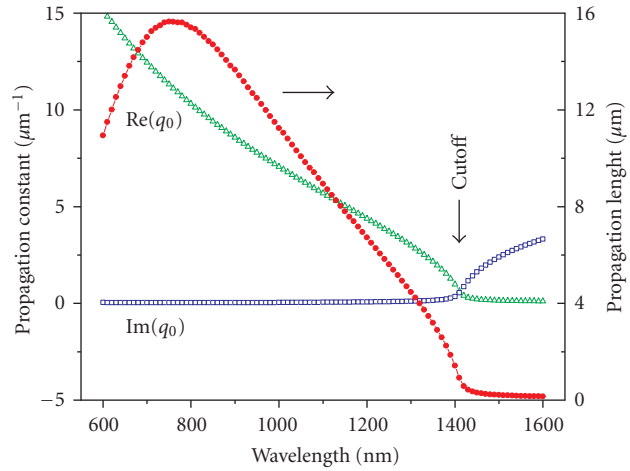


Figure 2: Dependence of the propagation constant and energy propagation length of the fundamental waveguide mode on the wavelength. Here, the opening of the square waveguide (silver) is 400 nm∗400 nm, the permittivity of the filling medium is 2.25; Re($q_0$) and Im($q_0$) represent the real and imaginary parts of the propagation constant, respectively. A maximal propagation length of 15.6 $\mu$m can be achieved at the vacuum wavelength 750 nm.

is of many wavelengths of the incident light (the predicted value is up to 50 $\mu$m, while 6 $\mu$m reported is limited by the fabrication length of the nanocoax). Moreover, rectangular or circular nanoholes similar to the conventional metallic waveguide can also be used to localize and guide the light. To transport the energy more efficiently, the cutoff wavelength of nanohole waveguide can be increased by filling the hole with the dielectric medium. As an example, Figure 2 shows the dependence of propagation constant as well as energy propagation length of a square waveguide on the wavelength ([37, equation (2)] is used here; note that, in the waveguide, the cavity plasmon-polariton mode exists, corresponding to conventional $TE_{01}$ mode). Here, the cross section of a nanohole is assumed to be 400 nm∗400 nm and the permittivity of the filling medium is 2.25 (a thickness of the surrounding silver walls of 100 nm is sufficient for the confinement). It can be seen that the cutoff wavelength is shifted to 1415 nm, below which the propagation of light is allowed, and a maximal energy propagation length up to 15.6 $\mu$m can be achieved at the vacuum wavelength 750 nm.

One major factor that hinders the further applications of plasmonic waveguide is the absorption of metal, allowing the propagation length of SPP mode to be finite. It is lucky that such a problem may be surmounted by replacing the passive dielectric with an active gain medium (the permittivity is $\varepsilon_d = \varepsilon_d' + i\varepsilon_d''$ and $\varepsilon_d'' < 0$) [38]. To elucidate this point, we still take the planar metal/dielectric interface as an example. A simple manipulation of (2), assuming that $\varepsilon_m' \gg \varepsilon_m''$ and $\varepsilon_d' \gg -\varepsilon_d''$, yields

$$k_{\text{spp}}'' = \frac{\omega}{2c} \frac{\varepsilon_m'^2 \varepsilon_d'' + \varepsilon_d'^2 \varepsilon_m''}{\sqrt{\varepsilon_m' \varepsilon_d' (\varepsilon_m' + \varepsilon_d')^3}}. \quad (3)$$

Here, $k''_{\text{spp}}$ represents the imaginary part of propagation constant of the SPP mode. It can be seen that, when $\varepsilon'^2_m\varepsilon''_d + \varepsilon'^2_d\varepsilon''_m = 0$, a lossless propagation of SPP mode can be reached. This corresponds to a gain coefficient $\gamma = -k_0\varepsilon''_d/\varepsilon'^{1/2}_d = k_0\varepsilon''_m\varepsilon'^{3/2}_d/\varepsilon'^2_m$, which is on the order of $1000\,\text{cm}^{-1}$ and can be achieved with the semiconductor-based gain media [38]. Theoretical investigation of gain-assisted SPP propagation has also been extended to metal stripe [38], chains of metal particles [39], and gap waveguide of subwavelength slit [40]. Furthermore, experimental works have been carried out recently, which confirm the existence of the effect [41, 42]. It thus can be expected that plasmonic waveguide combined with appropriate gain medium, owning both subwavelength confinement and (nearly) lossless propagation, could be most promising for the future applications. Further theoretical and experimental works are required.

## 4. PLASMONIC TRANSMISSION

Besides the light propagation along metal surface, the transmission of light through metal surface is another interesting issue. For a screen, such as a metal film, that is, completely opaque, the presence of a small hole may provide an efficient channel for the light. In classic optics, it is well known that, when the hole size is much larger than wavelength, the light will be diffracted into an Airy pattern with the transmission efficiency close to unity, and when the hole diameter is less than the wavelength, an analytical treatment was found to be difficult. Nevertheless, such a small hole of the subwavelength size is of greater interest due to its fundamental as well as practical importance. In 1928, Synge has proposed a new type of microscope (i.e., near-field microscope) [43], in which a small hole with the diameter ~10 nm milled into an opaque screen is required. When illuminating with the incident light, subwavelength resolution may be achieved under the proper conditions. Moreover, in the current optical data-storage technology, data are recorded by employing a lens to focus laser light onto the optical disk. Due to the diffraction limit, the focus spot is usually of the micrometer scale, which prevents the storage density from being further increased. A possible solution is to use a small hole in an opaque screen instead of a lens to transmit the light [44].

It seems that the above proposal will not work well in practice. Besides the fact that the light will be scattered into all directions when emerging from the small hole, the transmission efficiency was predicted to be extremely low. In 1944, Bethe studied the transmission of light through a single subwavelength hole, assuming that the hole is milled in an infinitely thin and perfectly conducting metal film. At normal incidence, the transmission efficiency for the modeled system is deduced to be [45]

$$t_0 = (64/27\pi^2)(kr)^4. \tag{4}$$

Here, $k = 2\pi/\lambda$ is the free-space wavevector and $r$ is the radius of the hole. Indeed, this transmission efficiency scaling with $(r/\lambda)^4$ is very small and it will be further decreased when considering the finite film thickness. Thus the theoretical result sets up a great barrier for the potential applications.

It is lucky that a favorable turn appeared in 1998 when Ebbesen et al. were studying the optical properties of the perforated metal films [3]. They found that a metal film pierced with subwavelength holes can transmit much more light than one will expect, where the transmission efficiency may be larger than unity when normalized to the area of the holes. This enhanced transmission effect has generated great interest in the scientific community. And since then, much effort has been devoted to the transmission properties of various metallic systems, such as a single hole in a metal film, a single hole surrounded by surface corrugations, as well as metal films with various hole arrays, both theoretically and experimentally [4].

The property of a single hole is important for the study of hole arrays. Recently, a single subwavelength hole in an optically thick and freestanding metal film has been fabricated and tested [46], allowing a comparison to the Bethe's theory. It was found that, for either a circular or a rectangular hole, there is a peak in the transmission spectrum, which is in contrast to the monotonous dependence predicted by (4). The results show that the Bethe's theory is insufficient to describe a real metal system. At least, for a metallic waveguide of finite permittivity and thus increased cutoff wavelength [47], the applicability of the theory should be pushed to $\lambda > \lambda_c$, where $\lambda_c$ is the cutoff associated with the real rather than perfect metals. To understand the transmission property of a single hole, one should note that, besides the SPP mode excited on the film surface around the hole [12], there is another SPP mode existing in the subwavelength holes [37, 47–49]. This SPP mode called cylindrical surface plasmons or cavity surface plasmons, originating from coupling of light to electrons on the hole walls, is mainly localized in the dielectric core and travels (propagating or evanescent) along the hole axis. Consequently, the cutoff wavelength of the hole is greatly increased and the photons become easier to pass through the subwavelength holes. On the other hand, it has been shown recently that the transmission peak of the subwavelength hole can be attributed to a Fabry-Perot resonance due to multiple reflections of the fundamental cavity mode [50]. And the position of the main resonance was found to be well close to the cutoff wavelength of the waveguide, for both perfect and real metal films [50, 51].

A single subwavelength slit in a metal film makes a great difference to the single hole, where the fundamental slit mode is propagating with no cutoff. Correspondingly, under the illumination of a TM-polarized wave, multiple transmission peaks will be formed when the slit depth is large enough. This Fabry-Perot-like resonance has been predicted theoretically [52], and experimentally confirmed [53]. Compared with the Fabry-Perot resonance condition ($\lambda = 2t/n$, where $t$ is the slit depth and $n$ is an integer), the transmission peaks of the slit exhibit small redshift due to its different boundary conditions. Further experiment suggested that this wavelength shift is related to the permittivity of metal and that the coupled surface plasmons in the subwavelength slit is involved [54].

Here, the attention should be also paid to the slit-groove structure, which has sparked some discussions recently. It was found experimentally that the far-field radiation of

a single slit can be modulated by the presence of a groove due to the near-field interactions between them [55]. The transmission efficiency oscillates with the slit-groove distance, where the oscillatory amplitude damps initially with the distance and then maintains a constant. To interpret the above behavior, composite-diffracted-evanescent wave (CDEW) model and SPP mechanism have been employed, respectively. It was turned out that the CDEW model can explain qualitatively the initial damping but fails to predict the constant amplitude [55], whereas the SPP model is just on the contrary [56]. A possible solution is that in the near-zone of groove, many diffraction components are involved, but on the surface, only the SPP mode excited ($k_{//} = k_{\mathrm{spp}}$) and a grazing wave ($k_{//} = k_0\sqrt{\varepsilon_d}$) can survive into the far zone. Accordingly, the surface wave originating from the groove and arriving at the slit will interfere with the incident light, leading to the transmission modulation. Similar effect exists in the plasmon-assisted Young's experiment [57]. In contrast to conventional wisdom that the fields at the hole opening are greatly enhanced at the SPP resonance, here, it should be mentioned that the SPP mode will be scattered by the hole, and only a small fraction of SPP can contribute to the light transmission.

The transmission properties of a single subwavelength hole or slit can be further engineered by texturing the metal surface surrounding the hole or slit with periodic corrugations [58–63]. Such a texture can lead to some novel effects in certain wavelength regions, such as the enhanced transmission or beaming of light, depending on which side of the metal film is corrugated. On the one hand, the incoupling of light is associated with the texture on the incident side. When a set of concentric circular (or parallel straight) grooves is added to the input side of the hole (or slit), great enhancement of the light transmission can be obtained [58, 59]. On the other hand, the outcoupling of light is related to the exit side. Correspondingly, when the grooves are made to the output side, highly directional emission from the hole or slit is attainable (the spread angle is only about several degrees) [60, 61]. However, the transmission efficiency (or beam shaping) is not sensitive to the exit (or input) side corrugations. More importantly, when the surface corrugations are fabricated on both sides of the metal film, both collections of incident light and suppression of divergence can be realized efficiently [62, 63]. This high efficiency in coupling in and low divergence in coupling out as well as the small size of the structure, owning the ability to overcome the difficulty aforementioned, have great promise for the applications in, such as subwavelength light sources, near-field optical microscopes, and high-density optical data storage. At present, the physical interpretation of the above phenomena favors a model based on SPP resonance on the textured metal surface [62, 63]. However, further experimental results are not consistent with the SPP model (see [64, Figure 9(b)]). Detailed investigations of the systems revealed that the phenomena are linked to groove cavity mode, light diffraction, and waveguide mode in the slit (or hole) [59, 60], thus possessing a complex physical origin.

In addition, a single subwavelength slit or hole surrounded with surface corrugations can also be used to focus the light [65], where the effect occurs within a narrow frequency range associated with the beaming effect just mentioned. An outstanding property of this subwavelength lens is that the location of the focus is independent on the incident angle. Thus the light impinging from any direction could be focused at the same spot. Moreover, the focus of lens relies on the period and the number of grooves on the exit surface, which can be tailored freely. It is also mentioned that the lens can be constructed with a metal film perorated with subwavelength slits, where the phase retardations of the beams are manipulated by the variant depths or widths of the slits [66, 67].

Now, we come to the subwavelength hole arrays milled in a metal film, which has sparked a renewed interest in surface plasmons that may not be expected initially by Ebbesen et al. [3]. Here, the interest is mainly concentrated on the cases where the film thickness is much larger than the skin depth and the holes do not support the propagating mode. The transmission spectrum of the metal film exhibits a set of maxima and minima, where the peak transmissivity can be orders of magnitude larger than that predicted by Bethe's theory. As an example, Figure 3 presents the measured transmission spectrum (the open circles) of a square hole arrays in a gold film (glass substrate), where the film thickness is 220 nm, the lattice constant is 580 nm, and the hole size is 265 nm$*$265 nm. The transmission efficiency for the longer peak around 945 nm is 26%, corresponding to a transmissivity of 1.25. Compared with the 0.145 estimated from (4), this means a ninefold enhancement of the transmission. Similar results have been demonstrated by many experiments [68]. Subsequent contributions have investigated the influence of physical and geometrical parameters on the transmission spectrum, such as the permittivity of the interface media [69], the thickness of the metal film [70], the shape and size of the holes [71–73], the period of hole arrays [74], the symmetry of the lattice [75], the Fourier coefficients of reciprocal vectors [76, 77], and so on. The variation of these parameters will result in a change of the spectrum shape, the peak or dip positions, or the width and height of the peaks, respectively. Moreover, current investigations have been extended from periodic arrays to quasiperiodic, aperiodic, and other structures [77–79], from optical to lower frequencies [78], and from linear to nonlinear regimes [80].

The experimental works are followed by such questions as, how to simulate the measured transmission spectrum, what the underlying physics could be, and what the role of surface plasmons is. The answers to these questions are of both fundamental and practical importance. The first analytical calculation has assumed a square array of square holes, where the predicted peak width is less than 20% of the measured values [81]. The numerical calculation based on a Fourier modal method is very successful, but the deviation of peak position (or width) between theory and experiment is still up to about 80 nm (or 40%) [71]. It is worthy of noticing that, recently, the performance of simulations has been greatly improved, as shown in [49] for circular holes with a numerical method, and [37] for rectangular holes in an analytical way. On the other hand, the mechanism for enhanced transmission has generated many

debates [37, 49, 64, 81–87]. Original studies have attributed the transmission minima and maxima to Wood's anomaly and SPP resonance, respectively (note that, for the subwavelength slits, the propagating slit mode plays an important role [88]). At normal incidence, they position, respectively, at [68]

$$\lambda_W = \frac{\sqrt{\varepsilon_d}\, d}{\sqrt{m^2 + n^2}}, \qquad \lambda_S = \frac{d}{\sqrt{m^2 + n^2}} \sqrt{\frac{\varepsilon_m \varepsilon_d}{\varepsilon_m + \varepsilon_d}}. \tag{5}$$

Here, $d$ is the period of the square lattice, and $m$ and $n$ are two integers associated with reciprocal vectors (which are used for quasiphase matching for SPP resonance). According to this idea, the main dips around 606 nm and 870 nm in Figure 3 should be due to Wood's anomaly at air and glass interfaces, respectively; correspondingly, the main peaks at 710 nm and 945 nm are the result of SPP resonance on either side of the metal film ($m^2 + n^2 = 1$). This seems to be sound but as is in many cases, a quantitative agreement cannot be found [64]. It is also pointed out that the position of the transmission dip is actually dependent on the permittivity of metal (see inset to Figure 3), thus relating the minima to surface plasmons rather than Wood's anomaly.

Compared with a single hole, the hole arrays hold some different characters. For example, the transmission peak of a single hole is close to the cutoff wavelength, but the peak position for hole arrays is larger than, and usually dependent on, the period [89]. This dependence on the period as well as on the hole size suggests that the enhanced transmission benefits from both extended surface modes (diffraction modes) and localized waveguide mode (cylindrical or cavity surface plasmons). The coupling between them can lead to a strong enhancement of fields near the hole opening, which increases the light transmission. As mentioned previously, the surface plasmons in the nanoholes should be commended, which plays a positive role for the guiding of the energy. But the SPP mode in this occasion deserves a further discussion. We stress that, for a single hole, the SPP mode can be locally excited on the surrounding metal surface at any wavelength. But for hole arrays, the strong excitation of SPP mode is possible only when it is resonant with one of the discrete diffraction modes, which is inherent in the periodic metal surface. Analytical formula shows that the SPP resonance is just corresponding to the transmission minimum [37], which agrees with the experiments (also see the shorter arrows in Figure 3). Thus the SPP mode is of a negative effect in the transmission, consistent with the numerical simulations in one-dimensional slits [82]. In other words, the SPP is positive for the reflection of light, as the transmission minimum is related to the reflection maximum [84]. Nevertheless, the proponent of SPP mechanism has suggested that the dispersion relation of SPP mode on the perforated metal surface has been strongly modified, switching the transmission peak to the larger wavelength. Comparing [74] to [86], where the metal surface and the hole inside have been treated either separately or simultaneously, it seems that there is still a question remaining on the horizon: what is the "true" SPP mode? If the dispersion relation of SPP mode has, indeed, been strongly modified, then the position corresponding to the SPP excitation on a flat (unmodulated) metal surface will point at neither the transmission maximum nor the transmission minimum. This is just in contradiction with the theory and experiments. It turns out to be that the SPP mode on a flat metal surface still survives and acts on the perforated metal films.

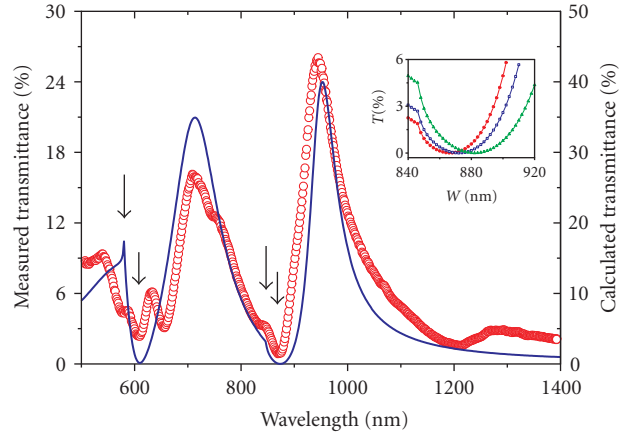


FIGURE 3: Measured (the open circles) and calculated (the solid line) transmission spectra of gold film perforated with square holes (glass substrate), where the lattice constant is 580 nm, the hole side is 265 nm, and the film thickness is 220 nm. The longer and shorter arrows correspond, respectively, to the Wood's anomaly and SPP resonance. The inset shows the evolution of transmission dip (around 870 nm) with the permittivity of metal (the solid circles, open squares, and solid triangles are calculated with a permittivity of −45, −35, and −25, resp.).

Despite the present and forthcoming discussions on the underlying physics of the phenomena, the proposed structures and effects are of great importance for the future applications. The selective transmission property of the hole arrays enables us to build a filter with the size much smaller than a photonic crystal. When the holes are made to be elliptical, a subwavelength polarizer can be constructed [72]. Moreover, by using the subwavelength hole array masks and enhanced light transmission, high-density nanolithography has been proposed and demonstrated [90]. In addition, the enhanced transmission has also been employed to study the photon entanglement [91, 92], which may be useful for quantum information processing. Again, by varying the electric field (or control light) applied to a liquid crystal (or nonlinear polymer) in contact with hole arrays, switching of the transmission spectrum has been demonstrated [93–96]. This controllable transmission character is very promising for the development of active plasmonic devices. And more recently, the interaction between single fluorescent molecules and isolated single holes in a metal film has been studied by Rigneault et al. [97]. Such investigations show that the molecular fluorescence can be enhanced due to an increase in the local excitation intensity, and that Ebbesen has not forgotten his pursuit for more than ten years [44].

## 5. THz PLASMONICS

In previous sections, the surface plasmon polariton, plasmonic waveguiding, and transmission have been reviewed focusing on visible and near-infrared frequency. Actually, the SPP mode and the related phenomena also exist in the low-frequency such as THz and microwave range. Recently, increasing interest has been devoted to the THz band (very far infrared) with the development of efficient THz-wave sources [98]. In practice, the THz radiation is very useful for the applications, such as in biology and medicine, as the vibrational modes of many biomolecules just lie in this frequency band. It can be expected that the combination of THz frequency and plasmonic effect will lead to new THz components and boost the development of THz technology. Since the wavelength of THz radiation is very large compared with the visible and infrared light, some special considerations and designs are required.

As we know, for the most metals, the bulk plasma frequency is in the ultraviolet region of the electromagnetic spectrum due to the large free electron density. As a result, the propagating mode or the bulk plasmon polariton are not present in the metal at the THz frequency. One method to overcome this constraint is to use a metamaterial, with the size of the microstructure much smaller than the wavelength. Pendry has proposed, in 1996, a two-dimensional periodic wire structure, which has an effective dielectric response of the Drude-model type when the electric field is polarized along the metallic wire axis [99]. Due to the dilute electron density and self-inductance effect, the plasma frequency is expressed in this case as $\omega_p = \sqrt{2\pi c^2/a^2 \ln(a/r)}$, where $c$ is the speed of light, $a$ is the lattice constant and $r$ is the wire radius. Then the plasmonic response can be engineered by controlling the geometrical parameters of the structure. With this method, a plasma frequency in the THz range (0.7 THz) has been realized using a metallic wire lattice, having the wire diameter of 30 $\mu m$, lattice constant of 120 $\mu m$ and wire length of 1000 $\mu m$ [100]. The sharp transition of reflection and transmission near the plasma frequency as well as its dependence on the polarization make the structure in the THz optics a high pass filter or a high efficiency polarization filter. Moreover, it has been argued recently that the effective plasma frequency can also be lowered by structuring the metal surface with subwavelength hole arrays [85]. Here the emphasis should be put on a common knowledge that this effective medium response is only valid in the long wavelength limit, which cannot be satisfied in many cases including enhanced light transmission. In addition, based on metallic split-ring resonators as mentioned previously, magnetic response or plasmon polariton has been also realized at the THz frequencies [101]. These plasmonic structures are very important for the construction of THz left-handed medium with both permittivity and permeability to be negative.

In the THz frequency range, the SPP mode on the metal surface is also known as Sommerfeld-Zenneck waves. Due to the lower frequency, the permittivity of metal in this band exhibits a large value (the imaginary part is much larger than the real part). Consequently, for an infinite metal/air interface, the propagation constant given by (2) can be simplified to $k_{spp} \approx k_0 + ik_0/2\varepsilon_m''$. This means a vanishing wavevector mismatch between the SPP mode and a free-space beam as well as a very long propagation length ($L = \varepsilon_m''/k_0 \sim 10^4$ cm). Moreover, the decay length into air is determined to be $\delta = \sqrt{2\varepsilon_m''}/k_0$, which ($\sim$10 cm) is much larger than the wavelength, showing a highly delocalized nature of the mode. Recently, with the edge-diffraction coupling near a razor blade [102] or at the corner of a silicon prism [103], the THz SPP mode on a metal surface has been efficiently excited. Nonetheless, the reported propagation length and mode extension are much less than the theoretical values. This discrepancy between theory and experiment may be attributed to the fact that a true Zenneck wave is difficult to establish due to its unique mode features [104]. To confine and guide this delocalized mode, THz waveguide based on various structures has been proposed and demonstrated. Circular and rectangular metal waveguides are useful but with very high group velocity dispersion near the cutoff wavelength [105], which is not beneficial to the propagation of sub-ps THz pulse. Instead, the parallel-plate metal waveguide can transport the TEM mode with a low loss and without a cutoff. With this geometry, a planar THz interconnect layer using quasioptics and broad bandwidth imaging below the diffraction limit have been demonstrated respectively [106, 107]. As an alternative, the coaxial metal waveguide can also support the TEM mode. Compared with the former case, it presents a better mode confinement but with a higher propagation loss [108]. More importantly, it has been shown that the metal wires can be used for THz waveguiding with the advantages of no dispersion, low attenuation, and simple configuration [109]. For a stainless steel waveguide with a diameter of 0.9 mm, an attenuation coefficient as low as 0.03 $cm^{-1}$ has been reported. Moreover, the theoretical calculations suggest that the attenuation coefficient can be further decreased to 0.002 $cm^{-1}$ if the metallic material and wire radius are optimized [110]. Note that such a metal wire waveguide also suffers from a larger-mode profile and significant radiation loss at wire bends [111].

The localization of THz SPP mode can be substantially improved by using a doped semiconductor surface. As we know, semiconductors have a carrier density several orders of magnitude smaller than that of metals, giving rise to a plasma frequency typically in the THz frequency range. Thus semiconductors behave at the THz frequencies as metals in the optical region. Recently, the propagation of THz SPP mode on gratings of grooves structured on a silicon surface has been demonstrated [112]. Due to Bragg reflection, the dispersion and propagation of surface modes are modified. Especially, a stop band is formed in which the in-plane transmission is prohibited. Moreover, the group velocity of the mode is greatly reduced at the edge of bandgap. It is worthy of noticing that the stop band depends strongly on the carrier density of semiconductors, which can be controlled through direct thermal or optical excitation of free carriers. Consequently, the semiconductor permittivity, the in-plane transmission, and the reflection can be artificially modulated [113, 114]. In contrast to this active control using the semiconductors, previous active plasmonics at the optical frequencies has exploited the structural transformation

of the waveguide material [115]. On the other hand, similar to the perforated metal films discussed previously, semiconductor surface with subwavelength hole arrays can also support enhanced transmission in the THz frequency range [116]. Moreover, when combined with the thermal or optical excitation, efficient switching of the transmission of THz radiation can be realized [117, 118].

Besides the semiconductor surface, a metal surface structured with corrugations can also be employed to concentrate and guide the THz wave. It has been proposed that, when perforated with subwavelength holes or grooves, a unique electromagnetic surface mode can be supported by a real or even perfect metal surface [85, 119–122]. The dispersion relation of this surface mode is similar to that of a semiconductor grating just mentioned [112] as well as the SPP mode on a flat metal surface. Accordingly, this SPP-like surface mode is also called the designer or spoof surface plasmons. A fascinating property of the SPP-like surface mode is that its dispersion relation is mainly determined by the geometry of the structure. Consequently, the coupling of light to a periodic metal surface and the in-plane transmission can be tailored freely. Recently, the propagation of THz surface mode on a perfect metal surface patterned with square holes of finite depth has been demonstrated theoretically [123]. The results also show that, by varying in lateral directions the hole sizes, efficient THz waveguiding with a two-dimensional confinement can be realized. Furthermore, the theoretical study of THz surface mode has been extended to a perfect metallic wire milled with subwavelength grooves [124, 125]. Although a smooth metal wire can support the THz SPP mode with a low propagation loss, the radial size of the mode is very large as mentioned above. The use of a structured metal wire can easily result in both subwavelength confinement and enhanced THz fields. It is interesting to find that, if the groove depth is gradually increased along the wire, the fields can be increasingly confined to the metal surface [124]. And when a conical structure with a constant groove depth is used, superfocusing of the THz radiation to micron-scale volumes may be achieved. This is an important extension of the nanofocusing with a smooth tapered plasmonic waveguide at the optical frequencies [126]. The results make the proposed structure useful in such applications as THz near-field imaging, spectroscopy, and so on.

To conclude this section, we briefly mention the enhanced transmission of THz radiation through a metal surface with subwavelength holes [78, 127–130]. This has been observed with the periodic, quasiperiodic, and aperiodic hole arrays, and the effect of hole shape and size and the geometrical structure factor on the transmission has been revealed. Compared with the spectrum of optical frequencies, the THz transmission exhibits a larger-transmission coefficient and a much narrower-resonance linewidth [128]. When the perforated metal film is connected to a liquid crystal (or fabricated on a semiconductor substrate), switching of the THz transmission with the magnetic field (or visible light) is possible [129, 130]. In addition, the THz transmission through a single hole surrounded by surface corrugations has been studied recently [131]. This type of structure is also promising for the THz near-field imaging with subwavelength resolutions [132].

## 6. CONCLUSIONS

Plasmonics possesses rich novel effects that have not been experienced previously. A deep investigation of these effects may provide us with new insight into plasmonics and yield many more future applications. In this paper, we have presented a simple review of this field, putting the emphasis on the plasmonic waveguiding as well as plasmonic transmission and involving both optical and THz frequencies. Although the current understanding of these effects is not complete or even not substantially correct, the materials presented in many literatures are useful and clue us on how to go ahead. Currently, there are many things left to be done [2]. For example, as a key step towards the plasmonic chip, the realization of plasmonic waveguiding with both subwavelength confinement and ultralow propagation loss is still a great challenge. When the gain medium is to be incorporated in the waveguide, an appropriate fabrication method and a pumping scheme should be investigated [40]. For another example, the use of plasmonics in realizing a new type of light sources such as plasmonic nanolaser has been proposed [133, 134]. But the experimental demonstration of the scheme remains to be accomplished. Finally, we express the belief that there is a huge space for us to design new plasmonic structures and excavate novel plasmonic effects. That needs not only well-drilled theoretical basis and experimental skills but also a creative imagination [135].

## ACKNOWLEDGMENTS

This work was supported by the State Key Program for Basic Research of China (Grant no. 2004CB619003), and the National Natural Science Foundation of China (Grants nos. 10523001 and 10474042).

## REFERENCES

[1] W. L. Barnes, A. Dereux, and T. W. Ebbesen, "Surface plasmon subwavelength optics," *Nature*, vol. 424, no. 6950, pp. 824–830, 2003.

[2] E. Ozbay, "Plasmonics: merging photonics and electronics at nanoscale dimensions," *Science*, vol. 311, no. 5758, pp. 189–193, 2006.

[3] T. W. Ebbesen, H. J. Lezec, H. F. Ghaemi, T. Thio, and P. A. Wolff, "Extraordinary optical transmission through subwavelenght hole arrays," *Nature*, vol. 391, no. 6668, pp. 667–669, 1998.

[4] C. Genet and T. W. Ebbesen, "Light in tiny holes," *Nature*, vol. 445, no. 7123, pp. 39–46, 2007.

[5] S. Nie and S. R. Emory, "Probing single molecules and single nanoparticles by surface-enhanced Raman scattering," *Science*, vol. 275, no. 5303, pp. 1102–1106, 1997.

[6] P. Anger, P. Bharadwaj, and L. Novotny, "Enhancement and quenching of single-molecule fluorescence," *Physical Review Letters*, vol. 96, no. 11, Article ID 113002, 4 pages, 2006.

[7] T. Y. F. Tsang, "Surface-plasmon-enhanced third-harmonic generation in thin silver films," *Optics Letters*, vol. 21, no. 4, pp. 245–247, 1996.

[8] J. Homola, "Present and future of surface plasmon resonance biosensors," *Analytical and Bioanalytical Chemistry*, vol. 377, no. 3, pp. 528–539, 2003.

[9] P. A. Hobson, S. Wedge, J. A. E. Wasey, I. Sage, and W. L. Barnes, "Surface plasmon mediated emission from organic light-emitting diodes," *Advanced Materials*, vol. 14, no. 19, pp. 1393–1396, 2002.

[10] N. Fang, H. Lee, C. Sun, and X. Zhang, "Sub-diffraction-limited optical imaging with a silver superlens," *Science*, vol. 308, no. 5721, pp. 534–537, 2005.

[11] A. V. Zayats, I. I. Smolyaninov, and A. A. Maradudin, "Nano-optics of surface plasmon polaritons," *Physics Reports*, vol. 408, no. 3-4, pp. 131–314, 2005.

[12] L. Yin, V. K. Vlasko-Vlasov, A. Rydh, et al., "Surface plasmons at single nanoholes in Au films," *Applied Physics Letters*, vol. 85, no. 3, pp. 467–469, 2004.

[13] P. Lalanne, J. P. Hugonin, and J. C. Rodier, "Theory of surface plasmon generation at nanoslit apertures," *Physical Review Letters*, vol. 95, no. 26, Article ID 263902, 4 pages, 2005.

[14] B. Hecht, H. Bielefeldt, L. Novotny, Y. Inouye, and D. W. Pohl, "Local excitation, scattering, and interference of surface plasmons," *Physical Review Letters*, vol. 77, no. 9, pp. 1889–1892, 1996.

[15] A. Bouhelier, Th. Huser, H. Tamaru, et al., "Plasmon optics of structured silver films," *Physical Review B*, vol. 63, no. 15, Article ID 155404, 9 pages, 2001.

[16] H. Ditlbacher, J. R. Krenn, N. Felidj, et al., "Fluorescence imaging of surface plasmon fields," *Applied Physics Letters*, vol. 80, no. 3, pp. 404–406, 2002.

[17] H. Ditlbacher, J. R. Krenn, G. Schider, A. Leitner, and F. R. Aussenegg, "Two-dimensional optics with surface plasmon polaritons," *Applied Physics Letters*, vol. 81, no. 10, pp. 1762–1764, 2002.

[18] D. Sarid, "Long-range surface-plasma waves on very thin metal films," *Physical Review Letters*, vol. 47, no. 26, pp. 1927–1930, 1981.

[19] E. Hutter and J. H. Fendler, "Exploitation of localized surface plasmon resonance," *Advanced Materials*, vol. 16, no. 19, pp. 1685–1706, 2004.

[20] S. I. Bozhevolnyi, J. Erland, K. Leosson, P. M. W. Skovgaard, and J. M. Hvan, "Waveguiding in surface plasmon polariton band gap structures," *Physical Review Letters*, vol. 86, no. 14, pp. 3008–3011, 2001.

[21] C. Marquart, S. I. Bozhevolnyi, and K. Leosson, "Near-field imaging of surface plasmon-polariton guiding in band gap structures at telecom wavelengths," *Optics Express*, vol. 13, no. 9, pp. 3303–3309, 2005.

[22] P. Berini, "Plasmon-polariton waves guided by thin lossy metal films of finite width: bound modes of symmetric structures," *Physical Review B*, vol. 61, no. 15, pp. 10484–10503, 2000.

[23] P. Berini, R. Charbonneau, N. Lahoud, and G. Mattiussi, "Characterization of long-range surface-plasmon-polariton waveguides," *Journal of Applied Physics*, vol. 98, no. 4, Article ID 043109, 12 pages, 2005.

[24] P. Berini, "Plasmon-polariton waves guided by thin lossy metal films of finite width: bound modes of asymmetric structures," *Physical Review B*, vol. 63, no. 12, Article ID 125417, 15 pages, 2001.

[25] V. N. Konopsky and E. V. Alieva, "Long-range propagation of plasmon polaritons in a thin metal film on a one-dimensional photonic crystal surface," *Physical Review Letters*, vol. 97, no. 25, Article ID 253904, 4 pages, 2006.

[26] J. R. Krenn, B. Lamprecht, H. Ditlbacher, et al., "Non-diffraction-limited light transport by gold nanowires," *Europhysics Letters*, vol. 60, no. 5, pp. 663–669, 2002.

[27] H. Ditlbacher, A. Hohenau, D. Wagner, et al., "Silver nanowires as surface plasmon resonators," *Physical Review Letters*, vol. 95, no. 25, Article ID 257403, 4 pages, 2005.

[28] K. Leosson, T. Nikolajsen, A. Boltasseva, and S. I. Bozhevolnyi, "Long-range surface plasmon polariton nanowire waveguides for device applications," *Optics Express*, vol. 14, no. 1, pp. 314–319, 2006.

[29] M. Quinten, A. Leitner, J. R. Krenn, and F. R. Aussenegg, "Electromagnetic energy transport via linear chains of silver nanoparticles," *Optics Letters*, vol. 23, no. 17, pp. 1331–1333, 1998.

[30] S. A. Maier, P. G. Kik, H. A. Atwater, et al., "Local detection of electromagnetic energy transport below the diffraction limit in metal nanoparticle plasmon waveguides," *Nature Materials*, vol. 2, no. 4, pp. 229–232, 2003.

[31] S. A. Maier, M. D. Friedman, P. E. Barclay, and O. Painter, "Experimental demonstration of fiber-accessible metal nanoparticle plasmon waveguides for planar energy guiding and sensing," *Applied Physics Letters*, vol. 86, no. 7, Article ID 071103, 3 pages, 2005.

[32] H. Liu, D. A. Genov, D. M. Wu, et al., "Magnetic plasmon propagation along a chain of connected subwavelength resonators at infrared frequencies," *Physical Review Letters*, vol. 97, no. 24, Article ID 243902, 4 pages, 2006.

[33] D. K. Gramotnev and D. F. P. Pile, "Single-mode subwavelength waveguide with channel plasmon-polaritons in triangular grooves on a metal surface," *Applied Physics Letters*, vol. 85, no. 26, pp. 6323–6325, 2004.

[34] S. I. Bozhevolnyi, V. S. Volkov, E. Devaux, and T. W. Ebbesen, "Channel plasmon-polariton guiding by subwavelength metal grooves," *Physical Review Letters*, vol. 95, no. 4, Article ID 046802, 4 pages, 2005.

[35] S. I. Bozhevolnyi, V. S. Volkov, E. Devaux, J.-Y. Laluet, and T. W. Ebbesen, "Channel plasmon subwavelength waveguide components including interferometers and ring resonators," *Nature*, vol. 440, no. 7083, pp. 508–511, 2006.

[36] J. Rybczynski, K. Kempa, A. Herczynski, et al., "Subwavelength waveguide for visible light," *Applied Physics Letters*, vol. 90, no. 2, Article ID 021104, 3 pages, 2007.

[37] C.-P. Huang, Q.-J. Wang, and Y.-Y. Zhu, "Dual effect of surface plasmons in light transmission through perforated metal films," *Physical Review B*, vol. 75, no. 24, Article ID 245421, 7 pages, 2007.

[38] M. P. Nezhad, K. Tetz, and Y. Fainman, "Gain assisted propagation of surface plasmon polaritons on planar metallic waveguides," *Optics Express*, vol. 12, no. 17, pp. 4072–4079, 2004.

[39] D. S. Citrin, "Plasmon-polariton transport in metal-nanoparticle chains embedded in a gain medium," *Optics Letters*, vol. 31, no. 1, pp. 98–100, 2006.

[40] S. A. Maier, "Gain-assisted propagation of electromagnetic energy in subwavelength surface plasmon polariton gap waveguides," *Optics Communications*, vol. 258, no. 2, pp. 295–299, 2006.

[41] J. Seidel, S. Grafström, and L. Eng, "Stimulated emission of surface plasmons at the interface between a silver film and an optically pumped dye solution," *Physical Review Letters*, vol. 94, no. 17, Article ID 177401, 4 pages, 2005.

[42] M. A. Noginov, V. A. Podolskiy, G. Zhu, et al., "Compensation of loss in propagating surface plasmon polariton by gain in adjacent dielectric medium," preprint, 2007 http://arxiv.org/abs/0704.1513.

[43] E. H. Synge, "A suggested method for extending microscopic resolution into the ultra-microscopic region," *Philosophy Magazine*, vol. 6, no. 35, pp. 356–362, 1928.

[44] T. Thio, "A bright future for subwavelength light sources," *American Scientist*, vol. 94, no. 1, pp. 40–47, 2006.

[45] H. A. Bethe, "Theory of diffraction by small holes," *Physical Review*, vol. 66, no. 7-8, pp. 163–182, 1944.

[46] A. Degiron, H. J. Lezec, N. Yamamoto, and T. W. Ebbesen, "Optical transmission properties of a single subwavelength aperture in a real metal," *Optics Communications*, vol. 239, no. 1–3, pp. 61–66, 2004.

[47] R. Gordon and A. G. Brolo, "Increased cut-off wavelength for a subwavelength hole in a real metal," *Optics Express*, vol. 13, no. 6, pp. 1933–1938, 2005.

[48] H. Shin, P. B. Catrysse, and S. Fan, "Effect of the plasmonic dispersion relation on the transmission properties of subwavelength cylindrical holes," *Physical Review B*, vol. 72, no. 8, Article ID 085436, 7 pages, 2005.

[49] N. García and M. Bai, "Theory of transmission of light by subwavelength cylindrical holes in metallic films," *Optics Express*, vol. 14, no. 21, pp. 10028–10042, 2006.

[50] F. J. García-Vidal, E. Moreno, J. A. Porto, and L. Martín-Moreno, "Transmission of light through a single rectangular hole," *Physical Review Letters*, vol. 95, no. 10, pp. 4 pages, 2005.

[51] F. J. García-Vidal, L. Martín-Moreno, E. Moreno, L. K. S. Kumar, and R. Gordon, "Transmission of light through a single rectangular hole in a real metal," *Physical Review B*, vol. 74, no. 15, Article ID 153411, 4 pages, 2006.

[52] Y. Takakura, "Optical resonance in a narrow slit in a thick metallic screen," *Physical Review Letters*, vol. 86, no. 24, pp. 5601–5603, 2001.

[53] F. Yang and J. R. Sambles, "Resonant transmission of microwaves through a narrow metallic slit," *Physical Review Letters*, vol. 89, no. 6, Article ID 063901, 3 pages, 2002.

[54] J. R. Suckling, A. P. Hibbins, M. J. Lockyear, T. W. Preist, J. R. Sambles, and C. R. Lawrence, "Finite conductance governs the resonance transmission of thin metal slits at microwave frequencies," *Physical Review Letters*, vol. 92, no. 14, Article ID 147401, 4 pages, 2004.

[55] G. Gay, O. Alloschery, B. V. de Lesegno, C. O'Dwyer, J. Weiner, and H. J. Lezec, "The optical response of nanostructured surfaces and the composite diffracted evanescent wave model," *Nature Physics*, vol. 2, no. 4, pp. 262–267, 2006.

[56] P. Lalanne and J. P. Hugonin, "Interaction between optical nano-objects at metallo-dielectric interfaces," *Nature Physics*, vol. 2, no. 8, pp. 551–556, 2006.

[57] H. F. Scheuten, N. Kuzmin, G. Dubois, et al., "Plasmon-assisted two-slit transmission: young's experiment revisited," *Physical Review Letters*, vol. 94, no. 5, Article ID 053901, 4 pages, 2005.

[58] T. Thio, K. M. Pellerin, R. A. Linke, H. J. Lezec, and T. W. Ebbesen, "Enhanced light transmission through a single subwavelength aperture," *Optics Letters*, vol. 26, no. 24, pp. 1972–1974, 2001.

[59] F. J. García-Vidal, H. J. Lezec, T. W. Ebbesen, and L. Martín-Moreno, "Multiple paths to enhance optical transmission through a single subwavelength slit," *Physical Review Letters*, vol. 90, no. 21, Article ID 213901, 4 pages, 2003.

[60] L. Martín-Moreno, F. J. García-Vidal, H. J. Lezec, A. Degiron, and T. W. Ebbesen, "Theory of highly directional emission from a single subwavelength aperture surrounded by surface corrugations," *Physical Review Letters*, vol. 90, no. 16, Article ID 167401, 4 pages, 2003.

[61] E. Popov, M. Nevière, A.-L. Fehrembach, and N. Bonod, "Enhanced transmission of light through a circularly structured aperture," *Applied Optics*, vol. 44, no. 32, pp. 6898–6904, 2005.

[62] H. J. Lezec, A. Degiron, E. Devaux, et al., "Beaming light from a subwavelength aperture," *Science*, vol. 297, no. 5582, pp. 820–822, 2002.

[63] A. Degiron and T. W. Ebbesen, "Analysis of the transmission process through single apertures surrounded by periodic corrugations," *Optics Express*, vol. 12, no. 16, pp. 3694–3700, 2004.

[64] H. J. Lezec and T. Thio, "Diffracted evanescent wave model for enhanced and suppressed optical transmission through subwavelength hole arrays," *Optics Express*, vol. 12, no. 16, pp. 3629–3651, 2004.

[65] F. J. García-Vidal, L. Martín-Moreno, H. J. Lezec, and T. W. Ebbesen, "Focusing light with a single subwavelength aperture flanked by surface corrugations," *Applied Physics Letters*, vol. 83, no. 22, pp. 4500–4502, 2003.

[66] Z. Sun and H. K. Kim, "Refractive transmission of light and beam shaping with metallic nano-optic lenses," *Applied Physics Letters*, vol. 85, no. 4, pp. 642–644, 2004.

[67] H. Shi, C. Wang, C. Du, X. Luo, X. Dong, and H. Gao, "Beam manipulating by metallic nano-slits with variant widths," *Optics Express*, vol. 13, no. 18, pp. 6815–6820, 2005.

[68] H. F. Ghaemi, T. Thio, D. E. Grupp, T. W. Ebbesen, and H. J. Lezec, "Surface plasmons enhance optical transmission through subwavelength holes," *Physical Review B*, vol. 58, no. 11, pp. 6779–6782, 1998.

[69] A. Krishnan, T. Thio, T. J. Kim, et al., "Evanescently coupled resonance in surface plasmon enhanced transmission," *Optics Communications*, vol. 200, no. 1–6, pp. 1–7, 2001.

[70] A. Degiron, H. J. Lezec, W. L. Barnes, and T. W. Ebbesen, "Effects of hole depth on enhanced light transmission through subwavelength hole arrays," *Applied Physics Letters*, vol. 81, no. 23, pp. 4327–4329, 2002.

[71] K. J. Klein Koerkamp, S. Enoch, F. B. Segerink, N. F. van Hulst, and L. Kuipers, "Strong influence of hole shape on extraordinary transmission through periodic arrays of subwavelength holes," *Physical Review Letters*, vol. 92, no. 18, Article ID 183901, 4 pages, 2004.

[72] R. Gordon, A. G. Brolo, A. McKinnon, A. Rajora, B. Leathem, and K. L. Kavanagh, "Strong polarization in the optical transmission through elliptical nanohole arrays," *Physical Review Letters*, vol. 92, no. 3, Article ID 037401, 4 pages, 2004.

[73] W. Fan, S. Zhang, B. Minhas, K. J. Malloy, and S. R. J. Brueck, "Enhanced infrared transmission through subwavelength coaxial metallic arrays," *Physical Review Letters*, vol. 94, no. 3, Article ID 033902, 4 pages, 2005.

[74] A. Degiron and T. W. Ebbesen, "The role of localized surface plasmon modes in the enhanced transmission of periodic subwavelength apertures," *Journal of Optics A*, vol. 7, no. 2, pp. S90–S96, 2005.

[75] Q.-J. Wang, J.-Q. Li, C.-P. Huang, C. Zhang, and Y.-Y. Zhu, "Enhanced optical transmission through metal films with rotation-symmetrical hole arrays," *Applied Physics Letters*, vol. 87, no. 9, Article ID 091105, 3 pages, 2005.

[76] Q.-J. Wang, C.-P. Huang, J.-Q. Li, and Y.-Y. Zhu, "Suppression of transmission minima and maxima with structured metal surface," *Applied Physics Letters*, vol. 89, no. 22, Article ID 221121, 3 pages, 2006.

[77] F. Przybilla, C. Genet, and T. W. Ebbesen, "Enhanced transmission through Penrose subwavelength hole arrays," *Applied Physics Letters*, vol. 89, no. 12, Article ID 121115, 3 pages, 2006.

[78] T. Matsui, A. Agrawal, A. Nahata, and Z. V. Vardeny, "Transmission resonances through aperiodic arrays of subwavelength apertures," *Nature*, vol. 446, no. 7135, pp. 517–521, 2007.

[79] J.-Q. Li, W.-Q. Yang, Y.-T. Zhang, Q.-J. Wang, C.-P. Huang, and Y.-Y. Zhu, "Optical transmission through gold film with Archimedean-like subwavelength hole arrays," *Journal of Applied Physics*, vol. 101, no. 7, Article ID 073505, 3 pages, 2007.

[80] J. A. H. van Nieuwstadt, M. Sandtke, R. H. Harmsen, et al., "Strong modification of the nonlinear optical response of metallic subwavelength hole arrays," *Physical Review Letters*, vol. 97, no. 14, Article ID 146102, 4 pages, 2006.

[81] L. Martín-Moreno, F. J. García-Vidal, H. J. Lezec, et al., "Theory of extraordinary optical transmission through subwavelength hole arrays," *Physical Review Letters*, vol. 86, no. 6, pp. 1114–1117, 2001.

[82] Q. Cao and P. Lalanne, "Negative role of surface plasmons in the transmission of metallic gratings with very narrow slits," *Physical Review Letters*, vol. 88, no. 5, Article ID 057403, 4 pages, 2002.

[83] M. M. J. Treacy, "Dynamical diffraction explanation of the anomalous transmission of light through metallic gratings," *Physical Review B*, vol. 66, no. 19, Article ID 195105, 11 pages, 2002.

[84] W. L. Barnes, W. A. Murray, J. Dintinger, E. Devaux, and T. W. Ebbesen, "Surface plasmon polaritons and their role in the enhanced transmission of light through periodic arrays of subwavelength holes in a metal film," *Physical Review Letters*, vol. 92, no. 10, Article ID 107401, 4 pages, 2004.

[85] J. B. Pendry, L. Martín-Moreno, and F. J. García-Vidal, "Mimicking surface plasmons with structured surfaces," *Science*, vol. 305, no. 5685, pp. 847–848, 2004.

[86] P. Lalanne, J. C. Rodier, and J. P. Hugonin, "Surface plasmons of metallic surfaces perforated by nanohole arrays," *Journal of Optics A*, vol. 7, no. 8, pp. 422–426, 2005.

[87] X. Fang, Z. Li, Y. Long, et al., "Surface-plasmon-polariton assisted diffraction in periodic subwavelength holes of metal films with reduced interplane coupling," *Physical Review Letters*, vol. 99, no. 6, Article ID 066805, 4 pages, 2007.

[88] J. A. Porto, F. J. García-Vidal, and J. B. Pendry, "Transmission resonances on metallic gratings with very narrow slits," *Physical Review Letters*, vol. 83, no. 14, pp. 2845–2848, 1999.

[89] C.-P. Huang and Y.-Y. Zhu, "Comment on "Enhanced transmission through periodic arrays of subwavelength holes: the role of localized waveguide resonances"," preprint, 2007, http://arxiv.org/abs/0706.0250.

[90] W. Srituravanich, N. Fang, C. Sun, Q. Luo, and X. Zhang, "Plasmonic nanolithography," *Nano Letters*, vol. 4, no. 6, pp. 1085–1088, 2004.

[91] E. Altewischer, M. P. van Exter, and J. P. Woerdman, "Plasmon-assisted transmission of entangled photons," *Nature*, vol. 418, no. 6895, pp. 304–306, 2002.

[92] S. Fasel, F. Robin, E. Moreno, D. Erni, N. Gisin, and H. Zbinden, "Energy-time entanglement preservation in plasmon-assisted light transmission," *Physical Review Letters*, vol. 94, no. 11, Article ID 110501, 4 pages, 2005.

[93] T. J. Kim, T. Thio, T. W. Ebbesen, D. E. Grupp, and H. J. Lezec, "Control of optical transmission through metals perforated with subwavelength hole arrays," *Optics Letters*, vol. 24, no. 4, pp. 256–258, 1999.

[94] I. I. Smolyaninov, A. V. Zayats, A. Stanishevsky, and C. C. Davis, "Optical control of photon tunneling through an array of nanometer-scale cylindrical channels," *Physical Review B*, vol. 66, no. 20, Article ID 205414, 5 pages, 2002.

[95] G. A. Wurtz, R. Pollard, and A. V. Zayats, "Optical bistability in nonlinear surface-plasmon polaritonic crystals," *Physical Review Letters*, vol. 97, no. 5, Article ID 057402, 4 pages, 2006.

[96] J. Dintinger, I. Robel, P. V. Kamat, C. Genet, and T. W. Ebbesen, "Terahertz all-optical molecule-plasmon modulation," *Advanced Materials*, vol. 18, no. 13, pp. 1645–1648, 2006.

[97] H. Rigneault, J. Capoulade, J. Dintinger, et al., "Enhancement of single-molecule fluorescence detection in subwavelength apertures," *Physical Review Letters*, vol. 95, no. 11, Article ID 117401, 4 pages, 2005.

[98] B. Ferguson and X.-C. Zhang, "Materials for terahertz science and technology," *Nature Materials*, vol. 1, no. 1, pp. 26–33, 2002.

[99] J. B. Pendry, A. J. Holden, W. J. Stewart, and I. Youngs, "Extremely low frequency plasmons in metallic mesostructures," *Physical Review Letters*, vol. 76, no. 25, pp. 4773–4776, 1996.

[100] D. Wu, N. Fang, C. Sun, et al., "Terahertz plasmonic high pass filter," *Applied Physics Letters*, vol. 83, no. 1, pp. 201–203, 2003.

[101] T. J. Yen, W. J. Padilla, N. Fang, et al., "Terahertz magnetic response from artificial materials," *Science*, vol. 303, no. 5663, pp. 1494–1496, 2004.

[102] J. Saxler, J. Gómez Rivas, C. Janke, H. P. M. Pellemans, P. Haring Bolívar, and H. Kurz, "Time-domain measurements of surface plasmon polaritons in the terahertz frequency range," *Physical Review B*, vol. 69, no. 15, Article ID 155427, 4 pages, 2004.

[103] J. O'Hara, R. Averitt, and A. Taylor, "Prism coupling to terahertz surface plasmon polaritons," *Optics Express*, vol. 13, no. 16, pp. 6117–6126, 2005.

[104] T.-I. Jeon and D. Grischkowsky, "THz Zenneck surface wave (THz surface plasmon) propagation on a metal sheet," *Applied Physics Letters*, vol. 88, no. 6, Article ID 061113, 3 pages, 2006.

[105] G. Gallot, S. P. Jamison, R. W. McGowan, and D. Grischkowsky, "Terahertz waveguides," *Journal of the Optical Society of America B*, vol. 17, no. 5, pp. 851–863, 2000.

[106] S. Coleman and D. Grischkowsky, "A THz transverse electromagnetic mode two-dimensional interconnect layer incorporating quasi-optics," *Applied Physics Letters*, vol. 83, no. 18, pp. 3656–3658, 2003.

[107] M. M. Awad and R. A. Cheville, "Transmission terahertz waveguide-based imaging below the diffraction limit," *Applied Physics Letters*, vol. 86, no. 22, Article ID 221107, 3 pages, 2005.

[108] T.-I. Jeon and D. Grischkowsky, "Direct optoelectronic generation and detection of sub-ps-electrical pulses on sub-mm-coaxial transmission lines," *Applied Physics Letters*, vol. 85, no. 25, pp. 6092–6094, 2004.

[109] K. Wang and D. M. Mittleman, "Metal wires for terahertz wave guiding," *Nature*, vol. 432, no. 7015, pp. 376–379, 2004.

[110] Q. Cao and J. Jahns, "Azimuthally polarized surface plasmons as effective terahertz waveguides," *Optics Express*, vol. 13, no. 2, pp. 511–518, 2005.

[111] T.-I. Jeon, J. Zhang, and D. Grischkowsky, "THz Sommerfeld wave propagation on a single metal wire," *Applied Physics Letters*, vol. 86, no. 16, Article ID 161904, 3 pages, 2005.

[112] J. Gómez Rivas, M. Kuttge, P. Haring Bolívar, H. Kurz, and J. A. Sánchez-Gil, "Propagation of surface plasmon polaritons on semiconductor gratings," *Physical Review Letters*, vol. 93, no. 25, Article ID 256804, 4 pages, 2004.

[113] J. Gómez Rivas, M. Kuttge, H. Kurz, P. Haring Bolívar, and J. A. Sánchez-Gil, "Low-frequency active surface plasmon optics on semiconductors," *Applied Physics Letters*, vol. 88, no. 8, Article ID 082106, 3 pages, 2006.

[114] J. Gómez Rivas, J. A. Sánchez-Gil, M. Kuttge, P. Haring Bolívar, and H. Kurz, "Optically switchable mirrors for surface plasmon polaritons propagating on semiconductor surfaces," *Physical Review B*, vol. 74, no. 24, Article ID 245324, 6 pages, 2006.

[115] A. V. Krasavin, A. V. Zayats, and N. I. Zheludev, "Active control of surface plasmon-polariton waves," *Journal of Optics A*, vol. 7, no. 2, pp. S85–S89, 2005.

[116] J. Gómez Rivas, C. Schotsch, P. Haring Bolívar, and H. Kurz, "Enhanced transmission of THz radiation through subwavelength holes," *Physical Review B*, vol. 68, no. 20, Article ID 201306, 4 pages, 2003.

[117] J. Gómez Rivas, P. Haring Bolívar, and H. Kurz, "Thermal switching of the enhanced transmission of terahertz radiation through subwavelength apertures," *Optics Letters*, vol. 29, no. 14, pp. 1680–1682, 2004.

[118] C. Janke, J. Gómez Rivas, P. Haring Bolívar, and H. Kurz, "All-optical switching of the transmission of electromagnetic radiation through subwavelength apertures," *Optics Letters*, vol. 30, no. 18, pp. 2357–2359, 2005.

[119] F. J. García-Vidal, L. Martín-Moreno, and J. B. Pendry, "Surfaces with holes in them: new plasmonic metamaterials," *Journal of Optics A*, vol. 7, no. 2, pp. S97–S101, 2005.

[120] F. J. García de Abajo and J. J. Sáenz, "Electromagnetic surface modes in structured perfect-conductor surfaces," *Physical Review Letters*, vol. 95, no. 23, Article ID 233901, 4 pages, 2005.

[121] M. Qiu, "Photonic band structures for surface waves on structured metal surfaces," *Optics Express*, vol. 13, no. 19, pp. 7583–7588, 2005.

[122] A. P. Hibbins, B. R. Evans, and J. R. Sambles, "Experimental verification of designer surface plasmons," *Science*, vol. 308, no. 5722, pp. 670–672, 2005.

[123] S. A. Maier and S. R. Andrews, "Terahertz pulse propagation using plasmon-polariton-like surface modes on structured conductive surfaces," *Applied Physics Letters*, vol. 88, no. 25, Article ID 251120, 3 pages, 2006.

[124] S. A. Maier, S. R. Andrews, L. Martín-Moreno, and F. J. García-Vidal, "Terahertz surface plasmon-polariton propagation and focusing on periodically corrugated metal wires," *Physical Review Letters*, vol. 97, no. 17, Article ID 176805, 4 pages, 2006.

[125] Y. Chen, Z. Song, Y. Li, et al., "Effective surface plasmon polaritons on the metal wire with arrays of subwavelength grooves," *Optics Express*, vol. 14, no. 26, pp. 13021–13029, 2006.

[126] M. I. Stockman, "Nanofocusing of optical energy in tapered plasmonic waveguides," *Physical Review Letters*, vol. 93, no. 13, Article ID 137404, 4 pages, 2004.

[127] H. Cao and A. Nahata, "Resonantly enhanced transmission of terahertz radiation through a periodic array of subwavelength apertures," *Optics Express*, vol. 12, no. 6, pp. 1004–1010, 2004.

[128] H. Cao and A. Nahata, "Influence of aperture shape on the transmission properties of a periodic array of subwavelength apertures," *Optics Express*, vol. 12, no. 16, pp. 3664–3672, 2004.

[129] C.-L. Pan, C.-F. Hsieh, R.-P. Pan, et al., "Control of enhanced THz transmission through metallic hole arrays using nematic liquid crystal," *Optics Express*, vol. 13, no. 11, pp. 3921–3930, 2005.

[130] E. Hendry, M. J. Lockyear, J. Gómez Rivas, L. Kuipers, and M. Bonn, "Ultrafast optical switching of the THz transmission through metallic subwavelength hole arrays," *Physical Review B*, vol. 75, no. 23, Article ID 235305, 5 pages, 2007.

[131] K. Ishihara, G.-I. Hatakoshi, T. Ikari, H. Minamide, H. Ito, and K. Ohashi, "Terahertz wave enhanced transmission through a single subwavelength aperture with periodic surface structures," *Japanese Journal of Applied Physics*, vol. 44, no. 32, pp. L1005–L1007, 2005.

[132] K. Ishihara, K. Ohashi, T. Ikari, et al., "Terahertz-wave near-field imaging with subwavelength resolution using surface-wave-assisted bow-tie aperture," *Applied Physics Letters*, vol. 89, no. 20, Article ID 201120, 3 pages, 2006.

[133] D. J. Bergman and M. I. Stockman, "Surface plasmon amplification by stimulated emission of radiation: quantum generation of coherent surface plasmons in nanosystems," *Physical Review Letters*, vol. 90, no. 2, Article ID 027402, 4 pages, 2003.

[134] A. K. Sarychev and G. Tartakovsky, "Magnetic plasmonic metamaterials in actively pumped host medium and plasmonic nanolaser," *Physical Review B*, vol. 75, no. 8, Article ID 085436, 9 pages, 2007.

[135] J. B. Pendry, D. Schurig, and D. R. Smith, "Controlling electromagnetic fields," *Science*, vol. 312, no. 5781, pp. 1780–1782, 2006.

Hindawi Publishing Corporation
Active and Passive Electronic Components
Volume 2007, Article ID 40249, 8 pages
doi:10.1155/2007/40249

*Review Article*

# Resonant Excitation of Terahertz Surface Plasmons in Subwavelength Metal Holes

**Weili Zhang,[1] Abul K. Azad,[1,2] and Jiaguang Han[1,3]**

[1] *School of Electrical and Computer Engineering, Oklahoma State University, Stillwater, OK 74078-5032, USA*
[2] *MPA-CINT, Los Alamos National Laboratory, P. O. Box 1663, MS K771, Los Alamos, NM 87545, USA*
[3] *Department of Physics, National University of Singapore, 2 Science Drive 3, Singapore 117542*

Received 27 September 2007; Accepted 12 October 2007

Recommended by Yalin Lu

We present a review of experimental studies of resonant excitation of terahertz surface plasmons in two-dimensional arrays of subwavelength metal holes. Resonant transmission efficiency higher than unity was recently achieved when normalized to the area occupied by the holes. The effects of hole shape, hole dimensions, dielectric function of metals, polarization dependence, and array film thickness on resonant terahertz transmission in metal arrays were investigated by the state-of-the-art terahertz time-domain spectroscopy. In particular, extraordinary terahertz transmission was demonstrated in arrays of subwavelength holes made even from Pb, a generally poor metal, and having thickness of only one-third of skin depth. Terahertz surface plasmons have potential applications in terahertz imaging, biosensing, interconnects, and development of integrated plasmonic components for terahertz generation and detection.



## 1. INTRODUCTION

Recent advance in extraordinary transmission of light has shown that the fascinating properties of two-dimensional (2D) plasmonic arrays of subwavelength holes could lead to breakthrough applications in photonics, nanofabrication, and biochemical sensing. It thus has stimulated extensive research interest in a broad spectral region, in particular, at terahertz frequencies [1–15]. Surface plasmons (SPs) are collective excitations for quantized oscillations of electrons. The resonant interaction between electron-charged oscillations near the surface of metal and the electromagnetic field creates SPs and results in rather unique properties [16]. It was demonstrated that when light passed through periodic subwavelength holes perforated in a metallic film, the observed extraordinary transmission was attributed to resonant excitation of SPs [1, 17]. Light was coupled into the holes in the form of SPs which were squeezed through the holes and then converted back into light on the far side of the holes. Extensive experimental and theoretical studies have been carried out to approach fundamental understanding of this extraordinary transmission and to explore its potential applications in a broad range of disciplines [18–21].

In the terahertz regime, SPs have recently attracted much attention and become an emerging new area [4–15, 22, 23]. SP-enhanced terahertz transmission was observed in subwavelength hole arrays patterned on both metallic films and doped semiconductor slabs. In this article, a review of experimental studies on resonant terahertz transmission in lithographically fabricated 2D metallic arrays of subwavelength holes is presented. Enhanced terahertz transmission in both optically thick and optically thin metallic arrays was experimentally demonstrated. At the primary SP $[\pm 1,0]$ mode, amplitude transmission efficiency of up to nine tenths of the maximum resonant transmission was achieved when a film thickness was only one third of the skin depth [14]. By use of highly reproducible subwavelength arrays, we have demonstrated the effect of dielectric function of metals on transmission properties of terahertz radiation [15]. Additionally, we showed that the enhanced terahertz transmission in the 2D arrays of subwavelength holes resulted from contributions of both SPs and nonresonant transmission [22].

## 2. TERAHERTZ SPs IN METAL ARRAYS

At terahertz frequencies, a drastic increase in the value of dielectric constant $\varepsilon_m = \varepsilon_{\mathrm{rm}} + i\varepsilon_{\mathrm{im}}$ has made most metals

become highly conductive. This has resulted in discrepancies in SP-enhanced terahertz transmission with that in the visible spectral region. Experimental results on transmission properties of light in metallic structures indicated that SP-enhanced transmission is normally achieved in metals with large ratio of the real to the imaginary dielectric constant, $-\varepsilon_{\mathrm{rm}}/\varepsilon_{\mathrm{im}} \gg 1$ [24, 25]. In the terahertz regime, however, this ratio becomes $-\varepsilon_{\mathrm{rm}}/\varepsilon_{\mathrm{im}} < 1$ for nontransition metals such as Ag, Au, Cu, and Al [26]. This was considered as a limitation to realize resonant excitation of terahertz SPs in the 2D hole arrays. A recent theoretical work, however, has shown that an appropriate surface corrugation gives rise to an effective dielectric constant and facilitates the establishment of SPs, even with $-\varepsilon_{\mathrm{rm}}/\varepsilon_{\mathrm{im}} < 1$ [27]. Extraordinary terahertz transmission was observed in subwavelength hole arrays made from both good and poor electrical conductors [15].

### 2.1. Resonant excitation of terahertz SPs in optically thick metal arrays

Resonant transmission of terahertz pulses in optically thick metallic films patterned with subwavelength hole arrays was experimentally demonstrated in a broad terahertz spectral range [4]. Terahertz time-domain spectroscopy (THz-TDS) measurements have revealed enhanced amplitude transmission and a sharp phase peak centered at the SP [±1,0] resonance mode. It was also found that the aperture shape has a remarkable effect on the transmission properties of the 2D hole arrays. Figures 1(a) and 1(b) illustrate the transmitted terahertz pulses and the corresponding amplitude spectra of the reference and the samples. The arrays were lithographically fabricated with 520-nm-thick aluminum film deposited on silicon substrate. Sample A is a square array of 80 $\mu$m ($x$ axis) × 100 $\mu$m ($y$ axis) rectangular holes as shown in the inset of Figure 1(a), while sample B is a square array of 100-$\mu$m-diameter circular holes. The period of these arrays is $L$ = 160 $\mu$m in both 2D directions. The THz-TDS transmission measurements were performed with linearly polarized terahertz ($E//x$) waves impinging on the array at normal incidence [4].

The amplitude transmission and the corresponding phase change are shown in Figures 2(a) and 2(b), respectively. The transmission is obtained from the ratio between the Fourier-transformed sample and the reference amplitudes, whereas the phase change is the phase difference between the sample and the reference spectra. At terahertz frequencies, the dielectric constant of metals is several orders higher than that of dielectric media. Here, $\varepsilon_m = -3.4 \times 10^4 + 1.3 \times 10^6 i$ for aluminum, while $\varepsilon_d = 11.68$ and $\varepsilon_d = 1$ for silicon and air, respectively. Thus the SP modes excited in the array can be approximately given as [4, 28]

$$\omega_{\mathrm{SP}}^{m,n} \cong cG_{mn}\varepsilon_d^{-1/2}, \tag{1}$$

where $G_{mn} = (2\pi/L)(m^2 + n^2)^{1/2}$ is the grating momentum wave vector for 2D square hole arrays, $L$ is the lattice constant of the array, $c$ is the speed of light in vacuum, and $m$ and $n$ are integers of the SP modes. The observed sharp phase peaks centered at the SP resonance modes are indicated by the vertical dashed lines: the metal-Si modes at 0.548 [±1,0] and 0.775 [±1,±1] THz; the metal-air mode [±1,0] at 1.875 THz. Besides samples A and B, a set of arrays with rectangular, square, and circular holes has been measured. We observed that, with the same fundamental period, the hole shape and dimensions can appreciably modify the strengths and shapes of the transmission and the phase change peaks due to the polarization dependent coupling of SPs.

### 2.2. SP-enhanced terahertz transmission in optically thin metallic arrays

So far, resonant excitation of SPs has been widely studied in optically thick 2D hole arrays in a broad spectral range. It is intriguing whether SPs can be excited in optically thin metallic arrays of sub-skin-depth thickness. Here, we demonstrate resonant terahertz transmission through subwavelength hole arrays patterned on metallic films with thicknesses less than a skin depth. Our experimental results have revealed a critical array thickness, above which the SP resonance occurs [14]. The maximum amplitude transmission was achieved when the thickness of metal film approaches a skin depth. However, enhanced terahertz transmission of up to nine tenths of the maximum transmission was realized at a film thickness of only one third of the skin depth at 0.55 THz. This finding may extensively reduce the metal thickness of plasmonic crystals for applications in photonics, optoelectronics, and sensors.

The metallic arrays made from Pb were lithographically fabricated on a silicon wafer (0.64 mm thick $p$-type resistivity $\rho$ = 20 Ωcm) as shown in the inset of Figure 1(a) [4]. The rectangular holes have physical dimensions of 100 $\mu$m × 80 $\mu$m with a lattice constant of 160 $\mu$m. Pb was chosen as the constituent metal of the arrays mainly because of two reasons. First, the extraordinary terahertz transmission in Pb subwavelength hole arrays has been demonstrated with an amplitude efficiency of up to 82% at 0.55 THz, which is close to the performance of arrays made from good electrical conductors such as Ag, Al, and Au [15]. Second, the skin depth of Pb at 0.55 THz is 320 nm, nearly three times of those of Ag and Al. It thus provides a large dynamic range to characterize the evolution of SP resonance at subskin-depth thickness.

The value of skin depth of electromagnetic waves in metal is determined by the penetration distance at which the electric field falls to 1/e. The SPs, which propagate on metal-dielectric interface, decay exponentially in both media. At terahertz frequencies, the complex wave vector inside the metal perpendicular to the interface is approximately given as $k_z = (\omega/c)\varepsilon_m^{1/2}$ [4, 14, 15], where $\omega$ is the angular frequency. Since only the imaginary part of $k_z$ causes the exponential decay of electric fields, the skin depth is defined as $\delta = 1/\mathrm{Im}(k_z) = (c/\omega)\lfloor 1/\mathrm{Im}(\varepsilon_m^{1/2})\rfloor$. Based on this relation, the skin depths for Pb, Al, and Ag at 0.55 THz, the primary SP [±1, 0] resonance are estimated as 320, 110, and 83 nm, respectively.

Pb arrays with various thicknesses ranging from 60 to 1000 nm were prepared. In the THz-TDS measurements, the input terahertz pulses are polarized along the minor axes (80 $\mu$m) of the rectangular holes and penetrate the array at normal incidence. In Figure 3, evolution of SP resonance as

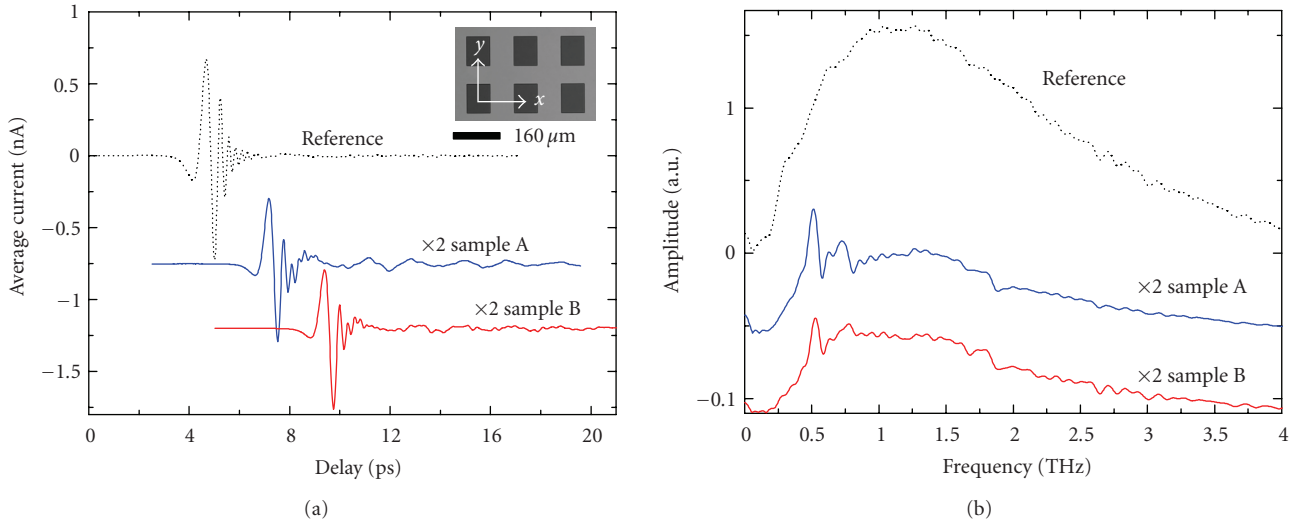


Figure 1: (a) THz-TDS measured transmitted terahertz pulses and (b) the corresponding spectra through the reference and array samples (multiplied by two). The curves in both (a) and (b) are displaced vertically for clarity. Inset: microscopic image of the array.

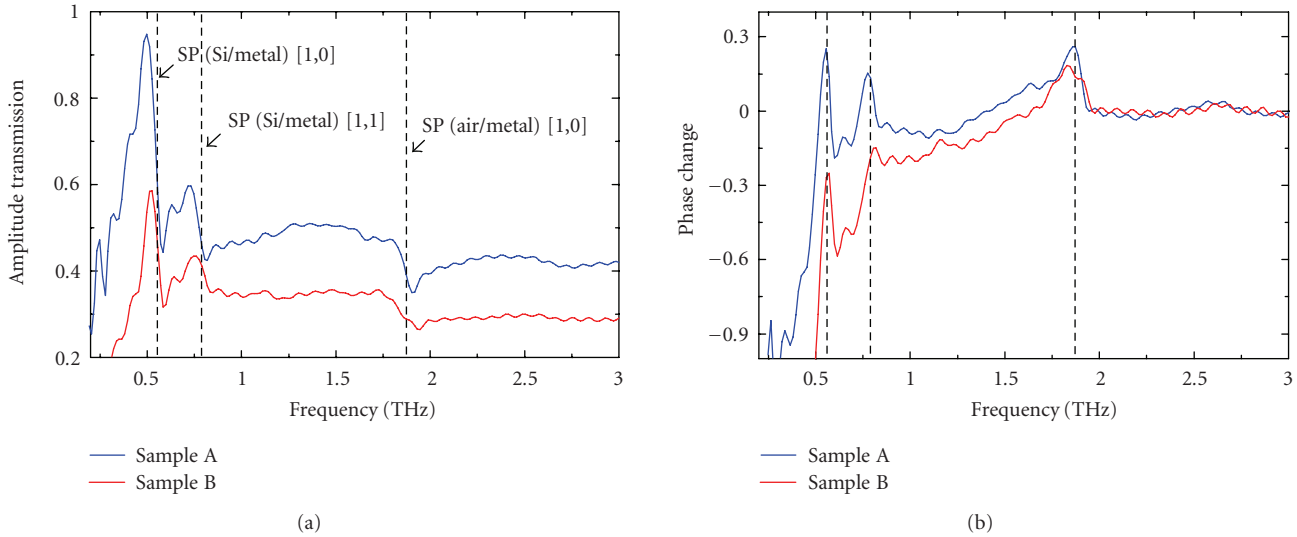


Figure 2: (a) Amplitude transmission of terahertz pulses through the array samples A and B. (b) Corresponding phase change in radians. The dashed lines indicate the SP resonant frequencies.

a function of array film thickness is depicted in the amplitude transmission spectra of various arrays. It clearly reveals two regions of thickness dependence. Below the critical thickness, 64 nm, the frequency-dependent transmission is nearly flat, showing no resonance peak. Above the critical thickness, a resonance at 0.55 THz appears in the transmission, whose amplitude increases with array thickness while the background transmission is reduced at the mean time. This resonance is attributed to the excitation of SPs at the Pb-Si interface. Immediately above the critical thickness, the resonance amplitude is very sensitive to the thickness of arrays. The dependence of peak transmission on array thickness above the critical thickness is shown in Figure 4. The amplitude transmission efficiency increases exponentially when the array thickness is below 100 nm. It then saturates gradually and approaches the maximum at one skin depth [14]. It is worth noting that a transmission efficiency as high as 76% was achieved at array thickness of 100 nm, only one third of skin depth. This value is more than nine tenths of the maximum transmission efficiency achieved at one skin depth. For comparison, we have fabricated two additional arrays of the same structure but made from Ag and Al of one third of skin depth. The measured transmission efficiencies are all above nine tenths of their maximum amplitude transmission.

### 2.3. *Effect of dielectric function of metals on terahertz SPs*

In the visible spectral region, the dielectric function of metals was demonstrated to play a crucial role in the extraordinary transmission in 2D subwavelength hole arrays. Because

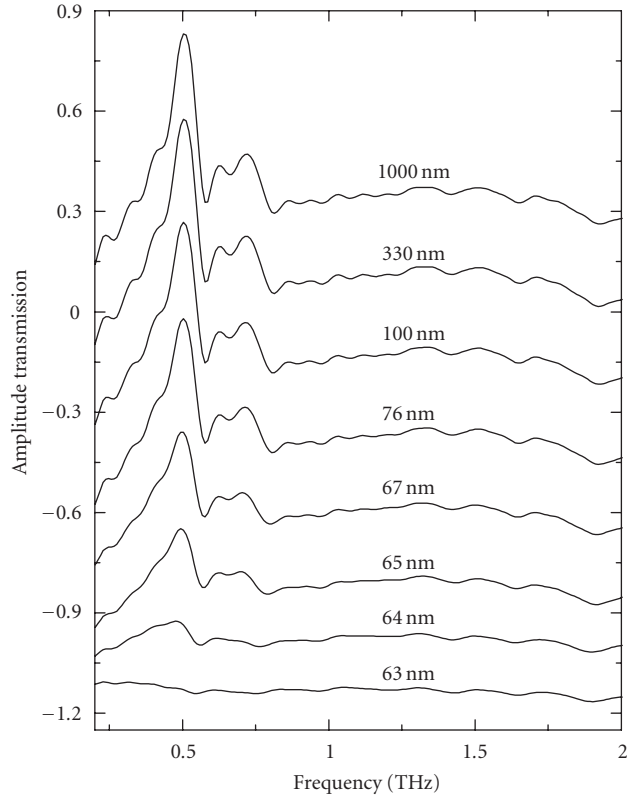


Figure 3: Amplitude transmission of terahertz pulses through the Pb arrays with different film thicknesses. The curves are vertically displaced for clarity.

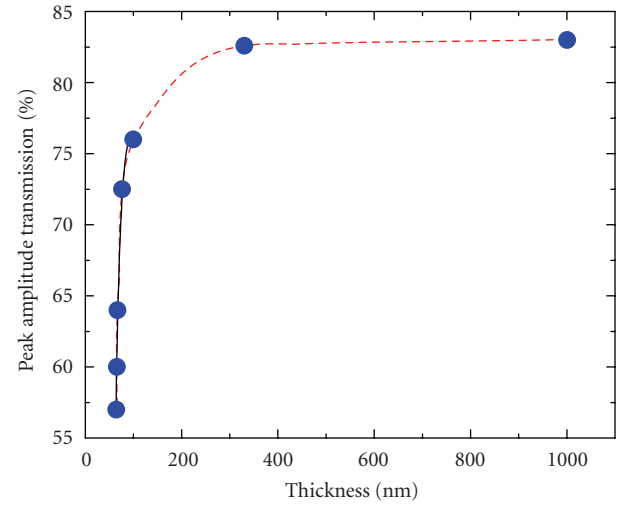


Figure 4: Peak amplitude transmission of the SP [±1,0] mode at 0.55 THz as a function of the Pb thickness (circles). The solid curve is an exponential fit to the data with array thickness below 100 nm. The dashed curve is a guide to the eye.

of a different ratio $-\varepsilon_{rm}/\varepsilon_{im}$, the transmission properties of light showed a large difference in arrays made from different metals [1, 24, 25]. The SP-enhanced transmission efficiency of light was increased with a higher ratio $-\varepsilon_{rm}/\varepsilon_{im}$ [24, 25]. At terahertz frequencies, however, the dielectric constant of metals is several orders of magnitude higher than that at visible frequencies. It is essential to explore how the dielectric function of metals influences extraordinary terahertz transmission in subwavelength structures.

Two types of metallic arrays were lithographically fabricated: array-on-silicon samples with patterned optically thick metal film on blank silicon substrate for the metal-silicon [±1,0] mode 0.55 THz [4, 15]; and freestanding metallic arrays for the metal-air [±1,0] mode 1.60 THz [10, 15]. At 0.55 THz, the ratios $-\varepsilon_{rm}/\varepsilon_{im}$ for Ag, Al, and Pb are 0.12, 0.03, and 0.01, respectively, which indicate that Ag is still a better metal than others and expected to show resonance with higher-amplitude transmission [25]. Realistically, the Ag array indeed shows the highest amplitude transmission 87%, while the Al and Pb arrays follow after with small attenuation, giving 85.5% and 82%, respectively. Even though the amplitude transmission of these arrays shows small difference, it indeed increases with higher ratio $-\varepsilon_{rm}/\varepsilon_{im}$. This result is consistent with those observed at visible frequencies [24, 25].

Compared to excellent metals, Pb is generally considered as a poor electrical conductor. However, the drastic increase in dielectric constant enables Pb to behave as a better metal towards the establishment of SP-enhanced transmission at terahertz frequencies. The measured peak transmissions at the SP [±1,0] resonance 1.60 THz for Ag, Al, and Pb are 82%, 81%, and 72.5%, respectively, showing similar properties as observed at the SP [±1,0] metal-Si resonance 0.55 THz. The difference in amplitude transmission for arrays made from these metals is arisen from the difference in effective propagation length of SPs.

Besides the metal arrays of skin-depth thickness, we have fabricated array-on-silicon samples with different thicknesses to verify the experimental results observed above. Figure 5 presents the peak transmittance measured at the 0.55 [±1,0] THz SP mode for the Ag, Al, and Pb arrays. With metal thicknesses of one-third and three times of skin-depth, the comparison of peak transmittance for different metals remains the same trend as observed with one skin-depth thickness, demonstrating the consistency of our measurements.

The difference in resonant transmission for arrays made from different metals is primarily arisen from the difference in effective propagation length of SPs, determined mainly by internal damping and radiation and scattering damping [3]. At terahertz frequencies, the imaginary propagation vector along the metal-dielectric interface, approximately given as $k_i = k_0\varepsilon_d^{3/2}/(2\varepsilon_{im})$ [4], governs the internal damping, where $k_0$ is the wave vector of electromagnetic wave in vacuum. Figure 6 shows the calculated $k_i$ for SP resonances along both the metal-Si and the metal-air interfaces. The measured transmission of the metal arrays indeed decreases with increasing $k_i$. On a rough metal surface, besides the internal absorption, radiation and scattering damping also modify the propagation length [17]. As a result, the effective propagation lengths for different metals can be extensively reduced, leading to the difference in the resonant transmission.

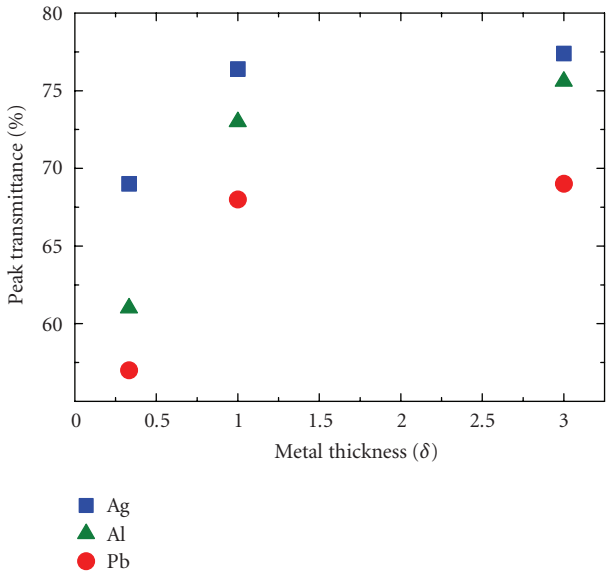


FIGURE 5: Peak transmittance at the 0.55 [±1,0] THz metal-Si mode for arrays made from Ag, Al, and Pb with different metal thicknesses. The arrays are metal on silicon with rectangular holes of dimensions 100 $\mu$m × 80 $\mu$m.

### 2.4. *Coupling between SPs and nonresonant transmission*

SPs excited at the surface of the 2D hole arrays were demonstrated to play a dominant role in extraordinary transmission of electromagnetic waves [1, 17]. The recent studies, however, have revealed that, besides SPs, localized waveguide resonances or localized modes also make contributions to the extraordinary transmission of light in periodic subwavelength holes [29–31]. To better understand the transmission enhancement mechanism in the terahertz regime, we studied hole width-dependent terahertz transmission. A characteristic evolution, including well-regulated change in transmittance, linewidth broadening, and blueshift of peak transmission frequencies with respect to hole width, is experimentally observed [22]. Based on numerical analysis by the Fano model, we found that terahertz transmissions in the 2D hole arrays are associated with two types of contributions: resonant excitation of SPs and nonresonant transmission (or non-SP transmission). The nonresonant transmission exhibits angle-independent peak frequencies and can be resulted from localized effects and direct transmission [22, 23, 29–33]. The localized effects, as either localized modes or localized waveguide resonances [29–31], also contribute substantially to enhanced terahertz transmission. The direct transmission, on the other hand, due to scattering and low filling fraction of metal, is the origin that causes the reduction in transmission efficiency of the holes.

A set of 2D hexagonal arrays of rectangular subwavelength holes are lithographically fabricated with 180-nm-thick Al film onto a silicon wafer (0.64-mm-thick, $p$-type resistivity 20 Ωcm) [22]. Each sample, with dimensions of 15 × 15 mm$^2$, has holes of a fixed length 120 $\mu$m and various widths from 40 to 140 $\mu$m with a 20 $\mu$m interval and a constant lattice period of 160 $\mu$m. Figure 7 illustrates the frequency-dependent absolute transmittance and the corresponding phase change for an array with hole dimensions of 120 × 40 $\mu$m$^2$. At normal incidence, the resonant frequency can be approximately given by (1) with $G_{mn} = 4\pi(m^2 + n^2 + mn)^{1/2}/\sqrt{3}L$, the grating momentum wave vector for the 2D hexagonal hole arrays. The calculated fundamental SP [±1,0] resonance of hexagonal arrays at the Al-Si interface is around 0.63 THz, which is higher than the measured transmission peak 0.49 THz; the latter is a result of both resonant and nonresonant contributions [4, 12, 34].

The transmittance can be analyzed by the Fano model that involves two types of scattering processes: one refers to the continuum direct scattering state as nonresonant transmission, and the other is the discrete resonant state as SPs [23, 34–38]. For an isolated resonance, the Fano model can be written as $T_{\text{fano}}(\omega) = |t(\omega)|^2 = T_a + T_b(\varepsilon_\nu + q_\nu)^2/(1 + \varepsilon_\nu^2)$, where $\varepsilon_\nu = (\omega - \omega_\nu)/(\Gamma_\nu/2)$, $T_a$ is a slowly varying transmittance, and $|T_b|$ is the contribution of a zero-order continuum state that couples with the discrete resonant state. The resonant state is characterized by the resonance frequency $\omega_\nu$, the linewidth $\Gamma_\nu$, and the Breit-Wigner-Fano coupling coefficient $q_\nu$ [23, 34–38]. The Fano model provided a consistent fit to the measured transmittance as shown in Figure 7(a), with a peak transmission at $\omega_\nu/2\pi$ = 0.49 THz and a linewidth $\Gamma_\nu/2\pi$ = 0.16 THz.

The measured transmittance of the arrays with various hole widths from 40 to 140 $\mu$m shown in Figure 8(a) reveals a hole width dependent evolution. An optimal hole width exists (here, is 80 $\mu$m), with which the peak absolute transmittance $T_P$ approaches the maximum value as depicted in Figure 8(b). Meanwhile, the resonance frequency and the corresponding linewidth exhibit monotonic changes. The all-out transmission probability can be obtained by solving the Hamiltonian $\hat{H} = \hat{H}_{\text{SP}} + \hat{H}_{\text{NRT}} + \hat{H}_{\text{Coupling}}$. Hence the coupling can be evaluated by diagonalizing the Hamiltonian matrix [13, 34, 35]

$$H = \hbar \begin{pmatrix} \omega_{\text{SP}} & \chi \\ \chi^* & \omega_{\text{NRT}} \end{pmatrix}, \tag{2}$$

where $\omega_{\text{SP}}$ is the resonance frequency of the SP mode given based on the momentum relationship, $\omega_{\text{NRT}}$ is the frequency of nonresonant transmission, and $\chi$ is the coupling coefficient between SPs and nonresonant transmission. Based on the angle-dependent transmission measurements for each array of different hole widths, the coupling $|\chi|^2$ at each angle of incidence can be solved [22].

Figure 9 shows the calculated coupling strength between the SP mode and nonresonant transmission for arrays with different hole widths at normal incidence. With increasing hole width, the coupling strength shows monotonic change; it is enhanced from $|\chi|^2 = 1.22 \times 10^{-3}$ at 40 $\mu$m to $|\chi|^2 = 6.21 \times 10^{-3}$ at 140 $\mu$m. This further explains the measured characteristic evolution in the transmission spectra of these arrays. The increase in hole width, that corresponds to

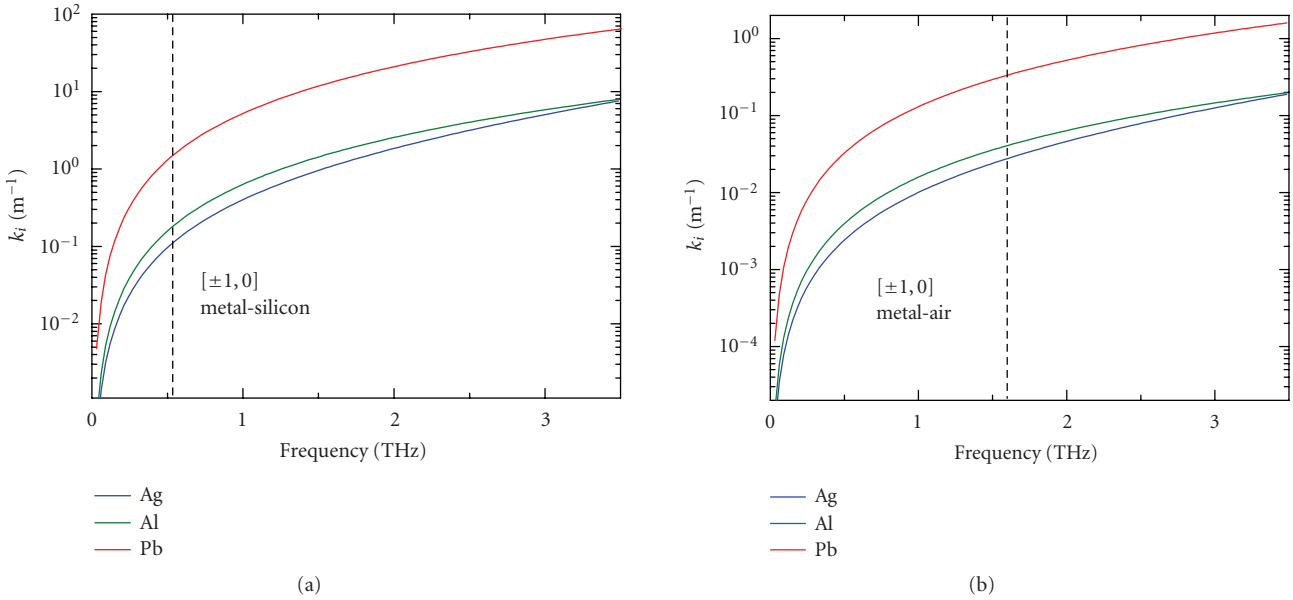


FIGURE 6: Frequency-dependent imaginary propagation vectors of SPs for Ag, Al, and Pb along (a) metal-Si interface and (b) metal-air interfaces.

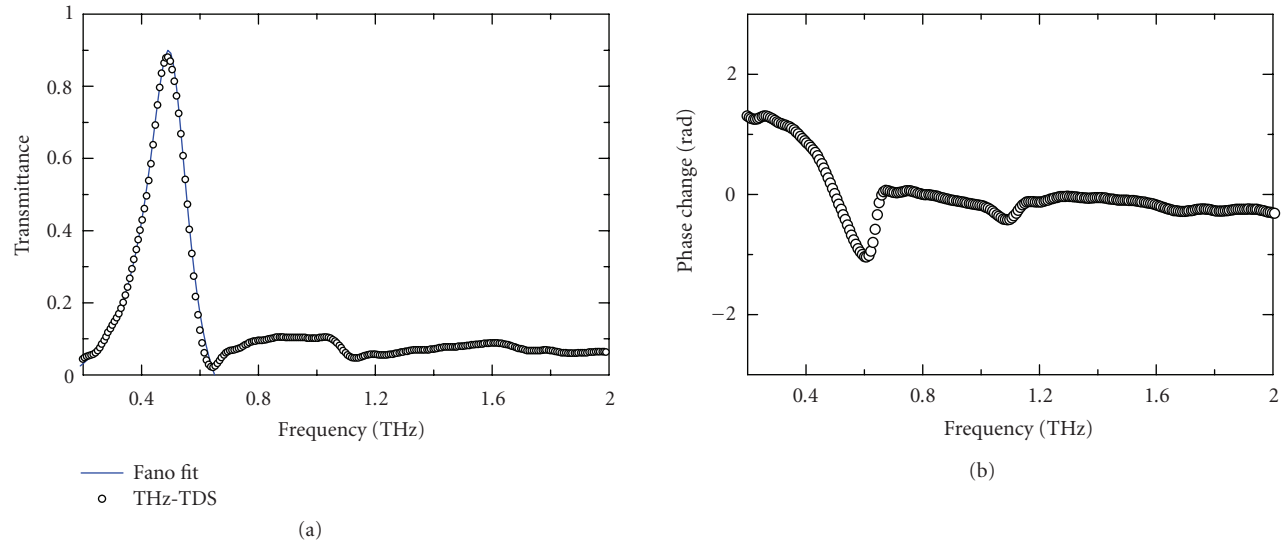


FIGURE 7: (a) Measured (open circles) and theoretical fit (solid curve) by the Fano model of frequency-dependent transmittance of the hexagonal array of 120 × 40 $\mu$m$^2$ holes. The fitting parameters are $q_v = 26.5 \pm 0.2$, $\omega_v/2\pi = 0.49 \pm 0.05$ THz, $\Gamma_v/2\pi = 0.16 \pm 0.01$ THz, and $T_b = (1.28 \pm 0.1) \times 10^{-3}$ for the [±1,0] mode. (b) Corresponding data of phase change.

reduced aspect ratio of holes and lower filling fraction of metal not only leads to increased direct transmission through the holes, but also enhances the coupling between SPs and nonresonant transmission. This, in turn, gives rise to an increased damping of SPs, and thus the linewidth broadens and shifts to higher frequencies towards the peak of nonresonant transmission [23, 29, 32–34]. Another evidence of the effect of direct transmission due to increased hole width is that, when the peak absolute transmittance $T_P$ is normalized by the area of the holes as shown by the circles in Figure 8(b), it exhibits monotonic decrease with increasing hole width.

The maximum absolute peak transmittance $T_P$ achieved at hole width 80 $\mu$m (aspect ratio 3 : 2, filling fraction of metal 62.5%) indicates that the negative effect of direct transmission becomes critical and challenges the dominant role of SPs and localized effects when the hole width is further increased. The contributions of localized effects and direct transmission to the effect of nonresonant terahertz transmission may vary with various hole width (or aspect ratio) and filling fraction of metal. For arrays with filling fraction of metal less than 80%, direct transmission contributes substantially to nonresonant transmission and causes the normalized transition efficiency declined monotonically.

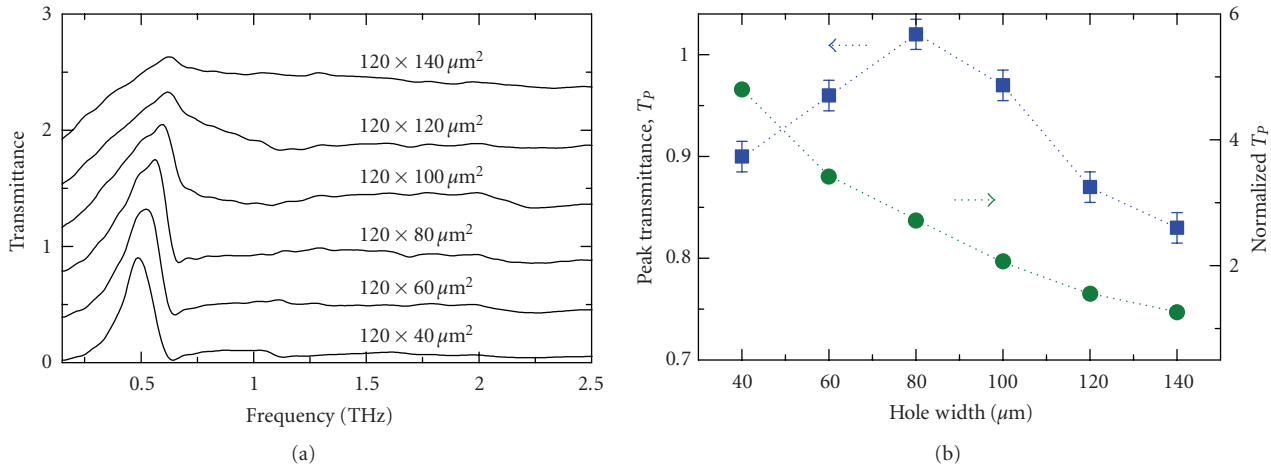


FIGURE 8: (a) Measured absolute transmittance of the hole arrays with fixed hole length of 120 $\mu$m and various hole widths from 40 to 140 $\mu$m. For clarity, the curves are vertically displaced by 0.36. (b) Absolute (squares) and normalized (circles) peak transmittance as a function of hole width. The dotted lines are a guide to the eye.

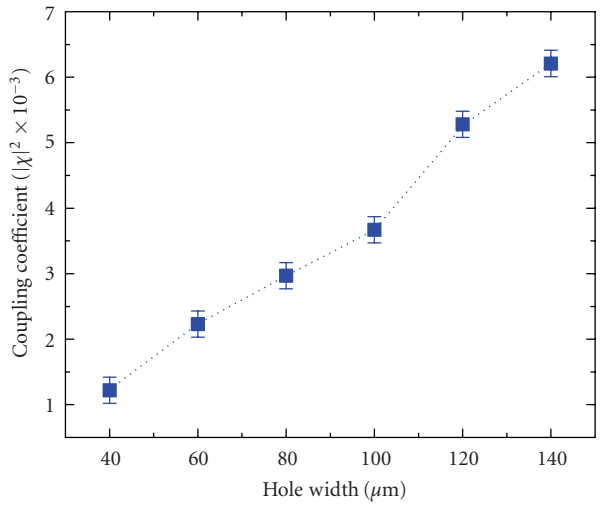


FIGURE 9: Calculated coupling coefficient of the Al-Si SP [±1,0] modes with nonresonant transmission for different hole widths at normal incidence. The dotted line is a guide to the eye.

## 3. CONCLUSION

In conclusion, transmission properties of terahertz pulses through 2D array of subwavelength metal holes were experimentally investigated. Conventional photolithographic process was used to pattern the subwavelength arrays on good and poor metallic conductors. Extraordinary terahertz transmission in such arrays was characterized by broadband THz-TDS measurements. The frequency-dependent resonant transmission in the 2D hole arrays is understood as a consequence of the resonance excitation of SPs at the metal-dielectric interface. We demonstrated the effect of hole shape, hole dimensions, dielectric properties of the metals, polarization dependence, and metal thickness on enhanced terahertz transmission. Rectangular hole shapes were found to show higher resonant transmission when the polarization of the incident terahertz field is perpendicular to the longer axis of the holes. Efficiently enhanced transmission was also observed in optically thin metallic arrays having thickness of one-third of the skin depth. For similar array transmission is higher for the array made from metal having higher electrical conductivity. In addition, the enhanced terahertz transmission in the 2D hole arrays is demonstrated as a result of contributions from both SPs and nonresonant transmission.

## ACKNOWLEDGMENTS

The authors thank D. Qu, D. Grischkowsky, Y. Zhao, M. He, X. Lu, M. Gong, and J. Dai for their outstanding contributions and efforts in this work. This work was partially supported by the National Science Foundation.

## REFERENCES

[1] T. W. Ebbesen, H. J. Lezec, H. F. Ghaemi, T. Thio, and P. A. Wolff, "Extraordinary optical transmission through subwavelength hole arrays," *Nature*, vol. 391, no. 6668, pp. 667–669, 1998.

[2] W. L. Barnes, A. Dereux, and T. W. Ebbesen, "Surface plasmon subwavelength optics," *Nature*, vol. 424, no. 6950, pp. 824–830, 2003.

[3] R. Gordon, A. G. Brolo, A. McKinnon, A. Rajora, B. Leathem, and K. L. Kavanagh, "Strong polarization in the optical transmission through elliptical nanohole arrays," *Physical Review Letters*, vol. 92, no. 3, Article ID 037401, 4 pages, 2004.

[4] D. Qu, D. Grischkowsky, and W. Zhang, "Terahertz transmission properties of thin, subwavelength metallic hole arrays," *Optics Letters*, vol. 29, no. 8, pp. 896–898, 2004.

[5] C. Janke, J. Gómez Rivas, C. Schotsch, L. Beckmann, P. Haring Bolivar, and H. Kurz, "Optimization of enhanced terahertz transmission through arrays of subwavelength apertures," *Physical Review B*, vol. 69, no. 20, Article ID 205314, 5 pages, 2004.

[6] H. Cao and A. Nahata, "Resonantly enhanced transmission of terahertz radiation through a periodic array of subwavelength apertures," *Optics Express*, vol. 12, no. 6, pp. 1004–1010, 2004.

[7] F. Miyamaru and M. Hangyo, "Finite size effect of transmission property for metal hole arrays in subterahertz region," *Applied Physics Letters*, vol. 84, no. 15, pp. 2742–2744, 2004.

[8] J. F. O'Hara, R. D. Averitt, and A. J. Taylor, "Terahertz surface plasmon polariton coupling on metallic gratings," *Optics Express*, vol. 12, no. 25, pp. 6397–6402, 2004.

[9] D. Qu and D. Grischkowsky, "Observation of a new type of THz resonance of surface plasmons propagating on metal-film hole arrays," *Physical Review Letters*, vol. 93, no. 19, Article ID 196804, 4 pages, 2004.

[10] A. K. Azad, Y. Zhao, and W. Zhang, "Transmission properties of terahertz pulses through an ultrathin subwavelength silicon hole array," *Applied Physics Letters*, vol. 86, no. 14, Article ID 141102, 3 pages, 2005.

[11] Q. Xing, S. Li, Z. Tian, et al., "Enhanced zero-order transmission of terahertz radiation pulses through very deep metallic gratings with subwavelength slits," *Applied Physics Letters*, vol. 89, no. 4, Article ID 041107, 3 pages, 2006.

[12] G. Torosyan, C. Rau, B. Pradarutti, and R. Beigang, "Generation and propagation of surface plasmons in periodic metallic structures," *Applied Physics Letters*, vol. 85, no. 16, pp. 3372–3374, 2004.

[13] J.-B. Masson and G. Gallot, "Coupling between surface plasmons in subwavelength hole arrays," *Physical Review B*, vol. 73, no. 12, Article ID 121401, 4 pages, 2006.

[14] A. K. Azad and W. Zhang, "Resonant terahertz transmission in subwavelength metallic hole arrays of sub-skin-depth thickness," *Optics Letters*, vol. 30, no. 21, pp. 2945–2947, 2005.

[15] A. K. Azad, M. He, Y. Zhao, and W. Zhang, "Effect of dielectric properties of metals on terahertz transmission subwavelength hole arrays," *Optics Letters*, vol. 31, no. 17, pp. 2637–2639, 2006.

[16] E. Ozbay, "Plasmonics: merging photonics and electronics at nanoscale dimensions," *Science*, vol. 311, no. 5758, pp. 189–193, 2006.

[17] H. Raether, *Surface Plasmons on Smooth and Rough Surfaces and on Gratings*, chapter 2, Springer, Berlin, Germany, 1988.

[18] W. Srituravanich, N. Fang, C. Sun, Q. Luo, and X. Zhang, "Plasmonic nanolithography," *Nano Letters*, vol. 4, no. 6, pp. 1085–1088, 2004.

[19] X. Luo and T. Ishihara, "Surface plasmon resonant interference nanolithography technique," *Applied Physics Letters*, vol. 84, no. 23, pp. 4780–4782, 2004.

[20] Z.-W. Liu, Q.-H. Wei, and X. Zhang, "Surface plasmon interference nanolithography," *Nano Letters*, vol. 5, no. 5, pp. 957–961, 2005.

[21] A. V. Zayats, J. Elliott, I. I. Smolyaninov, and C. C. Davis, "Imaging with short-wavelength surface plasmon polaritons," *Applied Physics Letters*, vol. 86, no. 15, Article ID 151114, 3 pages, 2005.

[22] J. Han, A. K. Azad, M. Gong, X. Lu, and W. Zhang, "Coupling between surface plasmons and nonresonant transmission in subwavelength holes at terahertz frequencies," *Applied Physics Letters*, vol. 91, no. 7, Article ID 071122, 3 pages, 2007.

[23] W. Zhang, A. K. Azad, J. Han, J. Xu, J. Chen, and X.-C. Zhang, "Direct observation of a transition of a surface plasmon resonance from a photonic crystal effect," *Physical Review Letters*, vol. 98, no. 18, Article ID 183901, 4 pages, 2007.

[24] T. Thio, H. F. Ghaemi, H. J. Lezec, P. A. Wolff, and T. W. Ebbesen, "Surface-plasmon-enhanced transmission through hole arrays in Cr films," *Journal of the Optical Society of America B*, vol. 16, no. 10, pp. 1743–1748, 1999.

[25] D. E. Grupp, H. J. Lezec, T. W. Ebbesen, K. M. Pellerin, and T. Thio, "Crucial role of metal surface in enhanced transmission through subwavelength apertures," *Applied Physics Letters*, vol. 77, no. 11, pp. 1569–1571, 2000.

[26] M. A. Ordal, L. L. Long, R. J. Bell, et al., "Optical properties of the metals Al, Co, Cu, Au, Fe, Pb, Ni, Pd, Pt, Ag, Ti, and W in the infrared and far infrared," *Applied Optics*, vol. 22, no. 7, pp. 1099–1119, 1983.

[27] L. Martín-Moreno, F. J. García-Vidal, H. J. Lezec, A. Degiron, and T. W. Ebbesen, "Theory of highly directional emission from a single subwavelength aperture surrounded by surface corrugations," *Physical Review Letters*, vol. 90, no. 16, Article ID 167401, 4 pages, 2003.

[28] H. J. Lezec and T. Thio, "Diffracted evanescent wave model for enhanced and suppressed optical transmission through subwavelength hole arrays," *Optics Express*, vol. 12, no. 16, pp. 3629–3651, 2004.

[29] K. L. van der Molen, K. J. Klein Koerkamp, S. Enoch, F. B. Segerink, N. F. van Hulst, and L. Kuipers, "Role of shape and localized resonances in extraordinary transmission through periodic arrays of subwavelength holes: experiment and theory," *Physical Review B*, vol. 72, no. 4, Article ID 045421, 9 pages, 2005.

[30] Z. Ruan and M. Qiu, "Enhanced transmission through periodic arrays of subwavelength holes: the role of localized waveguide resonances," *Physical Review Letters*, vol. 96, no. 23, Article ID 233901, 4 pages, 2006.

[31] A. Degiron and T. W. Ebbesen, "The role of localized surface plasmon modes in the enhanced transmission of periodic subwavelength apertures," *Journal of Optics A*, vol. 7, no. 2, pp. S90–S96, 2005.

[32] T. Matsui, A. Agrawal, A. Nahata, and Z. V. Vardeny, "Transmission resonances through aperiodic arrays of subwavelength apertures," *Nature*, vol. 446, no. 7135, pp. 517–521, 2007.

[33] F. J. García de Abajo, J. Sáenz, I. Campillo, and J. Dolado, "Site and lattice resonances in metallic hole arrays," *Optics Express*, vol. 14, no. 1, pp. 7–18, 2006.

[34] W. Fan, S. Zhang, B. Minhas, K. J. Malloy, and S. R. J. Brueck, "Enhanced infrared transmission through subwavelength coaxial metallic arrays," *Physical Review Letters*, vol. 94, no. 3, Article ID 033902, 4 pages, 2005.

[35] C. Genet, M. P. van Exter, and J. P. Woerdman, "Fano-type interpretation of red shifts and red tails in hole array transmission spectra," *Optics Communications*, vol. 225, no. 4–6, pp. 331–336, 2003.

[36] U. Fano, "Effects of configuration interaction on intensities and phase shifts," *Physical Review*, vol. 124, no. 6, pp. 1866–1878, 1961.

[37] M. Sarrazin, J.-P. Vigneron, and J.-M. Vigoureux, "Role of Wood anomalies in optical properties of thin metallic films with a bidimensional array of subwavelength holes," *Physical Review B*, vol. 67, no. 8, Article ID 085415, 8 pages, 2003.

[38] S.-H. Chang, S. K. Gray, and G. C. Schatz, "Surface plasmon generation and light transmission by isolated nanoholes and arrays of nanoholes in thin metal films," *Optics Express*, vol. 13, no. 8, pp. 3150–3165, 2005.

Hindawi Publishing Corporation
Active and Passive Electronic Components
Volume 2007, Article ID 49691, 10 pages
doi:10.1155/2007/49691

*Research Article*

# Effects of Microstructure Variations on Macroscopic Terahertz Metafilm Properties

**John F. O'Hara, Evgenya Smirnova, Abul K. Azad, Hou-Tong Chen, and Antoinette J. Taylor**

*Los Alamos National Laboratory, P.O. Box 1663, MS K771, Los Alamos, NM 87545, USA*

Received 4 September 2007; Accepted 12 October 2007

Recommended by Yalin Lu

The properties of planar, single-layer metamaterials, or metafilms, are studied by varying the structural components of the split-ring resonators used to comprise the overall medium. Measurements and simulations reveal how minor design variations in split-ring resonator structures can result in significant changes in the macroscopic properties of the metafilm. A transmission-line/circuit model is also used to clarify some of the behavior and design limitations of the metafilms. Though our results are illustrated in the terahertz frequency range, the work has broader implications, particularly with respect to filtering, modulation, and switching devices.



## 1. INTRODUCTION

Following its initial theoretical [1, 2] and experimental [3] introductions, metamaterials research has experienced explosive growth and interest. Metamaterials are typically defined as artificial electromagnetic materials comprised of arrays of subwavelength ($\sim\lambda/10$) metallic resonators within or on a dielectric or semiconducting substrate. Due to the small dimensions of the resonators, these composites can be considered effective media [4], and can be quantitatively described by bulk constitutive parameters $\mu(\omega)$, and $\varepsilon(\omega)$, in accordance with the macroscopic form of Maxwell's equations [5, 6]. More recently, the concept of the planar metamaterial, also known as a metafilm or metasurface, has taken on a clearer meaning. A metafilm, as the name implies, is simply a single, planar layer of metamaterial resonator elements [7]. Metafilms can be thought of as the bridge between three-dimensional (3D) metamaterials and the so-called frequency-selective surfaces [8]. The functionality of frequency-selective surfaces is based on the periodicity of the constituent elements, and is described by coherent wave interference concepts such as Bloch waves or Floquet modes [8–10]. Conversely, metafilms function on the same basis as metamaterials; their macroscopic properties depend mostly on the structure of the subwavelength resonators, and not necessarily on their periodic distribution.

While metamaterials promise novel devices and interesting science over very broad frequency bands, the terahertz (THz) spectrum (0.1–4 THz, $\lambda = 75\,\mu$m–3 mm) represents a particularly interesting region. Electronic component technology is only just beginning to develop in the THz and remains extremely immature. Optical approaches to bridge the "THz gap" have met similar difficulty. The cause of this deficiency is a vivid lack of suitable materials from which to form the basic elements crucial to THz technology implementation on a large scale. Despite the numerous possible applications [11–14], presently high-power THz sources, efficient detectors, switches, modulators, filters, and other basic elements are not widely available. Metamaterials are optimistic candidates to correct this problem [15–20]. Additionally, the THz regime also serves as a scale model to investigate the dynamic nature and limitations of higher-frequency metamaterial designs. Continuing THz metamaterials research will become particularly relevant as new fabrication techniques and nanotechnology solutions continue to enable ever smaller resonator structures.

In this paper, we empirically study the microscale structural variations in split-ring resonators and their resulting impact on the macroscale effective properties of metafilms. In addition, we show how lumped-element circuit models can be used in conjunction with transmission-line theory to form an intuitive (though preliminary) analysis tool that could prove useful for designing specific metafilm properties.

Table 1: Unit cell dimensions.

| Sample | All dimensions in $\mu$m | | | | |
|---|---|---|---|---|---|
| | $A_X$ | $A_Y$ | $L_X$ | $L_Y$ | $w$ |
| MF1 | 48 | 14 | 60 | 21 | 6 |
| MF2 | 14 | 48 | 21 | 60 | 6 |
| MF3 | 26 | 26 | 36 | 36 | 6 |
| MF4 | 26 | 26 | 36 | 36 | 8 |
| MF5 | 26 | 26 | 36 | 36 | 8 |
| MF6 | 26 | 26 | 36 | 36 | 8 |
| MF7 | 26 | 26 | 36 | 36 | 8 |

Most of the results shown are based on the simulated behavior of metafilms in THz transmission and reflection. However, we also show experimental transmission results to support the validity of the simulations.

## 2. EXPERIMENT AND SIMULATION

All of the metafilms studied in this work are based on the electric-resonator design [19–22] in which the symmetry of the split-ring resonator is used to eliminate or minimize the magnetic response. While the tuning of both the magnetic and electric metamaterial responses is sometimes desirable, certain applications, such as filtering, can also benefit from these new metamaterials that exhibit a purely electrical response. Our samples were comprised of planar, periodic arrays of electrical split-ring resonators (eSRRs) fabricated on semi-insulating gallium arsenide (SI-GaAs). The sample unit cells are illustrated in Figure 1 and detailed structural dimensions are given in Table 1. We add that the sample linewidths, $d = 2\,\mu$m, and gap spacing, $g = 2\,\mu$m, are equivalent for all samples. Sample fabrication utilized conventional photolithographic techniques in which the metal eSRRs, consisting of 200 nm of gold following 10 nm of titanium, were deposited on the SI-GaAs substrate of 625 $\mu$m thickness. In total there were seven different metafilm designs, designated by the "MF" numbers shown in the figure.

Experimental characterization was performed with terahertz time-domain spectroscopy [23] (THz-TDS) operating in a confocal transmission geometry. A detailed description of this system can be found in [20, 24]. The linearly polarized THz beam was focused to a spot approximately 3 mm ($1/e$) in diameter and propagated normally through the samples. The total sample area of the metafilm was $(1 \times 1)\,\text{cm}^2$ to prevent beam clipping. Measurements were conducted in a dry-air environment to mitigate the effects of water vapor absorption. Transmission measurements were performed on the metafilm samples and, for reference, a bare SI-GaAs substrate of the same thickness. Since the THz measurement is coherent, we directly record the time-varying electric field of the transmitted THz radiation following passage through the sample. Numerical Fourier transformation of the measured time-domain data then permits the extraction of the frequency dependent complex transmission coefficient, $\tilde{t}(\omega) = t(\omega)e^{-j\phi(\omega)}$.

Figures 2 and 3 show the normalized frequency-dependent transmission coefficients, $t_{\text{Meas}}(\omega)$, obtained from our

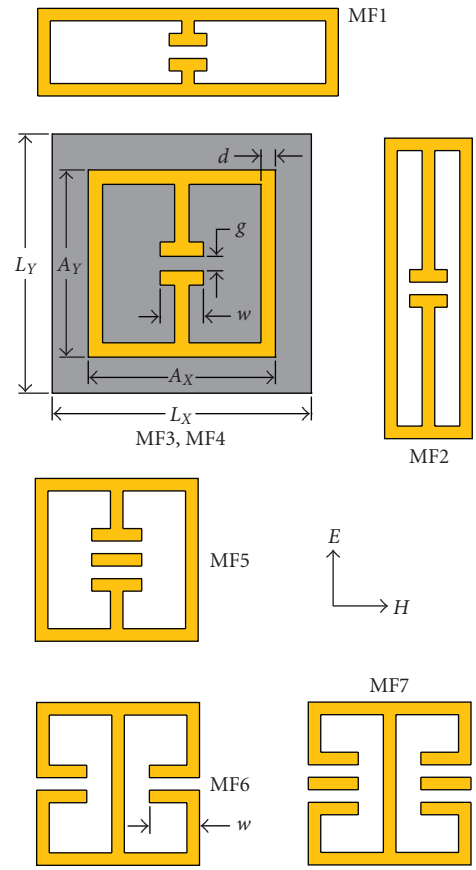


Figure 1: Metafilm unit cells. The dimensions $L_X$ and $L_Y$ specify the $X$ and $Y$ lattice parameters of the rectangular array on which the unit cells are distributed. Gold color indicates metallized regions whereas gray color indicates bare SI-GaAs regions. The THz field polarization is specified by the arrows to the right of MF5. All drawings are shown to scale except for the unit cell representing MF3 and MF4. To clarify dimensioning, this cell was magnified by 15%.

measurements. This data is normalized by dividing the measured transmission spectra of the metafilms, $E_{\text{MF}}(\omega)$, by the measured transmission spectrum of the reference substrate, $E_R(\omega)$, such that $t_{\text{Meas}}(\omega) = |\tilde{t}_{\text{Meas}}(\omega)| = |E_{\text{MF}}(\omega)/E_R(\omega)|$. All of the samples clearly exhibit a strongly resonant behavior between 0.5 and 1.1 THz in response to the electromagnetic field.

To further our understanding of the data, we performed simulations of the electromagnetic response of the metamaterials using commercially available finite-element software [25]; the results are shown in Figures 2 and 3. While simulations were set up to mimic the experimental conditions, some adjustments are necessary to properly compare the two.

These adjustments begin by recognizing that, in simulation, the substrate has an effectively infinite thickness to avoid Fabry-Perot (multiple reflection) effects in the frequency domain analysis. Therefore, simulated transmission coefficients are obtained by measuring the transmitted electric fields directly inside the GaAs, an obvious impossibility in our measurements. Instead our measured data must be divided by (or normalized to) a reference spectrum. This

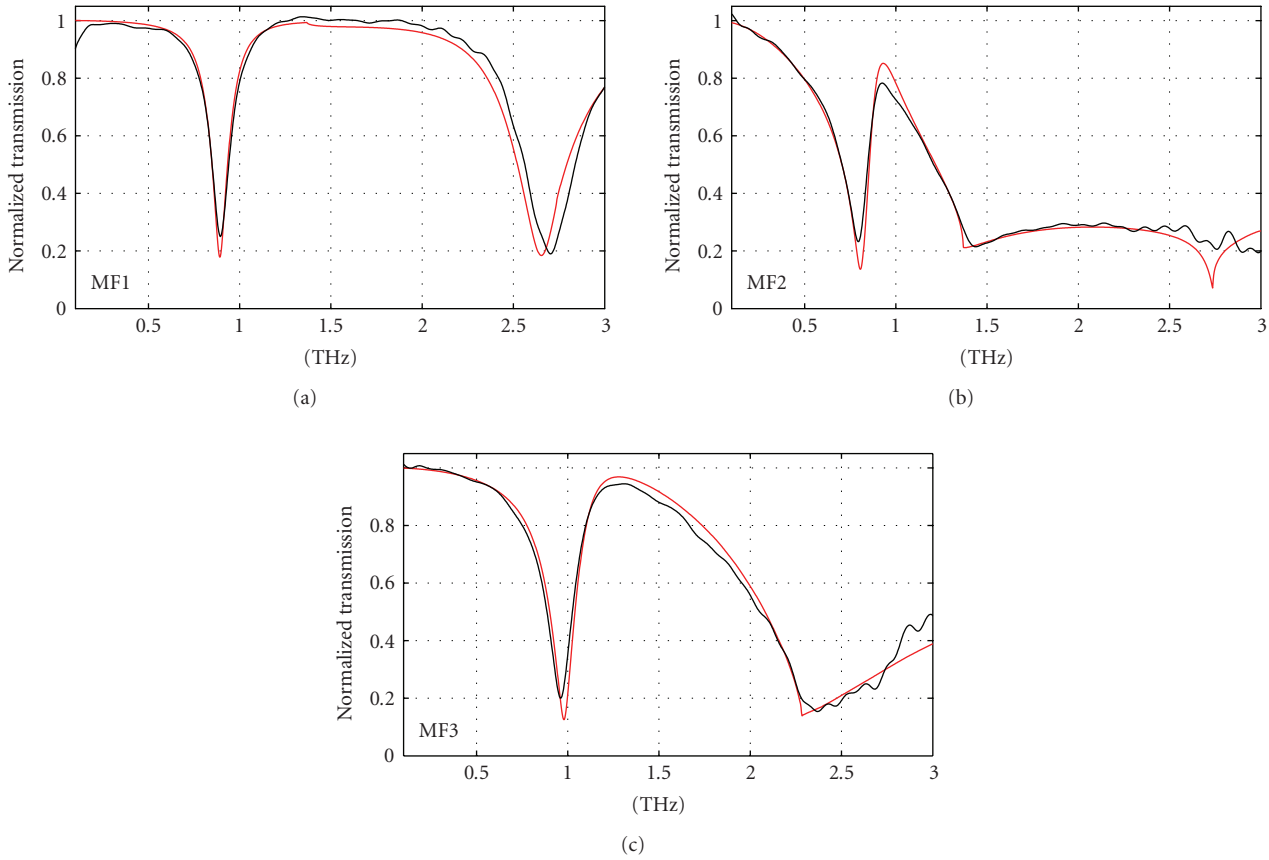


FIGURE 2: Normalized transmission through metafilm samples MF1, MF2, and MF3. Black curves indicate measured data while red curves show simulation results.

process isolates the response of the metafilm from the substrate by removing their common effects, such as Fresnel reflections from the back face. We add that Fabry-Perot effects can also be ignored in our measured data because our time-domain system allows us to "gate out" later arriving pulses. To quantify this data extraction procedure, we write out the expressions for the transmitted fields as a function of the input field, $E_0$. For the bare reference substrate, the measured field, $E_R$, is determined by the transmission coefficients at the front and back faces:

$$E_R(\omega) = E_0 \frac{2Z_G}{Z_G + Z_0} \frac{2Z_0}{Z_G + Z_0}, \tag{1}$$

where $Z_G = 103\,\Omega$ is the impedance of the GaAs substrate and $Z_0 = 377\,\Omega$ is the impedance of free space. We have omitted the phase term associated with wave propagation through the substrate as this is common to the sample and reference measurements. For the metafilm samples, the transmitted electric field is equivalent, with the exception that $Z_G$ is replaced by the complex metafilm impedance $Z(\omega)$ at the front face of the GaAs:

$$E_{\mathrm{MF}}(\omega) = E_0 \frac{2Z(\omega)}{Z(\omega) + Z_0} \frac{2Z_0}{Z_G + Z_0}. \tag{2}$$

The ratio of these two expressions, $\tilde{t}_{\mathrm{Meas}}$, describes what we actually measure. The magnitude of this quantity, $t_{\mathrm{Meas}}$, is shown by the black curves in Figures 2 and 3:

$$t_{\mathrm{Meas}}(\omega) = \left|\tilde{t}_{\mathrm{Meas}}(\omega)\right| = \left| \frac{2Z(\omega)}{Z(\omega) + Z_0} \frac{Z_G + Z_0}{2Z_G} \right|. \tag{3}$$

Unlike our measurements, the simulations require no accounting for Fresnel reflections at the back substrate face and phase accumulations due to wave propagation in the substrate can be divided out. Therefore, the transmission coefficients are described by a much simpler equation

$$t_{\mathrm{Sim}}(\omega) = \left|\tilde{t}_{\mathrm{Sim}}(\omega)\right| = \left| \frac{2Z(\omega)}{Z(\omega) + Z_0} \right|. \tag{4}$$

We add that these transmission coefficients are equivalent to the complex $S$-parameter $s_{21}$, which is often the output returned by simulation software. From the equations, we see that to cast our simulations in the same form as the measured data we need only to multiply the simulations by $(Z_G + Z_0)/2Z_G = 2.33$. The results of this operation applied to our simulated transmission coefficients are shown as the red curves in Figures 2 and 3. The close agreement to measured data enables us to confidently use the simulated results in further studies. It also provides support for the experimental procedure of using a bare reference substrate to isolate the metafilm properties, despite the fact that

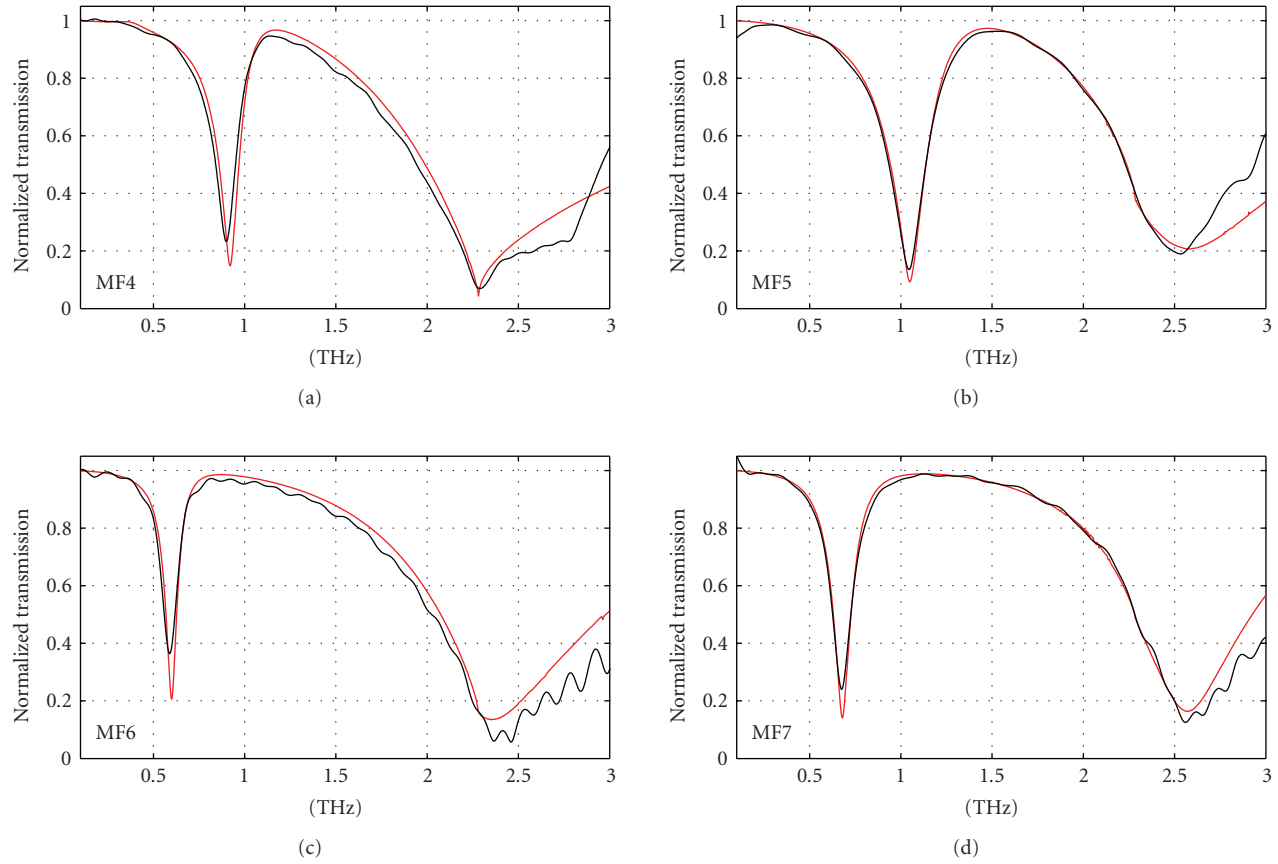


FIGURE 3: Normalized transmission through metafilm samples MF4, MF5, MF6, and MF7. Black curves indicate measured data while red curves show simulation results.

the metafilm's properties are heavily influenced by the substrate. And finally, it foreshadows that the metafilm can be well described as a *two-dimensional* composite. In this sense, the metafilm can be thought of as a boundary-confined, or extremely thin, phase shifter, instead of a three-dimensional effective medium.

It is important to point out that the metafilm impedance $Z(\omega)$ used in (1)–(4) incorporates the effect of the *backing* substrate, which in this case is GaAs. Therefore, $Z(\omega)$ has some functional dependence on $Z_G$. However, if a wave was incident upon the GaAs side of the boundary, then $Z(\omega)$ would become dependent on $Z_0$ instead of $Z_G$; in this case, free space is the backing substrate. The functional dependence on the backing material will be made clearer in a following section.

One particularly useful feature of the simulations is that they easily provide extra information, such as the reflection coefficient, $\widetilde{r}(\omega) = s_{11} = r(\omega)e^{-j\phi(\omega)}$. The simulated reflection and transmission coefficients are shown by the black curves in Figures 4 and 5. We add that these plots are not normalized to a substrate spectrum, as was the case in Figures 2 and 3. By studying the simulations we can begin to understand the behavior of the metafilms. For example, in every sample $t$ tends to the value 0.57 and $r$ tends to 0.43 as the frequency approaches zero. Similar behavior can be seen between the high and low frequency resonances of each sample, and even out to high frequencies in some samples. We also observe that some samples have two very distinct and clean resonances, while others have highly asymmetric and overlapping resonances.

## 3. METAFILM BEHAVIOR AND MODELING

Using the simulations we can now discuss the relationships between the macroscale properties of our samples and their microscale differences. This begins by first addressing the variability in the rings themselves. As can be seen in Figure 1, all of the rings are modifications of the original two structures MF4 and MF6. All of the rings were further designed to have the same ring area of 672 $\mu$m$^2$. Samples MF3, MF4, and MF5 differ only in modifications to the eSRR gaps. It is typically assumed that these gaps define the "capacitive" part of the eSRR response while the loops define the "inductive" part. This concept is illustrated in Figure 6(a) where the sample unit cells are modeled as lumped-element *RLC* circuits. This model is useful mainly in that it describes the Lorentzian nature of the resonance. One can use this model to roughly predict how our microstructural eSRR changes will affect the macroscale responses of our samples.

The resonant frequency of an *RLC* circuit is inversely related to the square root of both the inductance and capacitance. With this in mind, one can intuitively predict metafilm

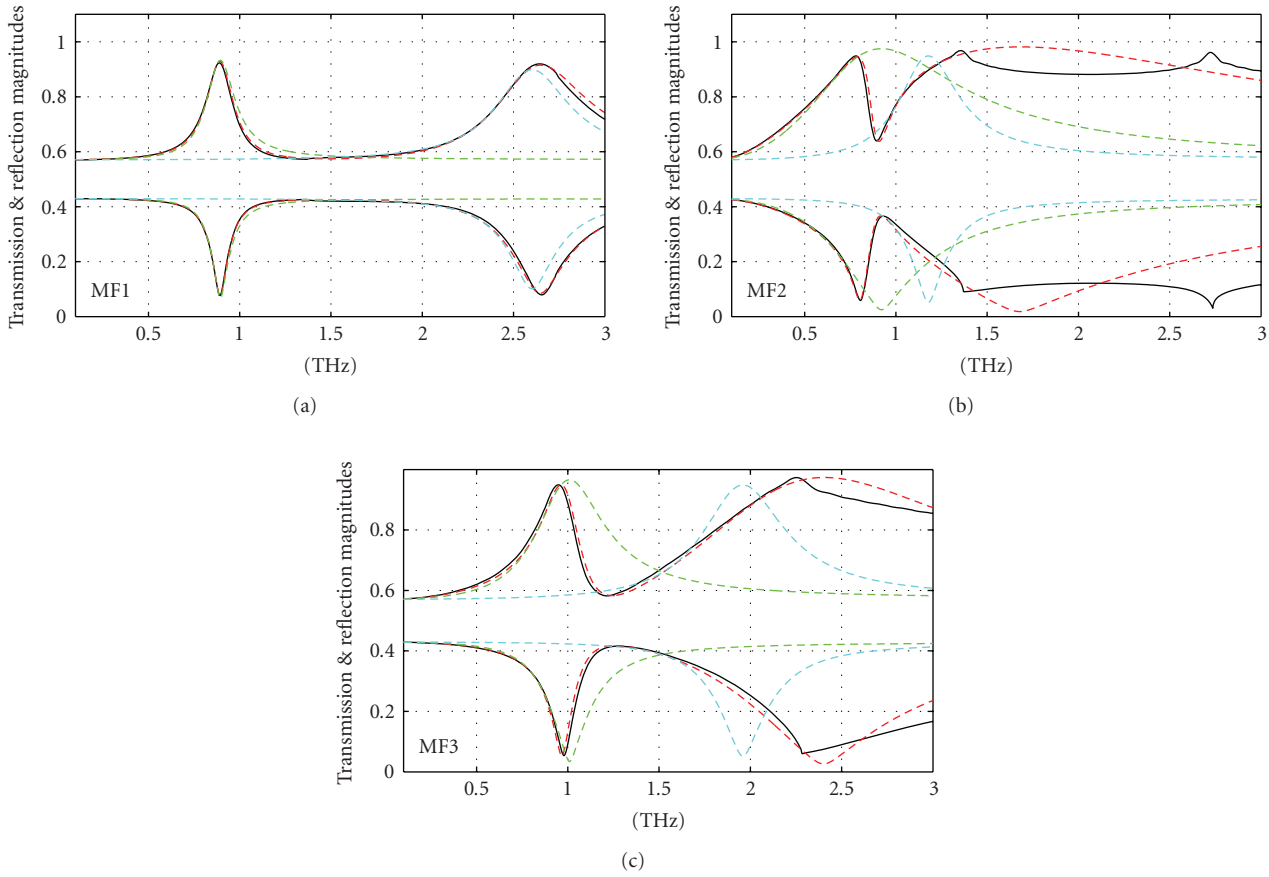


Figure 4: Transmission and reflection coefficients based on simulation and the TL-RLC circuit model for metafilm samples MF1, MF2, and MF3. Simulation results are shown in black. Red-dashed curves show the combined reflection and transmission coefficients based on the TL-RLC model. Green and blue dashed curves show the individual low and high frequency resonances, respectively, calculated by setting either $R_1$ or $R_2$ to a very large value.

behavior. For example, the extra metallic pad within the gap of MF5 can be regarded as splitting the capacitor into two coupled series capacitors, thus lowering the overall capacitance. The inductive response is largely determined by the area of the loops [2], so fixing the area and outer shape of the rings should, in principle, minimize the inductance as a performance variable. The net result is an increased resonance frequency. Indeed this is what we observe in Figure 5 by comparing MF4 and MF5. Similarly, MF6 should have roughly twice the capacitance (two capacitors in parallel) of MF4 causing a decrease in the resonance frequency; again this is consistent with the data. Sample MF7 is similar to MF6 where the added metallic pads decrease the capacitance with respect to MF6. The resonance frequency shifts up, as expected. Finally, by increasing the split gap width, $w$, sample MF4 should have a larger capacitance and slightly lower resonance frequency than MF3. Again this is observed in the data. We also point out an inverse relationship between capacitance and resonance linewidths in samples MF3–MF7. Those samples with the lower capacitance, or higher resonance frequency, also have broader linewidths.

Samples MF1 and MF2 are more radical variations; however, they maintain the same split gap and ring area as MF3 by stretching one dimension at the expense of shrinking another. One might expect that this alteration would have a minimal effect on the capacitance and, based on loop area, the inductance as well. In turn, we would expect little change in the lower frequency resonance. However, this is not the case. While the *position* of the lower frequency resonance does not shift greatly, the shape of this resonance is significantly altered. This is illustrated in Figure 4 by the green dashed curves which depict the first resonance after being mathematically separated from the higher-frequency resonance. This separation will be discussed in the following sections. One clear effect of changing the shape of the ring is to alter the linewidth of the lower resonance. An even greater effect observed in MF2 is the radical reshaping of the resonances. This behavior is due to a coupling effect occurring between the high and low frequency resonances. The high frequency resonance is usually understood to be due to dipole-dipole interactions between the two outside vertical (parallel to E-field) conductors of the rings. Since these conductors are relatively long on sample MF2, we expect this resonance to be shifted lower in frequency. The resulting close proximity between the low and high frequency resonances of this ring creates a strong coupling effect that reshapes the

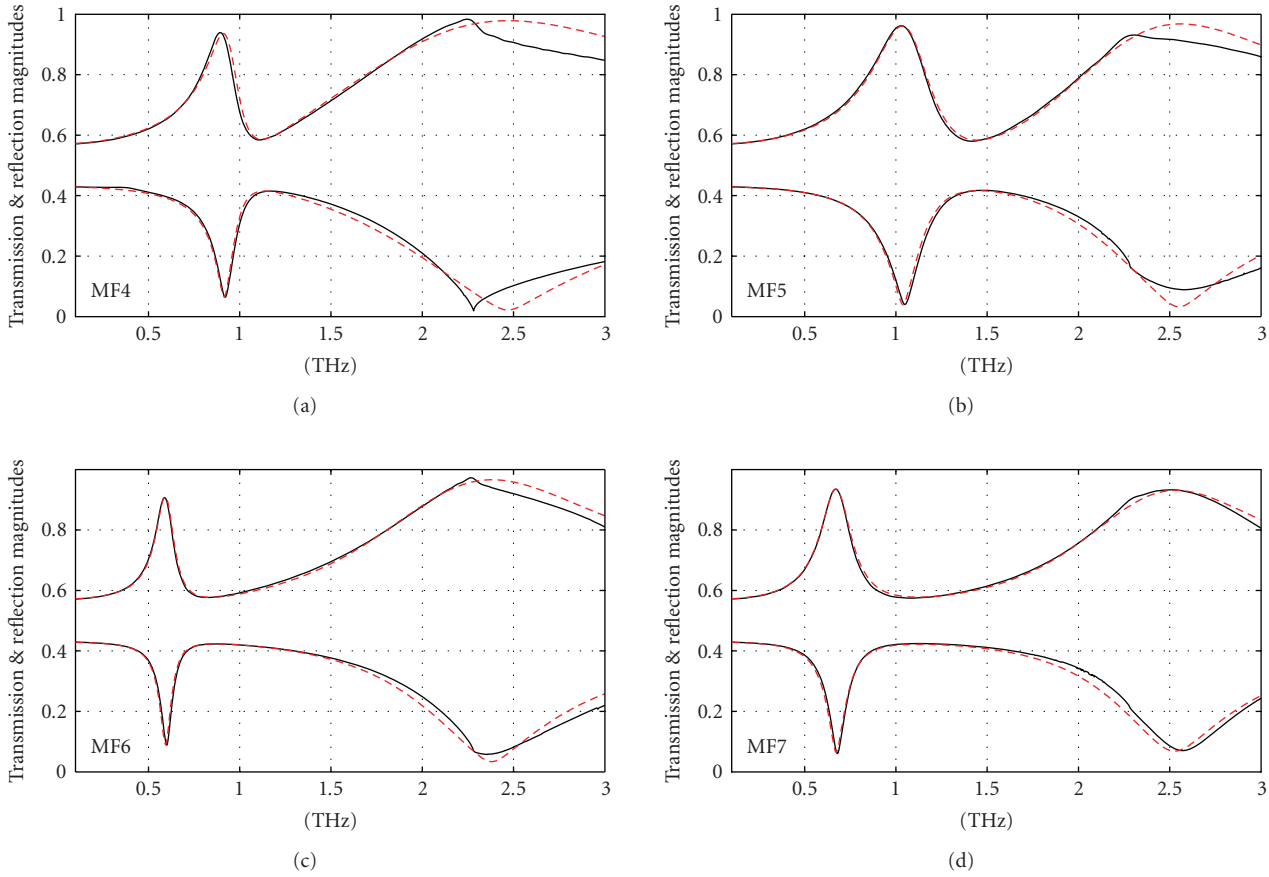


Figure 5: Transmission and reflection coefficients based on simulation and the TL-RLC circuit model for metafilm samples MF4, MF5, MF6, and MF7. Simulation results are shown in black. Red-dashed curves show the combined reflection and transmission coefficients based on the TL-RLC model.

transmission and reflection curves. The opposite is true for MF1, where the short vertical conductors shift the high frequency resonance to even higher values. Here the coupling effect is almost entirely eliminated and MF1 features very clean and distinct resonances.

We mention again that some samples have much narrower linewidths, or higher $Q$'s, than others. This is clearly an important attribute for possible future metamaterial devices. In filtering, for example, a narrow linewidth might be desirable for reducing noise. Broadband metamaterial devices such as detectors might benefit from ring designs that increase linewidth.

To help understand the origin of the observed transmission and reflection behavior it is helpful to derive a simple theoretical model of the metafilms. While the ring model of Figure 6(a) is intuitively helpful, a better model would incorporate other effects as well. As alluded to earlier, one approach is to treat the metafilm as an effective medium having some predetermined thickness, and a resonant permittivity with a Lorentzian functional form. This approach is valid for three-dimensional metamaterials in which planar layers of rings are spaced at a distance roughly equivalent to the unit cell length. However, our metafilms are essentially very thin, *single* metallic layers fabricated on relatively thick substrates. This makes the concept of effective media difficult to implement. The main problem is the assignment of the effective thickness. If this thickness is less than that of the substrate, then the effective medium treatment artificially creates a boundary between the metamaterial layer and the substrate. Upon deriving the transmission coefficient of this effective metamaterial layer, that boundary will create Fresnel reflections resulting in Fabry-Perot effects. These effects are not present in the actual measurements, nor in the full EM simulations.

Alternatively, one can perform more rigorous electromagnetic calculations assuming known or derived forms for the electric and magnetic polarizabilities [7, 26]. While these approaches can be powerful, accurate, and widely applicable to diverse situations, they are relatively difficult to implement and do not generally provide an immediate intuition into the processes at work and their relation to macroscale behavior.

These troubles can be avoided by using the model shown in Figure 6(b). The model is similar to previously reported models [27] and utilizes a doubly resonant lumped-element circuit at the boundary of two TEM transmission lines (TLs). The two TLs represent the air and substrate while the resonant circuit represents the metafilm layer at their boundary. Since the metafilm is very thin, the lumped-element

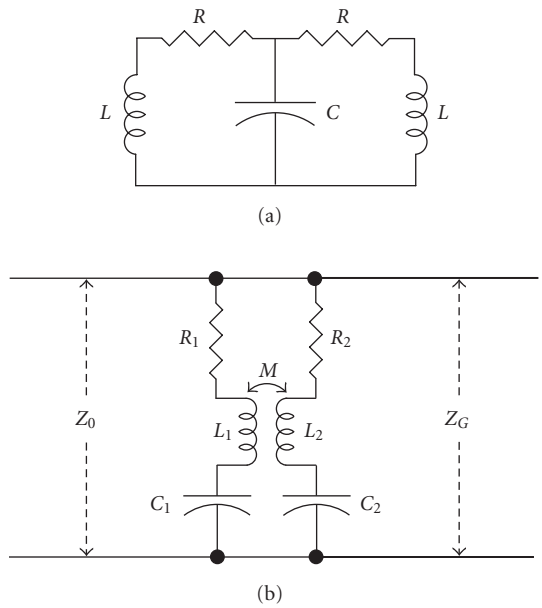


FIGURE 6: Circuit models for metafilm samples. (a) A series *RLC* circuit commonly used to describe the Lorentzian response of metamaterials. (b) The transmission-line *RLC* model which incorporates the effects of the substrate and uses a transformer to model the coupling between resonant modes.

approximation is valid in that the *RLC* circuit introduces no appreciable phase accumulation as the wave travels "through" it. Of course, the wave's phase is affected by the circuit, but only in the sense of a boundary-induced phase shift. The metafilm, and its analogous TL-RLC model, can be quantitatively described with only a few equations. The transmission and reflection coefficients follow the normal form

$$\tilde{t}(\omega) = \frac{2Z(\omega)}{Z(\omega) + Z_0}, \qquad \tilde{r}(\omega) = \frac{Z(\omega) - Z_0}{Z(\omega) + Z_0}, \tag{5}$$

where, like before, $Z_0 = 377\,\Omega$ is the impedance of $TL_0$ and $Z(\omega)$ is the complex impedance of the metafilm. $Z(\omega)$ can be obtained by noting that the impedance at the metafilm boundary is the parallel combination of the *RLC* circuit impedance and the impedance of $TL_G$, which is $Z_G = 103\,\Omega$. The impedance of the *RLC* circuit alone is

$$Z_{\text{ckt}}(\omega) = \frac{Z_{r1}Z_{r2} + \omega^2 M^2}{Z_{r1} + Z_{r2} - j\omega 2M}, \tag{6}$$

where $Z_{r1}$ and $Z_{r2}$ are the impedances of the individual series circuits, $R_1L_1C_1$ and $R_2L_2C_2$, spanning the transmission line and $M$ is the inductive coupling between these circuits. Both individual circuits have impedances of the form

$$Z_{rx} = R_x + j\omega L_x + \frac{1}{j\omega C_x}. \tag{7}$$

We clarify here that $Z_{\text{ckt}}$ is not the impedance used in (1)–(4) because it does not include the effect of the backing substrate, which is integral to the metafilm behavior. Rather $Z_{\text{ckt}}$ is only a conceptual 2D phase shifting and absorption layer, which can be combined with the backing substrate $Z_G$ to obtain the effective metafilm impedance $Z(\omega)$. Again, this is accounted for by computing the parallel impedance of $Z_{\text{ckt}}$ and $Z_G$. The result is

$$Z(\omega) = \frac{Z_G(Z_{r1}Z_{r2} + \omega^2 M^2)}{Z_G(Z_{r1} + Z_{r2} - j\omega 2M) + Z_{r1}Z_{r2} + \omega^2 M^2}. \tag{8}$$

A brief discussion of the limiting cases highlights some of the model's behavior. For $M = 0$, there is no coupling between the low and high resonances of the metafilm. In this case, the metafilm response $Z(\omega)$ is the parallel combination of the two *RLC* resonances and the substrate. Based on (7), it is clear that at low frequencies ($\omega \to 0$), both $Z_{r1} \to \infty$ and $Z_{r2} \to \infty$. Hence the overall impedance presented to the incident wave is $Z_G$. This clarifies why the simulated transmission and reflection coefficients for every sample tend to 0.43 and 0.57, respectively; these values represent $t$ and $r$ for the bare substrate. Consequently, the metafilm is essentially transparent to the incoming wave at off-resonance frequencies, an important implication in filtering applications. For our model, similar behavior occurs at very high frequencies when $M = 0$. This is generally not observed in the actual sample measurements or simulations due to the higher-order resonances. For frequencies near the resonance of one or the other *RLC* circuit, the impedance drops sharply, causing a local maximum in $r$ and a minimum in $t$. As the coupling parameter $M$ departs from zero, the neighboring circuit affects the magnitude of this impedance drop. The coupling effect on the overall response is most drastic when the two *RLC* circuits have closely spaced resonances.

The task remains to match this model with the data. This is done by choosing the values of $R_1, L_1, C_1, R_2, L_2, C_2$, and $M$ that result in $t$ and $r$ most closely overlapping the data. Limitations to these values are immediately obvious. For example, $L$'s and $C$'s must be paired to ensure that $\omega = 1/\sqrt{LC}$ is approximately equal to one or the other resonance frequency. Similarly, the resonance linewidths can be roughly matched by adjusting $C$ and $L$ simultaneously in an inverse relationship. Figures 4 and 5 show the comparison between the simulations (black curves) and the TL-RLC model (red-dashed curves). Table 2 shows the parameter values used to obtain these matches. The model clearly matches the simulated data well except at higher frequencies where higher-order modes become significant. The circuit parameters shown in Table 2 were obtained by manual adjustments and observation of the resulting match to simulations. The ease with which this is accomplished is dependent upon how clean the resonances are. Sample MF2, for example, has highly asymmetric resonances that complicate the determination of the "correct" *RLC* values. The nonintuitive nature of this match can be seen in Figure 4, where we show the individual resonances obtained by setting either $R_1$ or $R_2$ to a very large value. The positions of the individual resonances can be significantly shifted from their apparent positions in the transmission and reflection coefficients.

Table 2: Circuit parameters for matching TL-RLC model to simulated data. Resistor values are given in Ohms, capacitor values in femtofarads, and inductor values and coupling coefficients in picohenries.

| Structure | Circuit component | | | | | | |
|---|---|---|---|---|---|---|---|
| | $R_1$ ($\Omega$) | $L_1$ (pH) | $C_1$ (fF) | $R_2$ ($\Omega$) | $L_2$ (pH) | $C_2$ (fF) | $M$ (pH) |
| MF1 | 15 | 90.0 | 0.352 | 25 | 38.0 | 0.099 | −10.0 |
| MF2 | 5 | 15.3 | 1.95 | 11 | 41.5 | 0.440 | −15.0 |
| MF3 | 7 | 31.0 | 0.790 | 11 | 33.0 | 0.210 | −19.0 |
| MF4 | 8 | 36.0 | 0.750 | 8 | 24.5 | 0.300 | −18.0 |
| MF5 | 6 | 29.0 | 0.770 | 13 | 25.0 | 0.200 | −11.5 |
| MF6 | 19 | 130 | 0.550 | 8 | 12.0 | 0.400 | −10.0 |
| MF7 | 13 | 74.0 | 0.750 | 20 | 18.0 | 0.240 | −10.0 |

## 4. DISCUSSION

It is now necessary to discuss the extracted circuit parameters. We immediately point out that the circuit parameters in Table 2 do *not* necessarily correspond to the actual capacitance of the eSRR gap, the inductance of the eSRR loops, or the resistance of the conductors. In fact, the extracted values usually have the opposite behavior of what was expected. Taking the low frequency resonances as an example, we expect that the increased width of the split gap in MF4 would result in a larger capacitance than MF3. Surprisingly, the extracted capacitance, $C_1$, of MF4 is lower than that of MF3 and the greatest change is observed in the inductance, $L_1$. Another example is seen in the comparison of samples MF4 and MF5. The attempt here was to decrease the capacitance of the gap by inserting an intergap conductor. Instead, this variation hardly affected the capacitance of the model at all. Again, the inductive response was most affected. Indeed the parameters of Table 2 appear to have a "dual" characteristic in comparison to expectations. Where we expect large changes in capacitance, we observe large changes in inductance and vice versa.

The cause of this contrary behavior is that our model tells us little about real eSRR microparameters such as gap capacitance. The model only mimics the functional behavior of the metafilm by means of resonant circuits. The same behavior could be generated with two coupled systems comprised of springs, masses, and dashpots, although this would clearly have no relation whatsoever to a split-ring resonator. It is possible, however, that a model based on the dual circuit to that of Figure 6(b) may provide a better intuitive description of the relationship between macroscale performance and microscale variations. The exact form of this dual model is currently being studied and may constitute a closer match to previous circuit models [27]. Regardless, the value of the model is that it provides some metafilm analysis tools and also defines certain functional boundaries. For example, samples MF1, MF2, and MF3 all share a ring area of 672 $\mu$m, but both the inductive, $L_1$, and capacitive, $C_1$ response varied by almost as much as 6 times. While we cannot ensure true eSRR inductance or capacitance values we can say that neither of these quantities remains constant as the ring shape is changed. This is important because simultaneous and inverse adjustments in $L$ and $C$ are exactly the method used to tune resonator linewidths while preventing resonance shifts.

The model provides another interesting insight into linewidth limitations. The metafilm is bounded on its sides by both air and GaAs, both of which affect the macroscale properties of the metafilm, at least in part, by altering the capacitance of the split-gap. But the model also shows that they limit how narrow a linewidth can be achieved for a metafilm filter of the kind shown in this work. Consider the case where $R = 0$ in the circuit of Figure 6(a). For this undamped circuit, the result of removing any resistance is an infinitely narrow resonance. However, in the TL-RLC model, the metafilm impedance is intimately linked with the bounding substrate impedance, so there can never be an "undamped" situation, even when $R_1 = 0$. The backing substrate always provides a finite impedance by which to prevent infinitely narrow metafilm linewidths. However, it is also clear that by choosing a substrate with a favorable impedance and properly tuning the eSRR inductance and capacitance, limited linewidth adjustment is possible.

The model also clarifies underlying behavior inherent in coupled-resonator systems. As previously shown, the model can be used to extract the *individual* behavior of the two coupled metafilm resonances. This is done by first adjusting model parameters to match the measured or simulated transmission or reflection coefficients. Then one of the resistance values, $R_1$ or $R_2$, is assigned a very high value such that it behaves as an open circuit. This turns off one resonance and reveals the structure of the other. These individual resonances are displayed in Figure 4. Similarly, the model parameter $M$ can be set to zero to observe the behavior of both resonances operating simultaneously but without coupling. Such tools are both intuitive and useful for a metafilm designer trying to achieve some desired behavior.

## 5. CONCLUSION

The potential uses of electric metafilms are numerous. For example, metafilms fabricated in the "complementary" fashion exhibit bandpass behavior in transmission yet retain a continuous and relatively thick metal layer over the substrate surface. These metafilms may serve as future grids or electrodes for biasing electronic components where a transparency window is desired. Existing "transparent" electrodes require extremely thin ~10 nm metallization to be both conducting and transparent. Metafilms offer obvious advantages in these cases, especially when high current densities are required. Further, dynamical control of metafilm properties is an important capability in the THz regime. This versatility offers tremendous possibilities for THz switches, modulators, and phase shifters.

We finally reiterate the advantage of studying microstructural variations in metamaterials. Our sample MF1 clearly shows a very clean resonant response in comparison to more traditional ring designs. This design offers a clear advantage for practical applications such as filtering. Moreover, with the continuing progression of more advanced metamaterials systems, such as negative-index materials, there is an obvious

need for reducing the complexity of the design procedure. The short ring, MF1, offers a vivid demonstration of decoupling two physical effects; such designs will become increasingly important in future metamaterial technology.

In conclusion, we have studied the behavior of a variety of new THz metafilm designs through experimental THz time-domain transmission measurements and full electromagnetic simulations. The macroscale properties of these materials are seen to exhibit a strong dependence on microstructural variations, and are generally consistent with intuitive expectations. Using these results we were able to use a simple transmission-line and lumped-element circuit model that provides insight into the limitations and design tradeoffs for metafilm performance. Though our work concentrated on the THz regime, it has wide applicability from the radio to the infrared spectra due to the scalability [28] of metamaterials, and metafilms. The continued research of the fundamental properties of metamaterials will have a great impact on many future novel metamaterial-based devices.

## ACKNOWLEDGMENTS

This work was performed, in part, at the Center for Integrated Nanotechnologies, a US Department of Energy, Office of Basic Energy Sciences, Nanoscale Science Research Center, operated jointly by Los Alamos and Sandia National Laboratories. Los Alamos National Laboratory, an affirmative action/equal opportunity employer, is operated by Los Alamos National Security, LLC, for the National Nuclear Security Administration of the US Department of Energy under Contract no. DE-AC52-06NA25396.

## REFERENCES

[1] V. G. Veselago, "The electrodynamics of substances with simultaneously negative values of $\epsilon$ and $\mu$," *Soviet Physics Uspekhi*, vol. 10, no. 4, pp. 509–514, 1968.

[2] J. B. Pendry, A. J. Holden, D. J. Robbins, and W. J. Stewart, "Magnetism from conductors and enhanced nonlinear phenomena," *IEEE Transactions on Microwave Theory and Techniques*, vol. 47, no. 11, pp. 2075–2084, 1999.

[3] D. R. Smith, W. J. Padilla, D. C. Vier, S. C. Nemat-Nasser, and S. Schultz, "Composite medium with simultaneously negative permeability and permittivity," *Physical Review Letters*, vol. 84, no. 18, pp. 4184–4187, 2000.

[4] T. Koschny, M. Kafesaki, E. N. Economou, and C. M. Soukoulis, "Effective medium theory of left-handed materials," *Physical Review Letters*, vol. 93, no. 10, Article ID 107402, 4 pages, 2004.

[5] Th. Koschny, P. Markoš, E. N. Economou, D. R. Smith, D. C. Vier, and C. M. Soukoulis, "Impact of inherent periodic structure on effective medium description of left-handed and related metamaterials," *Physical Review B*, vol. 71, no. 24, Article ID 245105, 22 pages, 2005.

[6] For a review of the conditions of effective media applicable to metamaterials see ref. [5] and the references therin.

[7] C. L. Holloway, M. A. Mohamed, E. F. Kuester, and A. Dienstfrey, "Reflection and transmission properties of a metafilm: with an application to a controllable surface composed of resonant particles," *IEEE Transactions on Electromagnetic Compatibility*, vol. 47, no. 4, pp. 853–865, 2005.

[8] J. C. Vardaxoglou, *Frequency Selective Surfaces: Analysis and Design*, John Wiley & Sons, New York, NY, USA, 1997.

[9] J. A. Kong, *Electromagnetic Wave Theory*, John Wiley & Sons, New York, NY, USA, 2nd edition, 1990.

[10] H. Chen, L. Ran, D. Wang, J. Huangfu, Q. Jiang, and J. A. Kong, "Metamaterial with randomized patterns for negative refraction of electromagnetic waves," *Applied Physics Letters*, vol. 88, no. 3, Article ID 031908, 3 pages, 2006.

[11] J. E. Davis, "Bandpass interference filters for very far infrared astronomy," *Infrared Physics*, vol. 20, no. 4, pp. 287–290, 1980.

[12] D. A. Weitz, W. J. Skocpol, and M. Tinkham, "Capacitive-mesh output couplers for optically pumped far-infrared lasers," *Optics Letters*, vol. 3, no. 1, pp. 13–15, 1978.

[13] F. Baumann, W. A. Bailey Jr., A. Naweed, W. D. Goodhue, and A. J. Gatesman, "Wet-etch optimization of free-standing terahertz frequency-selective structures," *Optics Letters*, vol. 28, no. 11, pp. 938–940, 2003.

[14] R. D. Rawcliffe and C. M. Randall, "Metal mesh interference filters for the far infrared," *Applied Optics*, vol. 6, no. 8, p. 1353, 1967.

[15] T. J. Yen, W. J. Padilla, N. Fang, et al., "Terahertz magnetic response from artificial materials," *Science*, vol. 303, no. 5663, pp. 1494–1496, 2004.

[16] W. J. Padilla, A. J. Taylor, C. Highstrete, M. Lee, and R. D. Averitt, "Dynamical electric and magnetic metamaterial response at terahertz frequencies," *Physical Review Letters*, vol. 96, no. 10, Article ID 107401, 4 pages, 2006.

[17] H.-T. Chen, W. J. Padilla, J. M. O. Zide, A. C. Gossard, A. J. Taylor, and R. D. Averitt, "Active terahertz metamaterial devices," *Nature*, vol. 444, no. 7119, pp. 597–600, 2006.

[18] H.-T. Chen, W. J. Padillas, J. M. O. Zide, et al., "Ultrafast optical switching of terahertz metamaterials fabricated on ErAs/GaAs nanoisland superlattices," *Optics Letters*, vol. 32, no. 12, pp. 1620–1622, 2007.

[19] H.-T. Chen, J. F. O'Hara, A. J. Taylor, et al., "Complementary planar terahertz metamaterials," *Optics Express*, vol. 15, no. 3, pp. 1084–1095, 2007.

[20] J. F. O'Hara, E. Smirnova, H.-T. Chen, et al., "Properties of planar electric metamaterials for novel terahertz applications," *Journal of Nanoelectronics and Optoelectronics*, vol. 2, no. 1, pp. 90–95, 2007.

[21] D. Schurig, J. J. Mock, and D. R. Smith, "Electric-field-coupled resonators for negative permittivity metamaterials," *Applied Physics Letters*, vol. 88, no. 4, Article ID 041109, 3 pages, 2006.

[22] W. J. Padilla, M. T. Aronsson, C. Highstrete, M. Lee, A. J. Taylor, and R. D. Averitt, "Electrically resonant terahertz metamaterials: theoretical and experimental investigations," *Physical Review B*, vol. 75, no. 4, Article ID 041102, 4 pages, 2007.

[23] D. Grischkowsky, S. Keiding, M. van Exter, and Ch. Fattinger, "Far-infrared time-domain spectroscopy with terahertz beams of dielectrics and semiconductors," *Journal of the Optical Society of America B*, vol. 7, no. 10, pp. 2006–2015, 1990.

[24] J. F. O'Hara, J. M. O. Zide, A. C. Gossard, A. J. Taylor, and R. D. Averitt, "Enhanced terahertz detection via ErAs:GaAs nanoisland superlattices," *Applied Physics Letters*, vol. 88, no. 25, Article ID 251119, 3 pages, 2006.

[25] "CST Microwave Studio ®, ©2005 CST—Computer Simulation Technology," Wellesley Hills, Mass, USA, December 2005, http://www.cst.com.

[26] F. Falcone, T. Lopetegi, M. A. G. Laso, et al., "Babinet principle applied to the design of metasurfaces and metamaterials," *Physical Review Letters*, vol. 93, no. 19, Article ID 197401, 4 pages, 2004.

[27] J. D. Baena, J. Bonache, F. Martín, et al., "Equivalent-circuit models for split-ring resonators and complementary split-ring resonators coupled to planar transmission lines," *IEEE Transactions on Microwave Theory and Techniques*, vol. 53, no. 4, pp. 1451–1460, 2005.

[28] W. J. Padilla, D. R. Smith, and D. N. Basov, "Spectroscopy of metamaterials from infrared to optical frequencies," *Journal of the Optical Society of America B*, vol. 23, no. 3, pp. 404–414, 2006.

Hindawi Publishing Corporation
Active and Passive Electronic Components
Volume 2007, Article ID 24084, 8 pages
doi:10.1155/2007/24084

*Research Article*

# Extraordinary Transmission and Enhanced Emission with Metallic Gratings Having Converging-Diverging Channels

**Arvind Battula,[1] Yalin Lu,[2] R. J. Knize,[2] Kitt Reinhardt,[3] and Shaochen Chen[1]**

[1] *Department of Mechanical Engineering, Center for Nano and Molecular Science and Technology, University of Texas, Austin, TX 78712, USA*
[2] *Physics Department, Laser Optics Research Center, USAF Academy, CO 80840, USA*
[3] *Air Force Research Laboratory, AFOSR/NE, 875 North Randolph Street, Suite 326, Arlington, VA 22203, USA*

Received 22 October 2007; Accepted 26 November 2007

Recommended by Weili Zhang

Transmission metallic gratings having the shape of converging-diverging channel (CDC) give an extra degree of freedom to exhibit enhanced transmission resonances. By varying the gap size at the throat of CDC, the spectral locations of the transmission resonance bands can be shifted close to each other and have high transmittance in a very narrow energy band. Hence, the CDC shape metallic gratings can lead to almost perfect transmittance for any desired wavelength by carefully optimizing the metallic material, gap at the throat of CDC, and grating parameters. In addition, a cavity surrounded by the CDC shaped metallic grating and a one-dimensional (1D) photonic crystal (PhC) can lead to an enhanced emission with properties similar to a laser. The large coherence length of the emission is achieved by exploiting the coherence properties of the surface waves on the gratings and PhC. The new multilayer structure can attain the spectral and directional control of emission with only $p$-polarization. The resonance condition inside the cavity is extremely sensitive to the wavelength, which would then lead to high emission in a very narrow wavelength band. Such simple 1D multilayer structure should be easy to fabricate and have applications in photonic circuits, thermophotovoltaics, and potentially in energy efficient incandescent sources.



In late 1980s, the concept of photonic crystals emerged, which initiated new studies of gratings, as examples of one-dimensional (1D) periodic media [1, 2]. Since then, some theoretical studies have been done on the transmission gratings, but they did not receive much attention because it was thought that the transmission through the subwavelength apertures is very low according to the standard aperture theory by Bethe [3], which states that the transmission through a subwavelength circular hole ($r \ll \lambda$) in an infinitely thin perfectly conducting metal sheet would scale uniformly with the ratio of $r$ to $\lambda$ to the power of four. But, an extraordinary transmission (EOT) of several orders of magnitude more than Bethe's prediction has been reported through an array of subwavelength holes milled in an opaque metal screen [4]. The underestimation of transmission by Bethe's theory is because it is too idealized to consider the surface modes that might be involved and also propagating of evanescent modes that could be excited inside the holes [5]. Subsequently, enhanced transmission through hole arrays in metal films has been studied in great detail both theoretically and experimentally. This has sparked renewed interests in studying the transmission gratings (or slits), which are 1D version of the hole structures studied by [4], to explain the underlying physics for enhanced transmission. However, the transmission properties between slit and hole arrays have a fundamental difference. In a slit waveguide, there is always a propagating mode inside the channel, whereas in a hole waveguide all modes are evanescent when hole diameters are smaller than half the wavelength, and there is a cutoff frequency for transmission [6]. Hence, the slit and hole array structures have very different propagation mechanisms. But, it is believed in general that the EOT phenomenon is mainly due to the surface plasmons polariton (SPP) modes trapped at the interface of metal and dielectric. The SPPs are actually quanta of collective plasma oscillations localized at interface of a metal and dielectric [7]. However, not all agree on the same SPP mechanism for the enhanced transmission phenomena [8, 9]. Nevertheless, according to several other theoretical and experimental studies, the enhanced transmission process through subwavelength metallic hole array (MHA) can be divided into three steps: the coupling of light to SPPs on the incident surface, transmission through the holes to the

second surface, and then reemission from the second surface [5]. In addition, diffraction plays a central role in the transmission process through subwavelength holes or gratings. When a plane wave is incident on grating array, the diffraction leads to evanescent wave. After the transmitted evanescent wave reaches the far end of the array, it gets diffracted again producing a propagating transmitted wave. Therefore, the transmission enhancement occurs when the diffraction aids in coupling the incident light and the SPP modes of the metal structure [10]. It was also reported that for lamellar transmission metallic gratings, there are two transmission resonances: coupled SPP modes on both the horizontal surfaces of the metallic grating for $\lambda \sim d$, and cavity or waveguide modes located inside the slits for $\lambda \gg d$ [11]. SPPs will be resonantly excited on the gratings only when the higher-diffraction order along with the incident parallel momentum equals SPPs momentum according to the equation $K_{\mathrm{SPP}} = K_o \sin(\theta) \pm m\ (2\pi/d)$.

In thermal source, the light generation at the microscopic level is a spontaneous emission of photon when an emitter thermally excited relaxes to a lower state. Unlike the laser which produces highly directional and monochromatic light, thermal light source is isotropic with a broad spectrum. But the thermal source of light is coherent in the near field, that is, within a distance from the surface that is much smaller than the emission peak wavelength of the spectrum [12–14]. The coherence is due to the role of surface waves. Hence, a roughness or a grating on the surface can couple these waves to propagating waves, which will extend the coherence properties into the far field. Thus, by modifying the characteristics of the surface profile, the near field coherence properties can be extended to far field in a particular direction at a given wavelength. This has been observed first on a doped silicon grating supporting a surface plasmon polariton (SPP) [15]. Similarly, a peak in the thermal emission by gratings on ZnSe [16], gold [17], and SiC [18] was also observed. For these grating structures, it was noted that the excited surface waves could couple to the emitted radiation for the *p*-polarization only. No lobe of emission has been observed for *s*-polarization since, in this case, the SPPs or surface waves cannot be present [19].

In the present study, we propose a subwavelength grating with converging-diverging channel (CDC) for extraordinary transmission and in combination with one-dimensional (1D) PhC for enhanced emission. For the emission, there is a cavity between the CDC grating and the 1D PhC. Here, we could make use of the surface waves that could be present on both the metallic gratings and in the PhC structure. The 1D PhC considered is made of lossless dielectrics ($SiO_2$ and InSb) with refractive indices given by [20] $n_{\mathrm{SiO_2}} = 1.46$ and $n_{\mathrm{InSb}} = 3.95$. A freely available MIT photonic band (MPB) package was used for calculating the photonic band structure (PBS) of the PhC. The first or lower bandgap in the PBS is between the normalized frequency range of 0.136 to 0.217. So, a PhC having a unit cell thickness "a" of 100 nm has first bandgap wavelength range that is between 460 nm to 735 nm.

According to Kirchhoff's law, the directional spectral emissivity ($\varepsilon_{\lambda,\theta}$) can be determined by using $1-\rho_{\lambda,\theta} - \tau_{\lambda,\theta}$ [21], where the directional spectral reflectance, ($\rho_{\lambda,\theta}$), and the directional spectral transmittance, ($\tau_{\lambda,\theta}$), are evaluated by using a plane monochromatic wave incident from the air at an angle of incidence "$\theta$" as shown in Figure 1. In the figure, we show a schematic view of a metallic grating with CDC in vacuum that was studied with the definition of different parameters: the period of grating ($d$), the aperture width ($a$), the grating thickness ($t$), and the gap at the throat ($g$). The gap sizes were varied from 0.5 $\mu$m to 5 nm. It is plausible to use Maxwell's equation when the absolute lower limit of the length of macroscopic domain is 10 nm [22]. Therefore, it is assumed that the results obtained in the present study for gap of 5 nm will be rational. Nevertheless, it should be pointed out that the effects discussed in this study do apply for any other range of grating parameters provided that the aperture width is very small in comparison to the grating period. Also, the frequency of incident light has to be well below the plasma frequency of the metal [11]. The dielectric function of metals described in this study is from the tables reported in [20, 23]. The transmission for metallic lamellar gratings with transverse electric (TE) polarization suffers a cutoff wavelength [24]. Hence, we have analyzed the metallic gratings with only TM polarization (magnetic field vector parallel to the gratings) in order to study whether the enhanced transmission could be achieved for any desired wavelength with the CDC structure. The resulting governing equation for the time harmonic electromagnetic fields, with the dependent variable as magnetic field in the $z$-direction ($H_z$), is same as Helmholtz equation. Commercially available finite element software (FEMLAB 3.1i) was used for solving the governing equation. The 2D computational domain is surrounded by either a periodic boundary with perfect electric condition or a perfectly matching layer (PML) [25]. Since the proposed study has a structure that is periodic in 1D and has the length of the grating larger than the period of the grating, then the resulting computational domain would be a 2D domain. The

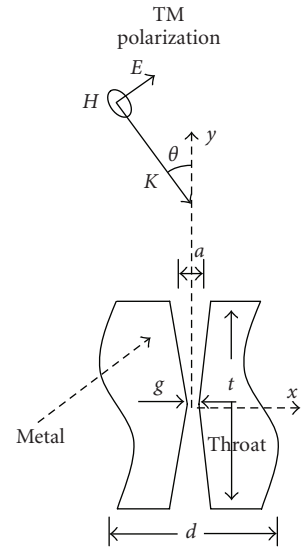


Figure 1: Schematic view of the lamellar transmission metallic grating with converging-diverging channels in vacuum with grating parameters as period ($d$), aperture ($a$), and thickness ($t$).

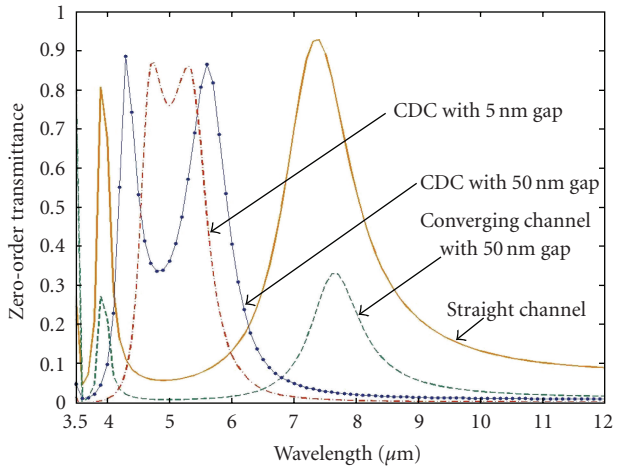


(a)

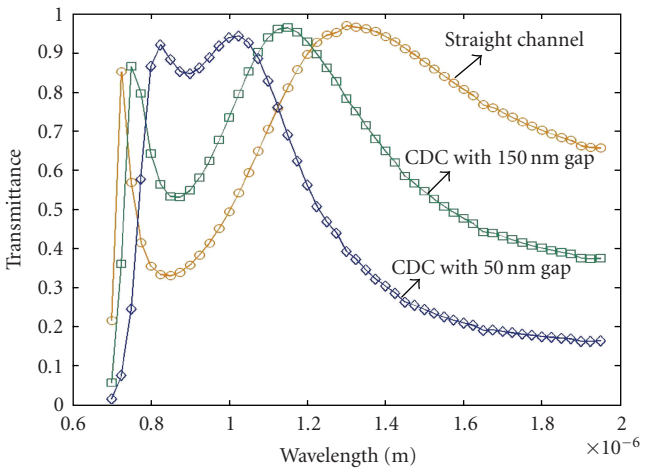


(b)

Figure 2: Zero-order transmittance for a normal incident plane wave on lamellar gratings in vacuum for different channel configurations, but with the same grating parameters as (a) $d = 3.5\,\mu$m, $a = 0.5\,\mu$m, and $t = 3.0\,\mu$m in gold film; (b) $d = 650$ nm, $a = 300$ nm, and $t = 500$ nm in silver film.

transmittance ($\tau$) and reflectance ($\eta$) of the CDC grating were calculated from the obtained electromagnetic field distributions as follows:

$$\tau = \frac{(H_z \cdot H_z^*)_{P1,F}}{(H_z \cdot H_z^*)_{P1,I}}, \qquad \eta = \frac{(Q \cdot Q^*)_{P2,F}}{(H_z \cdot H_z^*)_{P1,I}}, \tag{1}$$

where $Q = (H_z - (\partial H_z/\partial y)/(ik\ \cos(\theta)))$, $H_z$ is the magnetic field, $k$ is the wave vector, $\theta$ is the angle of incidence, and subscripts $F$ and $I$ indicate the incident and final transmitted energy. $P1$ and $P2$ indicate the planes below and above the grating.

Figure 2 shows the zero-order transmittance for normal incident radiation as a function of wavelength for different channel configurations. The CDC with 5 nm gap at the throat has a remarkable transmission in a very narrow wavelength band. The two transmission peaks for the straight channel are identified as the SPP and waveguide coupled resonance (~3.9 $\mu$m) and waveguide resonance (~7.4 $\mu$m) [11]. Although the two transmission peaks seen for the converging channel are located at almost the same resonance wavelengths as for the straight channel, the transmittance is much lower, which is explained later. For CDC, the locations of transmittance peaks have changed in spectral positions and are approaching each other as the gap at throat decreases, as seen in Figure 2(a). This would lead to a high transmission in a very narrow wavelength band, and the transmittance is almost negligible everywhere else in the considered wavelength range. A closer look at Figure 2(a) would also tell that the resonances for CDC occur at wavelengths which had lower transmittance with a straight channel. Similar kind of behavior can be observed at different wavelengths for the silver gratings (Figure 2(b)).

By varying the angle of incidence "$\theta$," we can calculate the PBS and $\omega(k_x)$, of these transmission resonances or surface excitations of the metallic gratings. Using the photonic band structure (PBS), both the spectral position and the width of transmission peaks can be found. In Figure 3(a), we show the PBS of a CDC gold grating with 100 nm gap at the throat in vacuum. Also, we show the energetic positions of the SPP modes (white dashed lines) for a nearly flat metal surface. Figure 3(a) shows that there are two transmission resonance bands, with the higher-energy band following close to the SPP mode energetic positions and lower-energy band shifts in spectral location with the angle of incidence "$\theta$." For the transmission resonances, the phases across the grating have to be in-phase for a Fabry-Perot or waveguide kind of resonance to occur [26]. With further decrease in the gap at throat to 50 nm (see Figure 3(b)), the band at the lower energy has become more dependent on "$\theta$," and the transmittance above the first-order diffraction has increased more, but now over a shorter range of energy spectrum when compared to that of the 100 nm gap (see Figure 3(a)). When the gap at the throat of CDC reduces the high-transmission resonance, bands in the PBS change from their previous energy positions, and the bands appear to approach each other (see Figure 3). Hence, it should be pointed out that with very small gap at the throat, the transmission over the entire energy spectrum could be made high only in a very narrow band. The shifting of transmission resonance band with the gap at the throat of the CDC can be seen in Figure 4, where the transmittance of CDC aluminum grating as a function of wavelength in UV-visible range and gap size at the throat is shown. The full width at half maximum (FWHM) of the transmission peak shrinks with the reduction in the throat gap. In addition, the transmission peak magnitude declines with the throat gap. This is due to two things: (i) the shift of transmittance peak to lower wavelengths that is accompanied by (ii) the change in the channel shape, which might increase the skin depth that would subsequently increase the absorption. Also, it is to be noted that the slight reduction in the transmittance peaks happens in the UV-visible range, and it is not observed at higher wavelength range since the skin depth remains constant for those wavelengths.

The normalized magnitude of the $x$-component electric field ($|E_x|$) along the center line of the channel at ~6.35 $\mu$m

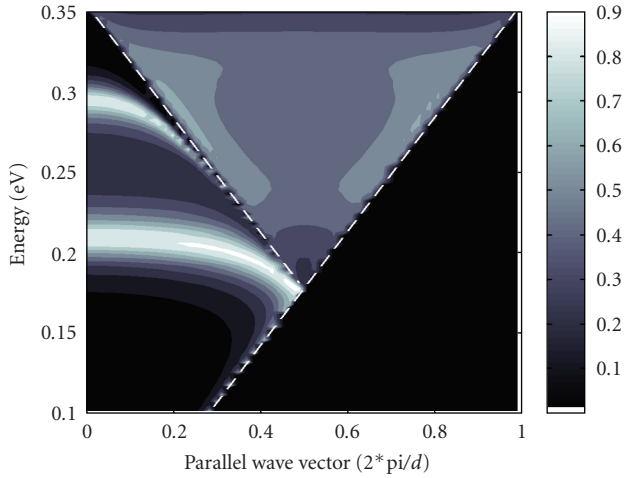


(a)

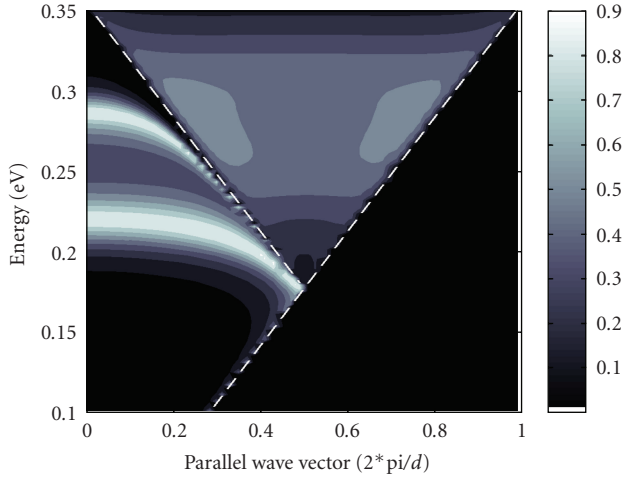


(b)

Figure 3: Photonic band structure of the surface plasmons responsible for the transmission resonances of gold gratings in vacuum with slit shape as (a) CDC with $g = 100$ nm and (b) CDC with $g = 50$ nm. The grating parameters are fixed at $d = 3.5\,\mu$m, $a = 0.5\,\mu$m, and $t = 3.0\,\mu$m. Also, energetic positions seen in figures are (white dashed lines) of the SPP modes.

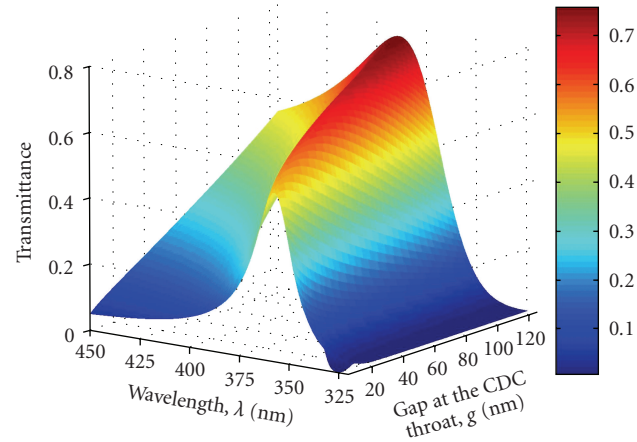


Figure 4: Transmittance in vacuum for CDC gratings as a function of the wavelength and distance at the gap of throat for the aluminum gratings having $d = 315$ nm, $a = 125$ nm, and $t = 100$ nm.

wavelength for the converging channel and CDC is shown in Figure 5. The variation of $|E_x|$ in the channel is proportional to the distribution of charges on the metallic grating channel surfaces. Also, by looking at the $|E_x|$ distribution along the channel would tell whether the wave inside the channel is in-phase or out-of-phase. In Figure 5(a), we show that when the gap is 500 nm, the wave inside the channel is an out-of-phase standing wave. This is because the minimum magnitude (or node) is not at the center of the channel, and the magnitudes near the end of channels (or antinodes) are not equal. This indicates that at the end of channel, the dipoles have unequal strength which could be due to the destructive interference of the wave inside the channel [24]. The surface charges oscillate between these two antinodes leading to the surface current that couples to the incident light and transmits it to the other side of grating. With the decrease in gaps near the throat, the node moves further away from the center, and hence the wave inside the channel goes more out-of-phase. Also, when the gap near the throat keeps decreasing, the dipole at the throat starts to gain in strength and becomes stronger than the dipole at the other end of channel. This causes very less net current or energy to flow out of the channel. Similarly, by looking at the $|E_x|$ distributions in Figure 5(b), we show that the wave inside the channel of CDC is a standing wave for different gaps near the throat. As the gap in CDC keeps decreasing, the node keeps moving toward the center of channel. Also, the magnitudes of $|E_x|$ at two antinodes are increasing and becoming equal. This shows that the CDC shape of the channel is aiding the wave inside the channel to become an in-phase standing wave. The condition for in-phase resonance inside the channel is given by [26] $2Kt + \Delta\phi = m2\pi$, where "$K$" is the wave vector of the resonance, and "$\Delta\text{ø}$" is the phase change on the aperture of the slits. The role of throat is that for various gap sizes the length of the channel surface would change and hence would result in having different resonance wave vector. This can be seen from Figure 5(b) where it is shown that at 6.35 $\mu$m wavelength the high transmittance happens at 200 nm gap near the throat, which has a standing wave inside the channel that is in-phase. A small decrease in the gap from 200 nm makes the standing wave inside the channel to go out-of-phase, and so the transmittance decreases. When the gap at throat becomes smaller, then the charges at throat gain strength, just like in the case of converging channel (see Figure 5(a)). This would not allow light to transmit more efficiently.

Normal emittance spectrum with $p$-polarization for the CDC grating with 5 nm gap and 1D PhC with various cavity lengths can be seen in Figure 6(a). The 50 nm cavity length has one smaller emissive peak at lower wavelength. But, when the cavity length is increased to 100 nm then the emissive peak present at lower wavelength would increase in magnitude, and the spectral position of the peak moves

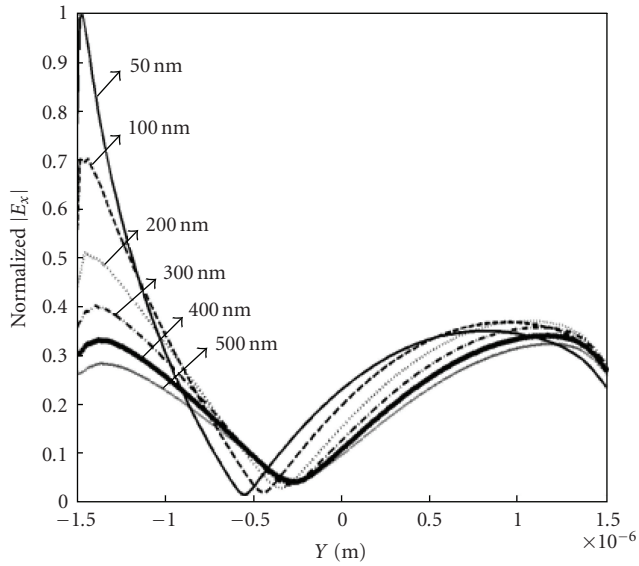


(a)

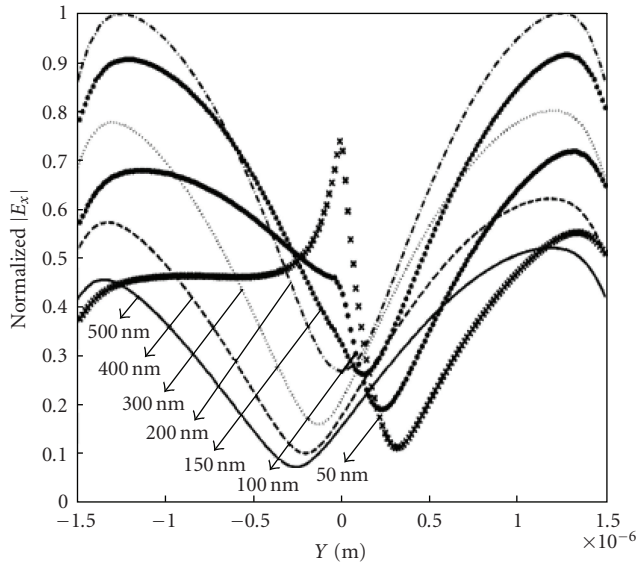


(b)

Figure 5: Normalized electric field $x$-component ($|E_x|$) at an incident wavelength of 6.35 $\mu$m along the channel center line of a gold grating in vacuum with (a) converging channel and (b) CDC for different gaps at the throat and grating parameters as $d$ = 3.5 $\mu$m, $a$ = 0.5 $\mu$m, and $t$ = 3.0 $\mu$m.

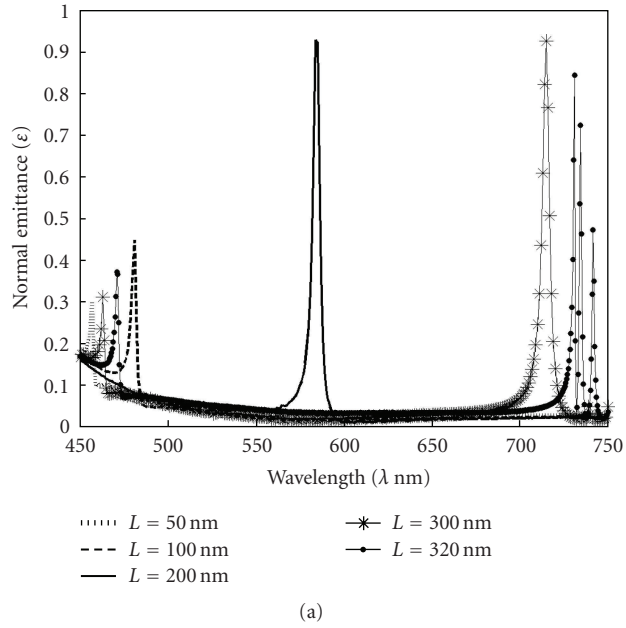


(a)

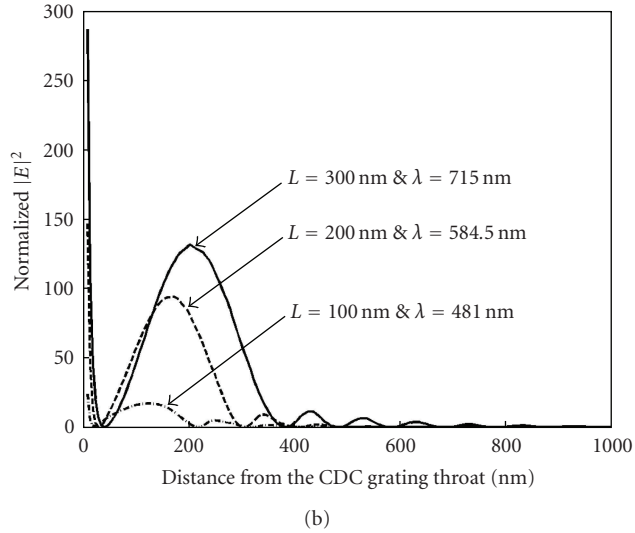


(b)

Figure 6: (a) Normal emittance spectrum with $p$ -polarization in vacuum for Ag CDC grating having the parameters $\Lambda$ = 250 nm, $h$ = 100 nm, $t$ = 100 nm, $g$ = 5 nm, and a photonic crystal having the parameters $a$ = 100 nm, $d_1 = d_2$ = 50 nm with cavity length $L$ = 50 nm, $L$ = 100 nm, $L$ = 200 nm, $L$ = 300 nm, $L$ = 320 nm; (b) electric field intensity distribution normalized to the incident along the line passing through the center of the CDC grating throat and into the photonic crystal with cavity lengths $L$ = 100 nm, $L$ = 200 nm, $L$ = 300 nm, and at respective normal emissive peak wavelengths.

to a bigger wavelength or has a red shift. When the cavity length increases further to 200 nm, then the only emissivity peak in the entire wavelength range of interest will have magnitude almost close to unity. The spectral position of the peak would have a further red shift. Figure 6(a) also shows that the 300 nm cavity length would have a high-emissive peak with an additional red shift. The spectrum of normal emittance for the 320 nm cavity length has several narrow peaks towards higher-band wavelength. The FWHM of the emissive peaks for the cavity length of 100 nm and 200 nm is the same and is around 4 nm. For the 300 nm cavity length, the FWHM is around 5 nm. Hence, Figure 6(a) shows that by varying the cavity length would result in the red shift of the emissive peak, and the FWHM of the peaks will be around 4-5 nm. In addition, according to the Wiener-Khinchin theorem the width of the emission spectrum peak

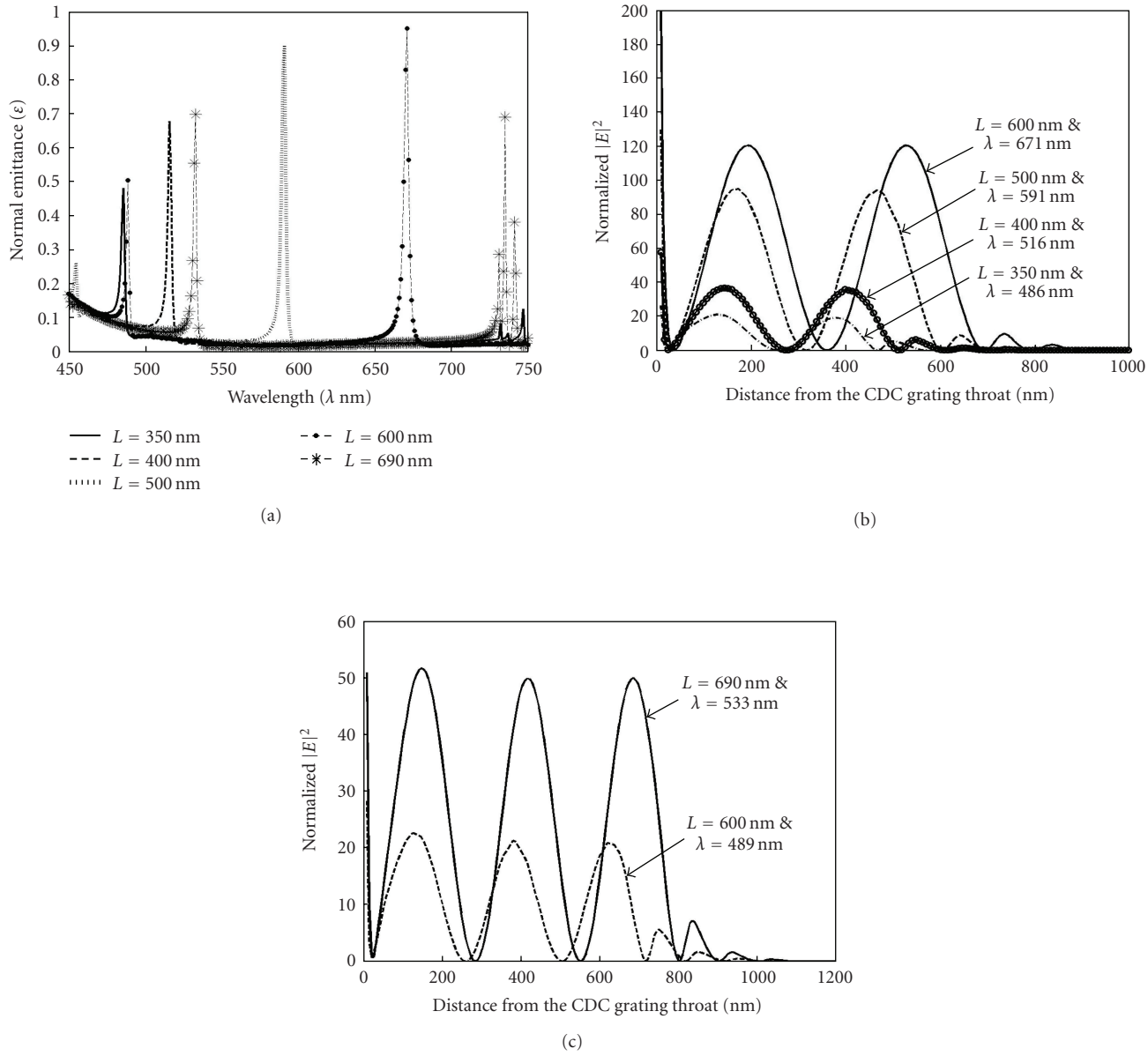


Figure 7: (a) Normal emittance spectrum with $p$-polarization in vacuum for Ag CDC grating having the parameters $\Lambda = 250$ nm, $h = 100$ nm, $t = 100$ nm, $g = 5$ nm, and a photonic crystal having the parameters $a = 100$ nm, $d_1 = d_2 = 50$ nm with varying cavity. Electric field intensity distribution normalized to the incident along the line passing through the center of the CDC grating throat and into the photonic crystal with (b) $L = 350$ nm, $L = 400$ nm, $L = 500$ nm, $L = 600$ nm, and at respective higher normal emissive peak wavelengths (c) $L = 600$ nm, $L = 690$ nm, and at respective lower-normal emissive peak wavelengths.

is inversely proportional to the coherence time [27]. This would then suggest that the cavity length is a good degree of freedom for achieving a tunable monochromatic thermal emitter for any desired wavelength with large temporal coherence. Figure 6(b) shows the electric field intensity distribution normalized to the incident along a line passing through the center of the CDC grating throat and into the 1D PhC. The intensity variation in the cavity seems to be like a first harmonic standing wave between the Ag grating and 1D PhC. The magnitude of the electric field intensity variation in the cavity increases with the cavity length, suggesting that the increase in emissive peak magnitude is due to the increase in the cavity resonance strength. Also, in 1D PhC, the electric field intensity decays within a smaller number of unit cells for larger cavity lengths. Hence, Figures 6(a)-6(b) show that the high absorption or emission is mainly due to the strong resonance in the cavity, and the condition for the resonant wavelength changes with the cavity length.

For a CDC, grating with 5 nm gap at the throat and 1D PhC with an increased cavity length from 320 nm to 350 nm has resulted in reducing the larger peaks present at higher wavelengths, as is evident in Figures 6(a) and 7(a). An additional increase in the cavity length to 400 nm has red shifted the spectral position of the emission peak present at lower

wavelengths, and also the magnitude of the emissivity peak has increased. In addition, at this cavity length there are no emission peaks near the larger wavelengths. When the cavity length is increased to 500 nm, then the emittance peak in the spectrum, as shown in Figure 7(a), has further red shifted and is almost in the middle of the wavelength range of interest. But, a closer look on the normal emission spectrum in the lower-wavelength range shows that there is a very small peak in the emission indicating that there could be an onset of even higher resonance in the cavity, as shown later. With the cavity length increased to 600 nm, the larger emission peak in the spectrum has further red shifted, and the smaller emission peak has gained in strength with a similar red shift. But the normal emittance spectrum, for the cavity length of 690 nm, has multiple emission peaks at higher wavelengths, and the emission peak at the lower wavelength has gained further in the magnitude with all of the emission peaks having red shift. Figure 7(b) shows the electric field intensity distribution normalized to the incident along the line passing through the center of the CDC throat and into the 1D PhC, at the spectral positions where the emission spectrum has large peaks for the cavity lengths of 350 nm, 400 nm, 500 nm, and 600 nm. From the figure, it can be seen that for all the cavity lengths considered, the resonance in the cavity is similar to a second harmonic resonance of a standing wave. Therefore, as the cavity length increases the spectral position of the emission peak due to the second harmonic resonance would have red shift, as observed similarly for the first harmonic resonance in Figures 6(a)-6(b). When the cavity lengths increase beyond a certain range, then there would be an onset of higher-order resonances at lower wavelengths and this is shown in Figure 7(c). In this figure, the normalized electric field intensity distribution is shown along the same line as the previous cases but for wavelengths where the spectral emission has peaks in the lower wavelength. The intensity distribution shows that the cavity has a resonance that is similar to a third harmonic standing wave.

In conclusion, we have shown that CDC metallic gratings with narrow and deep slits can have enhanced transmission resonances for wavelengths larger than the periodicity of the grating and have high-transmission resonances in a very narrow energy band. Also, it has been shown that a thermal emitter with a cavity surrounded by a CDC metallic grating and 1D PhC has very sharp spectral emission peak. This is mainly due to the strong resonances in the cavity supported by the CDC grating and 1D PhC. Thus, the emitter is tunable to various wavelengths with the choice of right materials along with the parameters of the grating, cavity length, and 1D PhC. Hence, the metallic subwavelength gratings with CDC can have important applications in optical communications, biological sensing, and optoelectronics.

## ACKNOWLEDGMENTS

Financial support from the US Air Force of Scientific Research (AFOSR) is greatly appreciated. This work was also supported in part by research grants from the US National Science Foundation. The authors appreciate the computer support from the Intel's Higher Education Program.

## REFERENCES

[1] W. L. Barnes, T. W. Preist, S. C. Kitson, and J. R. Sambles, "Physical origin of photonic energy gaps in the propagation of surface plasmons on gratings," *Physical Review B*, vol. 54, no. 9, pp. 6227–6244, 1996.

[2] S. C. Kitson, W. L. Barnes, and J. R. Samblas, "Full photonic band gap for surface modes in the visible," *Physical Review Letters*, vol. 77, no. 13, pp. 2670–2673, 1996.

[3] H. A. Bethe, "Theory of diffraction by small holes," *Physical Review*, vol. 66, no. 7-8, pp. 163–182, 1944.

[4] T. W. Ebbesen, H. J. Lezec, H. F. Ghaemi, T. Thio, and P. A. Wolff, "Extraordinary optical transmission through subwavelength hole arrays," *Nature*, vol. 391, no. 6668, pp. 667–669, 1998.

[5] C. Genet and T. W. Ebbesen, "Light in tiny holes," *Nature*, vol. 445, no. 7123, pp. 39–46, 2007.

[6] F. J. García-Vidal and L. Martín-Moreno, "Transmission and focusing of light in one-dimensional periodically nanostructured metals," *Physical Review B*, vol. 66, no. 15, Article ID 155412, 10 pages, 2002.

[7] J. A. Dionne, L. A. Sweatlock, H. A. Atwater, and A. Polman, "Planar metal plasmon waveguides: frequency-dependent dispersion, propagation, localization, and loss beyond the free electron model," *Physical Review B*, vol. 72, no. 7, Article ID 075405, 11 pages, 2005.

[8] H. J. Lezec and T. Thio, "Diffracted evanescent wave model for enhanced and suppressed optical transmission through subwavelength hole arrays," *Optics Express*, vol. 12, no. 16, pp. 3629–3651, 2004.

[9] Q. Cao and P. Lalanne, "Negative role of surface plasmons in the transmission of metallic gratings with very narrow slits," *Physical Review Letters*, vol. 88, no. 5, Article ID 057403, 4 pages, 2002.

[10] W. L. Barnes, W. A. Murray, J. Dintinger, E. Devaux, and T. W. Ebbesen, "Surface plasmon polaritons and their role in the enhanced transmission of light through periodic arrays of subwavelength holes in a metal film," *Physical Review Letters*, vol. 92, no. 10, Article ID 107401, 4 pages, 2004.

[11] J. A. Porto, F. J. García-Vidal, and J. B. Pendry, "Transmission resonances on metallic gratings with very narrow slits," *Physical Review Letters*, vol. 83, no. 14, pp. 2845–2848, 1999.

[12] R. Carminati and J.-J. Greffet, "Near-field effects in spatial coherence of thermal sources," *Physical Review Letters*, vol. 82, no. 8, pp. 1660–1663, 1999.

[13] C. Henkel, K. Joulain, R. Carminati, and J.-J. Greffet, "Spatial coherence of thermal near fields," *Optics Communications*, vol. 186, no. 1–3, pp. 57–67, 2000.

[14] A. V. Shchegrov, K. Joulain, R. Carminati, and J.-J. Greffet, "Near-field spectral effects due to electromagnetic surface excitations," *Physical Review Letters*, vol. 85, no. 7, pp. 1548–1551, 2000.

[15] P. J. Hesketh, J. N. Zemel, and B. Gebhart, "Organ pipe radiant modes of periodic micromachined silicon surfaces," *Nature*, vol. 324, no. 6097, pp. 549–551, 1986.

[16] E. A. Vinogradov, G. N. Zhizhin, A. G. Mal'shukov, and V. I. Yudson, "Thermostimulated polariton emission of zinc selenide films on metal substrate," *Solid State Communications*, vol. 23, no. 12, pp. 915–921, 1977.

[17] M. Kreiter, J. Oster, R. Sambles, S. Herminghaus, S. Mittler-Neher, and W. Knoll, "Thermally induced emission of light from a metallic diffraction grating, mediated by surface plasmons," *Optics Communications*, vol. 168, no. 1, pp. 117–122, 1999.

[18] J.-J. Greffet, R. Carminati, K. Joulain, J.-P. Mulet, S. Mainguy, and Y. Chen, "Coherent emission of light by thermal sources," *Nature*, vol. 416, no. 6876, pp. 61–64, 2002.

[19] P. Ben-Abdallah, "Thermal antenna behavior for thin-film structures," *Journal of the Optical Society of America A*, vol. 21, no. 7, pp. 1368–1371, 2004.

[20] E. D. Palik, Ed., *Handbook of Optical Constants of Solids*, Academic Press, Orlando, Fla, USA, 1985.

[21] J.-J. Greffet and M. Nieto-Vesperinas, "Field theory for generalized bidirectional reflectivity: derivation of Helmholtz's reciprocity principle and Kirchhoff's law," *Journal of the Optical Society of America A*, vol. 15, no. 10, pp. 2735–2744, 1998.

[22] J. D. Jackson, *Classical Electrodynamics*, John Wiley & Sons, New York, NY, USA, 3rd edition, 1999.

[23] D. R. Lide, *Handbook of Chemistry and Physics*, CRC Press, Cleveland, Ohio, USA, 58th edition, 1977.

[24] Y. Xie, A. R. Zakharian, J. V. Moloney, and M. Mansuripur, "Transmission of light through slit apertures in metallic films," *Optics Express*, vol. 12, no. 25, pp. 6106–6121, 2004.

[25] A. Lavrinenko, P. I. Borel, L. H. Frandsen, et al., "Comprehensive FDTD modelling of photonic crystal waveguide components," *Optics Express*, vol. 12, no. 2, pp. 234–248, 2004.

[26] X. Jiao, P. Wang, L. Tang, et al., "Fabry-Pérot-like phenomenon in the surface plasmons resonant transmission of metallic gratings with very narrow slits," *Applied Physics B*, vol. 80, no. 3, pp. 301–305, 2005.

[27] J. Le Gall, M. Olivier, and J.-J. Greffet, "Experimental and theoretical study of reflection and coherent thermal emission by a SiC grating supporting a surface-phonon polariton," *Physical Review B*, vol. 55, no. 15, pp. 10105–10114, 1997.

Hindawi Publishing Corporation
Active and Passive Electronic Components
Volume 2007, Article ID 63139, 4 pages
doi:10.1155/2007/63139

*Research Article*

# Transmission Properties of Metallic Grating with Subwavelength Slits in THz Frequency Region

**Dong Liang,[1] Qirong Xing,[1] Zhen Tian,[1] Changlei Wang,[1] Weili Zhang,[2] Jianqiang Gu,[1] Yanfeng Li,[1] Lu Chai,[1] Qingyue Wang,[1] and Aleksei Zheltikov[3]**

[1] *Center for THz waves, Ultrafast Laser Laboratory, College of Precision Instrument and Optoelectronics Engineering, and Key Laboratory of Opto-electronics Information and Technical Science (Ministry of Education), Tianjin University, Tianjin 300072, China*
[2] *School of Electrical and Computer Engineering, Oklahoma State University, Stillwater, OK 74078, USA*
[3] *Physics Department and International Laser Center, M.V. Lomonosov Moscow State University, Moscow 119992, Russia*

Received 11 September 2007; Accepted 10 October 2007

Recommended by Yalin Lu

This paper presents a fully experimental and theoretical study on transmission properties of a deep metallic grating with subwavelength slits in THz frequency region by using THz time domain spectroscopy (THz-TDS). The grating exposed to $p$-polarized incident wave exhibits enhanced nonresonant transmission in the long-wavelength region where the incident wavelength is larger than the grating period. Wood anomalies are observed when the wavelength is comparable to the grating period. Strict theory is given to explain the experimental results and the two are in good agreement. It is proposed that the Wood dips may be considered a criterion and a tool to judge and control the uniformity or fabricating accuracy of the grating period.



## 1. INTRODUCTION

Since 1998 when Ebbesen et al. discovered enhanced transmission of light through subwavelength hole arrays made in a thin metal film [1] there has been a renewed interest in exploiting dielectric response of subwavelength metallic periodic structures in different frequency regions including the optical [2–4], microwave [5], and terahertz region [6–12]. These structures possess abilities to confine incident light into a small spatial domain or to transmit light very efficiently. Thus, subwavelength metallic structures have great potential in subwavelength photonics apart from the fundamental physics.

In this letter, we experimentally investigated the transmission properties of a metallic grating with subwavelength slits by using THz-TDS [13]. The grating is exposed to $p$-polarized incident wave which is also called transverse magnetic (TM) with its electric field vector E perpendicular to the slit direction. The delay of the terahertz pulses and the nonresonant transmission spectrum through the samples were observed. Here, "nonresonant" corresponds to the case where the depth of the metallic grating in our experiment is much larger than the time window of the sampling terahertz radiation signal by using THz-TDS so that only a single pass of the terahertz pulses through the sample could be detected. Therefore, there was no Fabry-Perot-like resonant transmittance. Enhanced transmission in the long-wavelength was observed, as well as Wood anomalies which may act as a criterion and a tool to judge and control the fabricating accuracy of the sample grating. Theoretical explanation is then given by employing the effective refractive index of the metallic grating in the long wavelength and the nonuniformity of the grating period. Experimental results agree well with theoretical calculation.

## 2. EXPERIMENTAL SETUP AND RESULT

The sample was constructed using $250 \pm 5\,\mu$m thick steel blades, which were aligned vertically in a metallic frame with air spacers of the thickness of $70 \pm 15\,\mu$m. The grating was 3 mm in depth. In Figure 1, we show a schematic view of the sample with the parameters: the period of the grating ($p$), the width ($w$), and the depth ($h$) of the grating. The sample was placed between two off-axis parabolic mirrors in the collimated path of a standard THz-TDS with ZnTe-based emitter and detector. Linearly polarized and near single-cycle

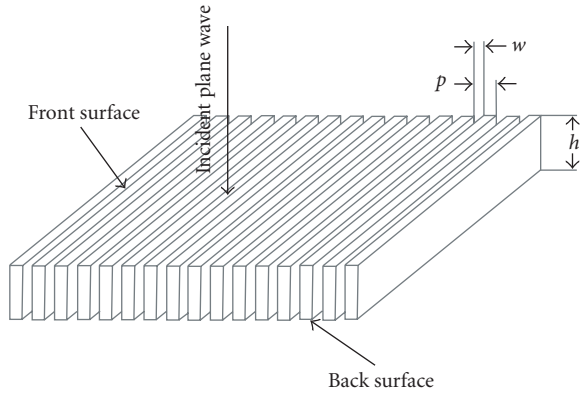


Figure 1: Schematic view of the metallic grating with subwavelength slits.

broadband terahertz pulses with a bandwidth from 0.3 to 3 THz were generated using 50 femtoseconds pulses from a mode-locked Ti: sapphire laser (average output power of 300 mW, repetition rate of 100 MHz).

The linearly polarized terahertz pulses through around 20 mm diameter aperture were impinged perpendicularly on the grating surface. All the system was sealed in a plastic box purged with pure nitrogen to mitigate absorption by water vapor.

The reference signal was obtained without the sample in the collimated beam path. We adjusted the metallic grating to make sure that the THz pulses were incident perpendicularly upon the grating surface in $p$-polarized state. Time domain signals with and without the metallic grating are given in Figure 2(a); while their corresponding spectra are shown Figure 2(b). Also, it can be seen in Figure 2(a) that the amplitude of transmission signal is nearly one third of that of the incident THz pulse, and that transmission pulse exhibits a time delay compared to the reference signal. The additional structures on the spectra curves in Figure 2(b) arise from absorption of the residual water vapor in the plastic box. The transmittance or transfer function of the grating can be derived by dividing the transmission spectrum by the reference spectrum as shown in Figure 2(c).

## 3. DISCUSSION

According to the modal expansion method proposed by Sheng et al. [14] and the effective Fabry-Perot model given in [15], and considering that metal can generally be treated as a perfect electrical conductor (PEC) in the THz frequency region, the expressions of transmittance or transfer function for normal incidence may be written as

$$T(\omega) = \frac{4\Gamma}{(1+f)^2}, \tag{1}$$

where $\Gamma = w/p$ is the area filling factor of the slits. Function $f$ can be written as

$$f = \Gamma \sum_{n=-\infty}^{+\infty} \frac{s_n^2}{\beta_n}, \tag{2}$$

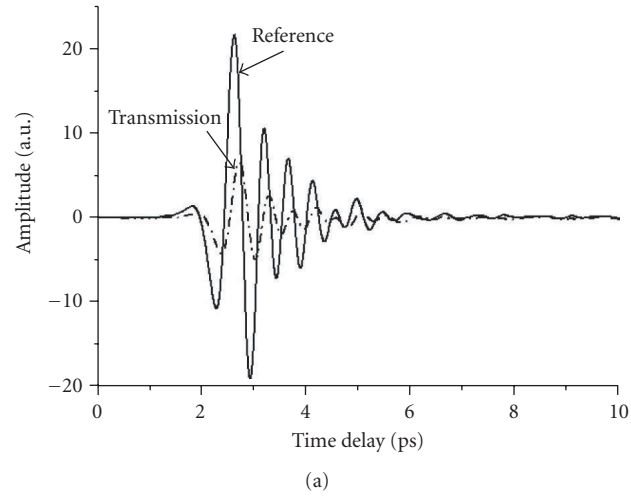


(a)

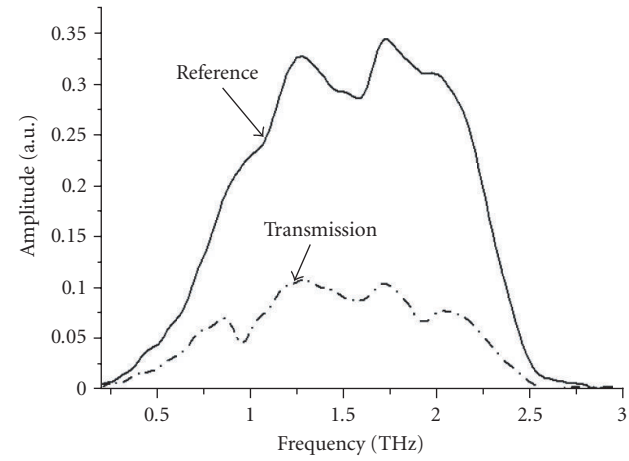


(b)

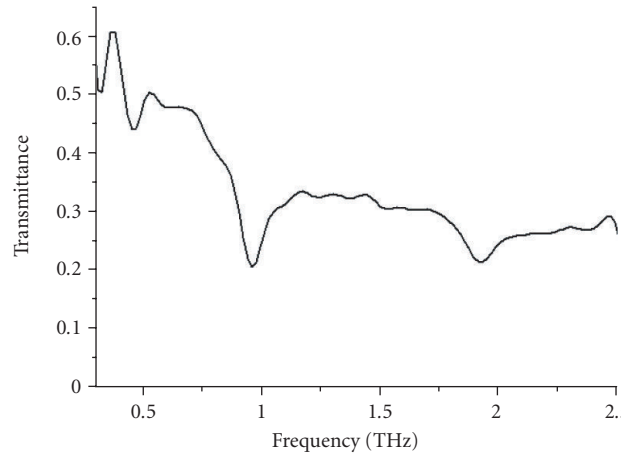


(c)

Figure 2: Nonresonant terahertz transmission properties of the grating exposed to $p$-polarized incident wave with grating period $p = 320 \pm 15\,\mu$m, slit width $w = 70 \pm 5\,\mu$m, and grating depth $h = 3$ mm. (a) Time domain traces of terahertz pulses. (b) Corresponding Fourier spectra. (c) Transmittance.

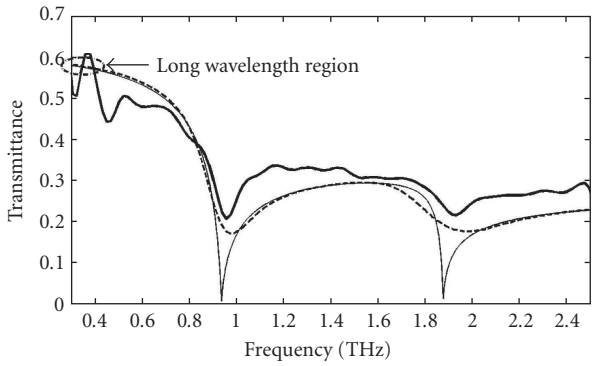


Figure 3: Comparison between experimental result and theoretical calculation. The thick solid line shows the experimental transmittance as indicated in Figure 2(c). The thin solid line denotes the theoretical transmittance of the grating with uniform period $p = 320\,\mu$m. The dashed line is a theoretical simulation assuming the grating period fulfills normal distribution with mean $320\,\mu$m and standard deviation $20\,\mu$m. The circle marks the transmittance in the long-wavelength region.

where $s_n$ with integer $n$ can be expressed as

$$s_n = \frac{\sin(k_0\gamma_n w/2)}{(k_0\gamma_n w/2)} \tag{3}$$

with

$$\gamma_n = n\frac{\lambda}{p}, \qquad \beta_n^2 = 1 - \gamma_n^2. \tag{4}$$

Regular spaced transmission minima, called Wood anomalies [16, 17], can be observed when a new diffraction order emerges from the surface, which is $\gamma_n = 1$ corresponding to Wood frequencies:

$$\nu_n = \frac{nc}{p}, \tag{5}$$

where $c$ and $n$ are the vacuum speed of light and an integer number, respectively. The experimental positions of the minima in the transmission spectrum agree well with the theoretical expectation as illustrated in Figure 2(c) with frequencies equal to 0.94 THz and 1.88 THz.

It should be pointed that the minima at frequencies 0.94 THz and 1.88 THz are expected to be zero according to (1), (2), and (4) as shown by the thin solid line in Figure 3 but the experimental result (thick solid line in Figure 3) only exhibits dips at such frequencies. The difference may be attributed to the nonuniformity of the period of the sample grating we fabricated. The grating period is randomly distributed in the vicinity of $320\,\mu$m with a fabrication error of $20\,\mu$m. As we know, the positions of the minima are subject to the grating period. Different periods correspond to different positions of the minima so that the comprehensive effect is to form dips in the transmittance curve other than zeros at Wood frequencies.

A model is proposed to demonstrate our point of view. Assuming the grating period fulfills normal distribution $N(p)$ with mean $p_0$ of $320\,\mu$m and standard deviation $\sigma$ of $20\,\mu$m, which is

$$N(p) = \frac{1}{\sqrt{2\pi}\sigma} e^{-(p-p_0)^2/2\sigma^2}. \tag{6}$$

Thus, the average transmittance $\overline{T}(\omega)$ can be rewritten as

$$\overline{T}(\omega) = \int_{-\infty}^{+\infty} N(p)T(\omega)dp, \tag{7}$$

where $T(\omega)$ is given by (1). The dashed line in Figure 3 denotes the curve of $\overline{T}(\omega)$ The theoretical simulation of the average transmittance demonstrates the formation of the dips at Wood frequencies. More importantly, the dips provide us a basis to judge the uniformity or fabricating accuracy of the metallic grating. The grating period can be judged by the position of the dips; and the fabricating accuracy may be judged by the width and depth of the dips. The narrower and deeper the dips are, the more accurate the grating period is.

The theoretical deviation from the experiment is mainly attributed to two reasons. The first is that the actual distribution of the grating period does not exactly fulfill the normal distribution. The second one is that the signal-to-noise ratio (SNR) increases when the frequency is below 0.5 THz, which leads to fluctuation of the transmittance in the long-wavelength region shown in Figure 3.

Then, we mainly focus on the long-wavelength region where the incident wavelength $\lambda$ is much larger than the grating period $p$. Therefore,

$$f = \Gamma \sum_{n=-\infty}^{+\infty} \frac{s_n^2}{\beta_n} = \Gamma\left(1 - \frac{2ip}{\lambda}\sum_{n=1}^{\infty}\frac{\mathrm{sinc}(n\pi\Gamma)}{n}\right) \approx \Gamma. \tag{8}$$

The transmittance can thus be approximated by the expression

$$T(\omega) = \frac{4\Gamma}{(1+\Gamma)^2} = \frac{4}{(1/\Gamma+1)^2}. \tag{9}$$

However, (9) implies that the transmittance is only related to the area filling factor of the slits in the long-wavelength region. By comparing (9) with the transmittance of a plane wave incident normally on a dielectric slab with refractive index $n$ and thickness of $h/n$,

$$T = \frac{4}{(n+1)^2}, \tag{10}$$

we can easily extract an effective refractive index $n = 1/\Gamma = p/w$, namely, the metallic grating with subwavelength slits can be treated as a dielectric slab. In fact, the effective index reflects the surface phase retardation of the metallic grating because the slits bring no time delay to the THz pulse compared to the reference signal. Assuming that the grating period keeps constant, the narrower the slits are, the more time the incident wave spends in getting into and out of the slits, which corresponds to a larger refractive index. As we can see in Figure 2(a), there is a time delay in the time traces of the transmitted THz pulses compared to reference traces, which is a proof of the surface retardation of the grating.

The transmission efficiency $t$ exceeds unit when normalized to the field directly impinging on the slits:

$$t = \frac{T(\omega)}{\Gamma} = \frac{4}{(1+\Gamma)^2}. \quad (11)$$

As indicated by (11), $t$ ranges from 1 to 4 for $0 < \Gamma < 1$. Obviously, the larger $\Gamma$ factor, the larger the effective index and the larger the transmission efficiency we can get. For $\Gamma \to 0$, $t$ tends to reach its maximum 4. This conclusion is different from the resonant transmission condition described in [1, 3]. For condition $\Gamma \to 1$, where the grating actually becomes air or vacuum, $t = 1$ corresponding to no enhanced transmission. For our sample grating with period $p = 320\,\mu$m and slit width $w = 70\,\mu$m, transmittance $T = 0.59$ agrees well with the experimental result shown by the circle in Figure 3.

## 4. CONCLUSION

The nonresonant transmission properties through a metallic grating with subwavelength slits in the THz frequency region were investigated. The grating was exposed to $p$-polarized incident THz radiation. The minima attributed to Wood anomalies were observed at wavelengths equal to fractions of the grating period. The nonuniformity of the grating period led to dips other than zeros at Wood frequencies. Normal distribution of the grating period was used to simulate the formation of the dips. These results provide us a criterion and a tool to judge and control the fabricating accuracy of the metallic grating. As for the long-wavelength region, an effective index of the grating was extracted based on the effective Fabry-Perot model to explain the enhanced transmission in this region. The experimental results are in good agreement with the theoretical calculations.

## ACKNOWLEDGMENTS

This work was partly supported by National Key Basic Research Special Foundation of China through Grant No.2007CB310408, National Natural Science Foundation of China (No.60578037), NSFC-RFBR program 2007-2008, and "985" program of Tianjin University.

## REFERENCES

[1] T. W. Ebbesen, H. J. Lezec, H. F. Ghaemi, T. Thio, and P. A. Wolff, "Extraordinary optical transmission through subwavelenght hole arrays," *Nature*, vol. 391, no. 6668, pp. 667–669, 1998.

[2] W. L. Barnes, A. Dereux, and T. W. Ebbesen, "Surface plasmon subwavelength optics," *Nature*, vol. 424, no. 6950, pp. 824–830, 2003.

[3] J. A. Porto, F. J. García-Vidal, and J. B. Pendry, "Transmission resonances on metallic gratings with very narrow slits," *Physical Review Letters*, vol. 83, no. 14, pp. 2845–2848, 1999.

[4] Q.-J. Wang, J.-Q. Li, C.-P. Huang, C. Zhang, and Y.-Y. Zhu, "Enhanced optical transmission through metal films with rotation-symmetrical hole arrays," *Applied Physics Letters*, vol. 87, no. 9, pp. 1–3, 2005.

[5] H. E. Went, A. P. Hibbins, J. R. Sambles, C. R. Lawrence, and A. P. Crick, "Selective transmission through very deep zero-order metallic gratings at microwave frequencies," *Applied Physics Letters*, vol. 77, no. 18, pp. 2789–2791, 2000.

[6] D. Qu, D. Grischkowsky, and W. Zhang, "Terahertz transmission properties of thin, subwavelength metallic hole arrays," *Optics Letters*, vol. 29, no. 8, pp. 896–898, 2004.

[7] J. G. Rivas, C. Schotsch, P. H. Bolivar, and H. Kurz, "Enhanced transmission of THz radiation through subwavelength holes," *Physical Review B*, vol. 68, no. 20, Article ID 201306, 4 pages, 2003.

[8] C. Janke, J. Gómez Rivas, C. Schotsch, L. Beckmann, P. Haring Bolivar, and H. Kurz, "Optimization of enhanced terahertz transmission through arrays of subwavelength apertures," *Physical Review B*, vol. 69, no. 20, Article ID 205314, 5 pages, 2004.

[9] G. Torosyan, C. Rau, B. Pradarutti, and R. Beigang, "Generation and propagation of surface plasmons in periodic metallic structures," *Applied Physics Letters*, vol. 85, no. 16, pp. 3372–3374, 2004.

[10] H. Cao and A. Nahata, "Influence of aperture shape on the transmission properties of a periodic array of subwavelength apertures," *Optics Express*, vol. 12, no. 16, pp. 3664–3672, 2004.

[11] A. K. Azad, J. Dai, and W. Zhang, "Transmission properties of terahertz pulses through subwavelength double split-ring resonators," *Optics Letters*, vol. 31, no. 5, pp. 634–636, 2006.

[12] Q. Xing, S. Li, Z. Tian, et al., "Enhanced zero-order transmission of terahertz radiation pulses through very deep metallic gratings with subwavelength slits," *Applied Physics Letters*, vol. 89, no. 4, Article ID 041107, 3 pages, 2006.

[13] L. Lang, Q. Xing, S. Li, F. Mao, L. Chai, and Q. Wang, "Experimental study on terahertz radiation," *Chinese Optics Letters*, vol. 2, no. 11, pp. 677–679, 2004.

[14] P. Sheng, R. S. Stepleman, and P. N. Sanda, "Exact eigenfunctions for square-wave gratings: application to diffraction and surface-plasmon calculations," *Physical Review B*, vol. 26, no. 6, pp. 2907–2916, 1982.

[15] F. J. García-Vidal and L. Martín-Moreno, "Transmission and focusing of light in one-dimensional periodically nanostructured metals," *Physical Review B*, vol. 66, no. 15, Article ID 155412, 10 pages, 2002.

[16] W. Wood, "On a remarkable case of uneven distribution of light in a diffraction grating spectrum," *Philosophical Magazine*, vol. 4, pp. 396–400, 1902.

[17] L. Rayleigh, "On the dynamical theory of gratings," *Proceedings of the Royal Society of London. Series A*, vol. A79, no. 532, pp. 399–416, 1907.

Hindawi Publishing Corporation
Active and Passive Electronic Components
Volume 2007, Article ID 52461, 7 pages
doi:10.1155/2007/52461

*Research Article*

# Compact Optical Waveguides Based on Hybrid Index and Surface-Plasmon-Polariton Guidance Mechanisms

**Min Yan and Min Qiu**

*Department of Microelectronics and Applied Physics, Royal Institute of Technology, Electrum 229, 16440 Kista, Sweden*

Received 13 October 2007; Accepted 9 November 2007

Recommended by Yalin Lu

Surface-plasmon-polariton (SPP) waveguides made of materials available in nature have, in general, been found to suffer from very high absorption loss when light confinement is beyond diffraction limit. In this paper, the possibility of combining both the conventional index-guiding and the SPP-guiding mechanisms together into one single waveguide is being explored. Such waveguides, expectedly, inherent the low-loss feature of all-dielectric waveguides as well as the superior mode field confinement possessed by SPP waveguides. By using experimentally ready materials, it is theoretically shown that compact metallodielectric waveguides can be designed with a $\sim 500 \times 500\,\text{nm}^2$ core size around the 1550 nm telecommunication wavelength. The examined waveguides can be interpreted as a gap SPP waveguide with an inner dielectric core. Compared to pure SPP waveguides, such hybrid waveguides have a comparable mode field size, but with significantly lower loss ($\sim$ 0.05 dB/$\mu$m for either quasi-TE or quasi-TM operation). Therefore they can be potentially deployed for a range of integrated photonic applications.



## 1. INTRODUCTION

Recently, there has been a revived interest on surface-plasmon-polariton (SPP) waveguides [1]. Such waveguides can confine light without a diffraction limit. Therefore, they are promising for applications in integrated optics. However, the propagation loss of almost all SPP waveguides is found to be inversely proportional to their mode field confinement (see, e.g., [2]). Most SPP waveguides proposed so far have their propagation lengths limited to only several micrometers once light is squeezed beyond the diffraction limit [3–5]. Such a high loss value ultimately prevents the waveguides from being deployed as integrated photonic circuits. In this paper, we look into a type of waveguides which guide light using both the dielectric index-guiding mechanism and the SPP effect. Such hybrid waveguides should inherit both the low-loss feature of all-dielectric waveguides as well as the superior mode confinement possessed by SPP waveguides. Compared to SPP waveguides, the proposed waveguides are expected to be able to achieve a comparable mode field confinement and lower propagation loss.

The waveguide to be examined, in a 1D slab limit, has a high-index dielectric core layer surrounded by low-index dielectric cladding layers, which is then further jacketed by metal claddings (see Figure 1(a)). When the distance between two metals (or metal gap size) is large enough, both TE and TM modes can be guided by the central high-index dielectric core. As the gap distance gets smaller, the effect of metal claddings becomes more evident. In fact, if the gap distance is close to the wavelength, the dielectric materials between metal claddings can be treated as an effective dielectric medium. Among the two modes, the TE mode will be cutoff if the metal gap is as short as half of the light wavelength (measured in the effective dielectric medium), while the TM mode is an SPP in nature and does not suffer from a diffraction limit. In practice, the waveguide in Figure 1(a) should be fabricated with a finite height. Figure 1(b) depicts the schematic cross-section of a corresponding planar 2D waveguide. Modes guided by the waveguide shown in Figure 1(b) are all hybrid. The first two modes have their major electric field polarized along either $x$ or $y$ direction. These two modes, therefore, can be referred to as quasi-TE or quasi-TM mode. Both index-guiding and SPP-guiding mechanisms, in general, contribute to the mode field confinement in such a waveguide. Without the central high-index core, the waveguides shown in Figures 1(a) and 1(b) correspond to the previously reported metal-insulator-metal (MIM) [6] and metal gap waveguides [4, 7–9], respectively. We will show that introduction of a high-index inner core will reduce metal absorption loss considerably for the TM mode (or quasi-TM

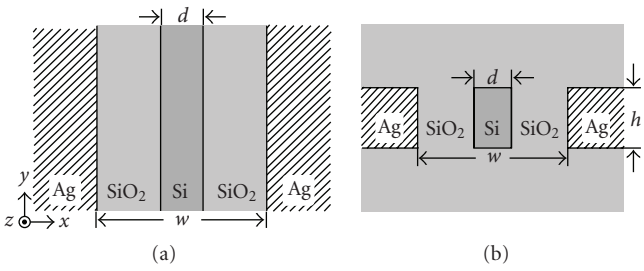


FIGURE 1: Schematic diagrams of the hybrid optical waveguide cross-sections. (a) 1D; (b) 2D.

mode for a 2D waveguide). At the same time, the TE mode (or quasi-TE mode) can be saved from cutoff, due to an increase in the effective index of the dielectric filling between two metal claddings. The optimum inner core thickness will be determined for achieving relatively low-loss quasi-TE or quasi-TM operation around 1550 nm wavelength, given a fixed metal cladding separation.

## 2. 1D ANALYSIS

We choose commonly available materials, namely silver (Ag), silica ($SiO_2$), and silicon (Si), for the current theoretical study. Throughout this paper, we have explicitly considered the material dispersion. The dielectric constant of silver is described in Drude model as

$$\epsilon(\mathrm{Ag}) = \epsilon_\infty - \frac{(\epsilon_0 - \epsilon_\infty)\omega_p^2}{\omega^2 + i\omega\gamma} \tag{1}$$

with $\epsilon_\infty = 4.017$, $\epsilon_0 = 4.896$, $\omega_p = 1.419 \times 10^{16}$ rad/s, and $\gamma = 1.117 \times 10^{14}$ rad/s. This Drude model is fitted according to the measured data from Palik's handbook [10]. The dielectric constant of silica is assumed to adhere to the well-recognized Sellmeier equation [11]. And similarly, a Sellmeier equation for silicon [10] is adopted. The operating wavelength is chosen to be within the range 1.2~2.0 $\mu$m, in which both silica and silicon are transparent.

We have employed a transfer-matrix method (TMM) for deriving modes propagating in the 1D waveguide. A time dependence of $\exp(j\omega t)$ is assumed throughout this study for harmonic electromagnetic field. The guided modes in a 1D waveguide can be separated into TE and TM two groups. We describe briefly the method for deriving TM modes. TE probelms can be handled accordingly. As a mode field in any single layer fulfills the wave equation in homogeneous material, and its general solution for the tangential field $\mathrm{H}_y$ can be written as

$$\mathrm{H}_{y,i} = A\exp(jk_{xi}x) + B\exp(-jk_{xi}x), \tag{2}$$

where $k_{xi}^2 = k_0^2\mu_{ri}\epsilon_{ri} - \beta^2$. Care should be taken for choosing the sign of the square root when deducing $k_{xi}$. $k_0$ is the free-space wave number. $\beta$ is the propagation constant which is, in general, complex. The effective mode index is defined as $n_{\mathrm{eff}} = \beta/k_0$. In (2), the first term denotes the left-propagating wave, and the second denotes the right-propagating wave. Another tangential field $\mathrm{E}_z$ can be derived as

$$\mathrm{E}_{zi} = A\frac{k_{xi}}{\omega\epsilon_i}\exp(jk_{xi}x) - B\frac{k_{xi}}{\omega\epsilon_i}\exp(-jk_{xi}x). \tag{3}$$

Equations (2) and (3) can be written compactly as

$$\begin{bmatrix}\mathrm{H}_{yi}\\ \mathrm{E}_{zi}\end{bmatrix} = \mathbf{M}_i\begin{bmatrix}A\\ B\end{bmatrix}. \tag{4}$$

As tangential fields are continuous across an material interface, by setting $x = x_i$ with $x_i$ the $i$th interface position, we can relate fields in two adjacent layers by

$$\begin{bmatrix}\mathrm{H}_{yi}\\ \mathrm{E}_{zi}\end{bmatrix} = \mathbf{M}_{xi}\begin{bmatrix}\mathrm{H}_{y,i+1}\\ \mathrm{E}_{z,i+1}\end{bmatrix}, \tag{5}$$

where $\mathbf{M}_{xi} = \mathbf{M}_i^{-1}\mathbf{M}_{i+1}$ is the transfer matrix. In this manner, the field in the leftmost layer can be related to that in the rightmost layer. By considering there is no right-propagating wave in the leftmost layer, and that there is no left-propagating wave in the rightmost layer, we can get a characteristic equation. $\beta$ values can be determined by solving for the roots of the equation.

Figures 2(a) and 2(b) show, respectively, the variations of the TE and TM modes in their $n_{\mathrm{eff}}$ and loss values as the Si layer thickness $d$ is changed from 0 to 500 nm while the distance between two metals $w$ is kept at 500 nm. Wavelength is at 1550 nm. For the first TE mode, its propagation loss decreases sharply by more than one order and reaches its minimum at 25.7 dB/mm around $d = 220$ nm. The loss increases gently as $d$ is further increased. In fact, the $\mathrm{TE}_0$ mode is close to cutoff at $d = 0$ nm, and introduction of the Si layer pushes the cutoff to longer wavelength, which explains the initial sharp decrease of loss. When $d$ reaches 275 nm, the second TE mode ($\mathrm{TE}_1$) begins to be guided. We can easily avoid this $\mathrm{TE}_1$ mode by letting $d < 275$ nm. The TM modes in Figure 2(b), in general, exhibits the same trend. The first two modes, $\mathrm{TM}_0$ and $\mathrm{TM}_1$, are the Fano mode pair in a conventional MIM slab waveguide. Among them, the $\mathrm{TM}_0$ mode does not experience cutoff even if $w$ decreases to a near-zero value. Propagation loss of this fundamental mode decreases as $d$ increases. The minimum loss of 22.6 dB/mm occurs when $d = 340$ nm. This drop in loss is attributed to the trapping of light in the Si layer, and therefore the interaction of mode with metal surfaces is reduced. Notice that all-Si filling results in a higher loss than that induced by all-$SiO_2$ filling. The $\mathrm{TM}_1$ mode is close to cutoff at $d = 0$, and it becomes better confined as the Si layer is introduced. However, the improvement is not as significant as that for the fundamental mode. The is due to the fact that there is a nodal line for the dominant field of the $\mathrm{TM}_1$ mode, which effectively expels light out of the Si layer. The $\mathrm{TM}_2$ mode appears at $d = 275$ nm, which experiences similar dispersion and loss behaviors as the $\mathrm{TE}_1$ mode. The Fano mode pair is seen to always exist regardless of $d$. However, we will show in the next section that the second Fano mode can be stripped off if a proper substrate and superstrate are deployed for a realistic 2D waveguide. Here $w = 500$ nm has been chosen for our

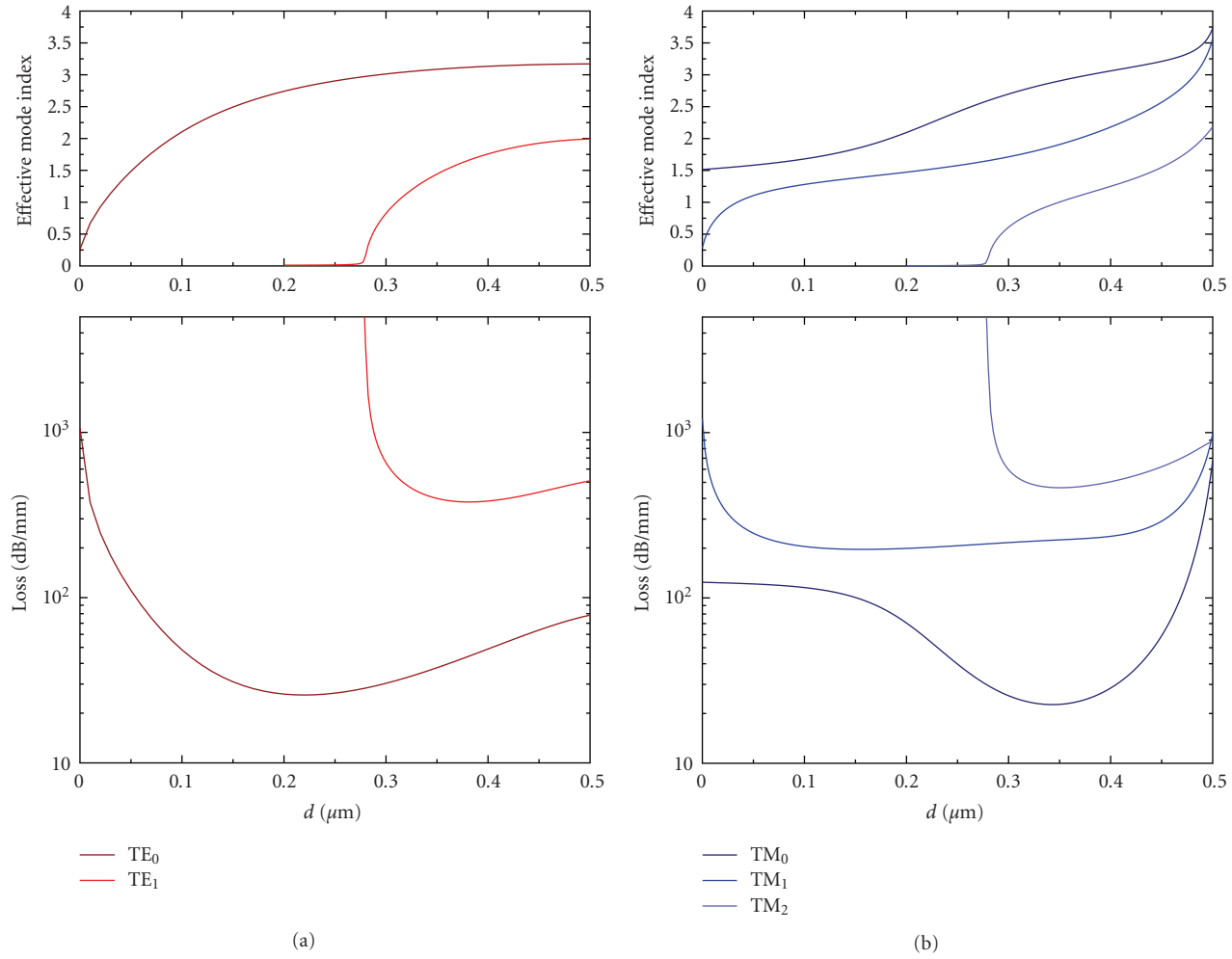


Figure 2: The variations of $n_{\text{eff}}$ (upper panel) and loss (lower panel) values for the TE (a) and TM (b) modes with respect to the Si layer thickness.

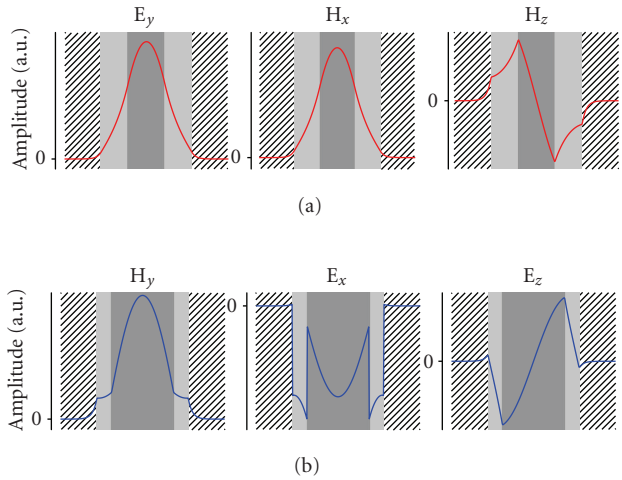


Figure 3: Modes supported by 1D waveguides. (a) Field components of the $TE_0$ mode guided by a slab waveguide with $d = 200$ nm. (b) Field components of the $TM_0$ mode guided in a slab waveguide with $d = 340$ nm. In both cases, the $z$ field component is the minor component.

case study. Although not shown in this paper, we point out that an extra Si layer only helps to reduce propagation loss when $w$ is larger than ~250 nm. When $w = 200$ nm, no TE mode is supported, and loss of the first TM mode increases monototically with $d$.

In Figure 3(a), we plot the fundamental TE mode at $d = 200$ nm, and the fundamental TM mode at $d = 340$ nm in Figure 3(b). It is evident that a major part of the light is trapped in the Si layer, which reduces the interaction of the modes with the metal claddings. The field penetration into metal claddings is limited to only tens of nanometers (so-called skin depth). Therefore, it is expected that such waveguides can be placed very close to each other without suffering from heavy cross-talks, which is key for achieving high-density optical integration.

## 3. 2D ANALYSIS

In 2D scenario, the waveguide in Figure 1(a) will have a finite height $h$. A substrate and a superstrate will be present below and above the waveguide, respectively, as shown in

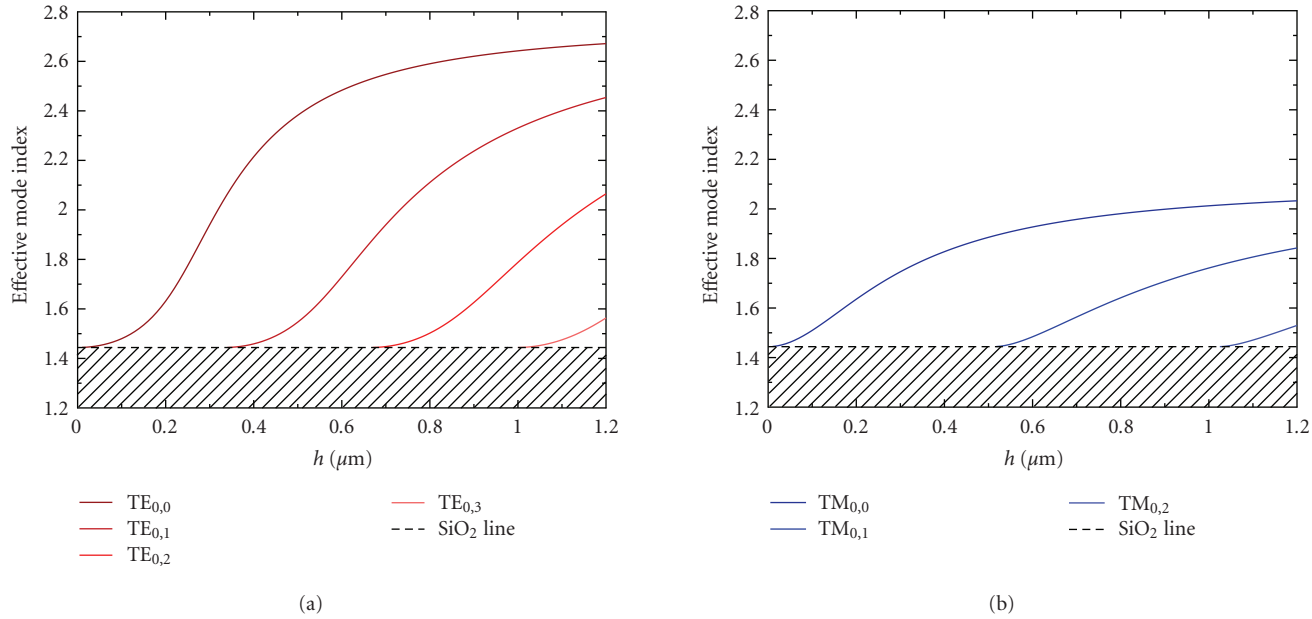


FIGURE 4: Dispersion of the TE (a) and TM (b) modes as the waveguide height is changed. $d = 200$ nm.

Figure 1(b). The guided mode is affected not only by the height of the planar waveguide but also by the indices of substrate and superstrate. Most importantly, the high-order modes that appear in 1D waveguides as shown in Figure 2 can be trimmed off for some adequate substrate or superstrate. For example, it is relatively simple to achieve low-loss single-mode quasi-TE operation at $\lambda = 1550$ nm, since a substrate and a superstrate made of $SiO_2$ ($n \approx 1.444$) would be sufficient to get rid of the $TE_1$ mode at $d = 200$ nm (see Figure 2(a)). For low-loss single-mode quasi-TM operation a substrate and a superstrate of index greater than ~2.0 (but less than 2.75) can be used to get rid of the odd Fano mode ($TM_1$) while $d$ can be kept around 340 nm (see Figure 2(b)). In the following, we will introduce two separate waveguides that are, respectively, intended for low-loss quasi-TE and quasi-TM operations.

### 3.1. Waveguide for quasi-TE operation

For low-loss quasi-TE operation, we let both substrate and superstrate be silica. $d$ is fixed at 200 nm. In 1D limit, the loss of the TE-mode will be as low as 26.1 dB/mm at 1550 nm wavelength (see Figure 2(a)). A further complication is on choosing an appropriate height $h$ to prevent nodal line from appearing in the vertical direction. Although a vector finite-element method (FEM) can be used to decide $h$ for single-mode operation, we have found the effective-index method (EIM) a much more efficient way to achieve the objective.

In EIM, a 2D planar waveguide is simplified to a horizontally-placed three-layer slab waveguide. For the particular waveguide shown in Figure 1(b), the upper and bottom layers of the corresponding simplified waveguide are simply $SiO_2$. The central layer has a refractive index which is the $n_{\text{eff}}$ value of the mode guided by the waveguide shown in Figure 1(a)). The EIM is noticed to have a reasonable accuracy, especially when wavelength is small (not shown). Figure 4(a) shows the geometric dispersion curves for the first four TE modes as $h$ is varied at $\lambda = 1550$ nm. We have only considered the $TE_0$ mode in Figure 2(a). It is seen that all high-order modes approach cutoff when $h$ decreases. When $h$ is less than ~400 nm, only one mode, that is, $TE_{0,0}$,[1] is supported. In the same manner, we have examined the geometric dispersions for the TM modes, as shown in Figure 4(b); and it is noticed that all high-order modes have been cutoff for $h <$ ~500 nm. Again, only $TM_0$ mode in Figure 2(b) is studied here. Although the second mode in Figure 2(b) ($TM_1$) has an $n_{\text{eff}} = 1.472768$, which is slightly larger than the refractive index of the substrate/superstrate (1.444024), the effective index of all modes in 1D case will be reduced as the height of the waveguide is reduced. It will be shown in the following paragraph that $TM_{1,x}$ modes will not be supported in our designed 2D waveguide by using an appropriate $h$.

Next, we use a vector FEM method to investigate explicitly a particular 2D planar waveguide that is optimized for low-loss quasi-TE operation. The advantages of FEM include its accurate definition of material boundaries as well as its adaptive meshing of the numerical domain. The waveguide under study has a height of 450 nm. The dispersion and loss curves for the first four modes are plotted in Figures 5(a) and 5(b). It is seen that the high-order $TM_{0,1}$ and $TE_{0,1}$ modes approach to their cutoffs at $\lambda \approx 1380$ nm and $\lambda \approx 1430$ nm, respectively. Hence the waveguide operates in single mode

[1] The first subscript in the mode designation corresponds to the number of nodal lines along $x$ direction, while the second subscript denotes the number of nodal lines along $y$ direction. Although the modes are all hybrid, for simplicity we still use the abbreviations "TE" and "TM."

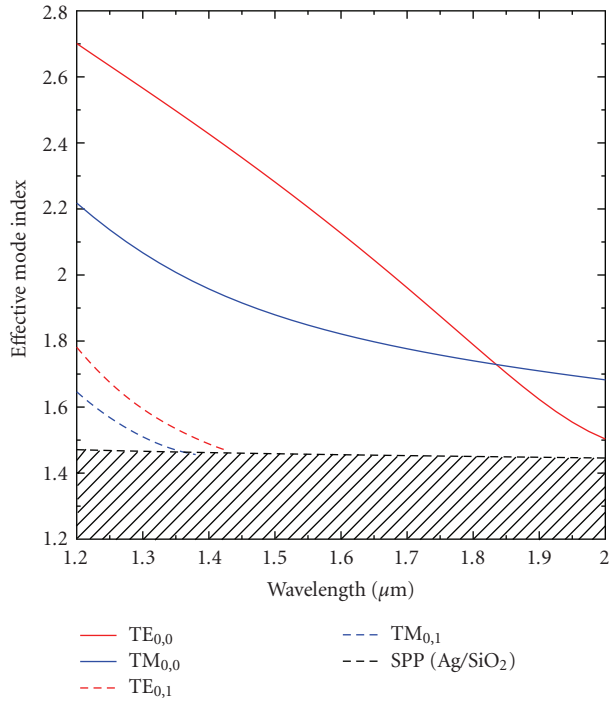


(a)

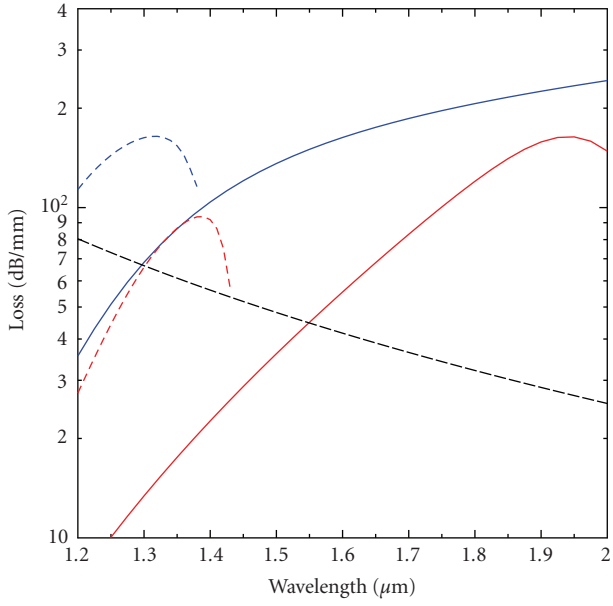


(b)

FIGURE 5: Dispersion (a) and loss (b) values for the first four modes guided by a 2D waveguide with $d = 200$ nm and $h = 450$ nm.

for each polarization at wavelength beyond ~1430 nm. At $\lambda = 1550$ nm, the waveguide is highly birefringent, with birefringence value (defined as $|n_{\text{eff}}^x - n_{\text{eff}}^y|$) as high as 0.3569. This indicates that the TM$_{0,0}$ and TE$_{0,0}$ modes, though both supported by the waveguide, will hardly interact with each other. A careful excitation by a linearly polarized light source will ensure that only one of the modes will be propagating down the waveguide. Generally speaking, the propagation

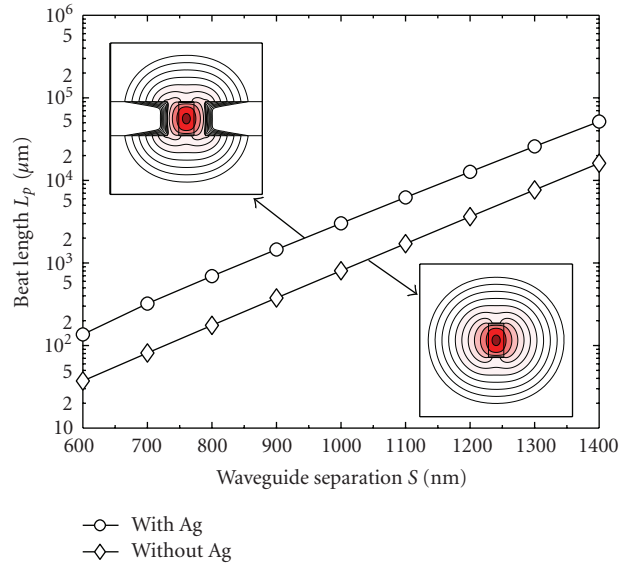


FIGURE 6: Beat length variation as a function of waveguide separation for the quasi-TE mode at $\lambda = 1550$ nm. The inset in the upper-left corner gives the TE$_{0,0}$ mode supported by an individual waveguide with metal cladding, while that in the bottom-right corner gives the same mode supported by a waveguide without metal cladding. The field contour lines are in 3 dB separation. The first contour line is an exception, which is at 90% of the maximum value. Domain size of the field plots: $2 \times 2\,\mu\text{m}^2$.

loss of the waveguide increases as $h$ is decreased. The propagation losses of both TE$_{0,0}$ and TM$_{0,0}$ modes are, in general, higher as compared to the pure 1D modes. The propagation loss of the TE$_{0,0}$ mode at 1550 nm is 44.9 dB/mm, and that for TM$_{0,1}$-like mode 150.1 dB/mm. The loss of the TE$_{0,1}$-like mode is almost equal to that of the SPP mode supported by a single Ag-SiO$_2$ surface (see Figure 5(b)), which is *in theory* impossible to be achieved by the coupled SPPs in MIM waveguides.

To know how strong two waveguides placed in parallel interact with each other, one needs to examine the beat length $L_p$ for the coupled supermodes. Beat length is defined as $L_p = 2\pi/|\beta_e - \beta_o|$, where $\beta_e$ and $\beta_o$ are propagation constant of the even and odd supermodes, respectively. The longer the $L_p$, the weaker the two waveguides interact. In Figure 6, we show the variation of beat length as a function of the waveguide separation $S$ (defined as the distance between core center to core center). The same curve is also derived for an identical waveguide but without the metal claddings. Both curves are approximately linear with the beat length represented in logarithmic scale. It is observed that the beat length is increased to their 3.5 times when metal claddings are present. With the same cross-talk requirement, waveguides with metal claddings can be put 23% closer as compared to without metal cladding. According to the coupled-moded theory, field overlapping of two waveguide modes (examined for each individual waveguide in separation) has direct effect on the coupling strength between two waveguides. From the field distribution of the mode supported by the hybrid waveguide (upper-left inset in Figure 6), it is not

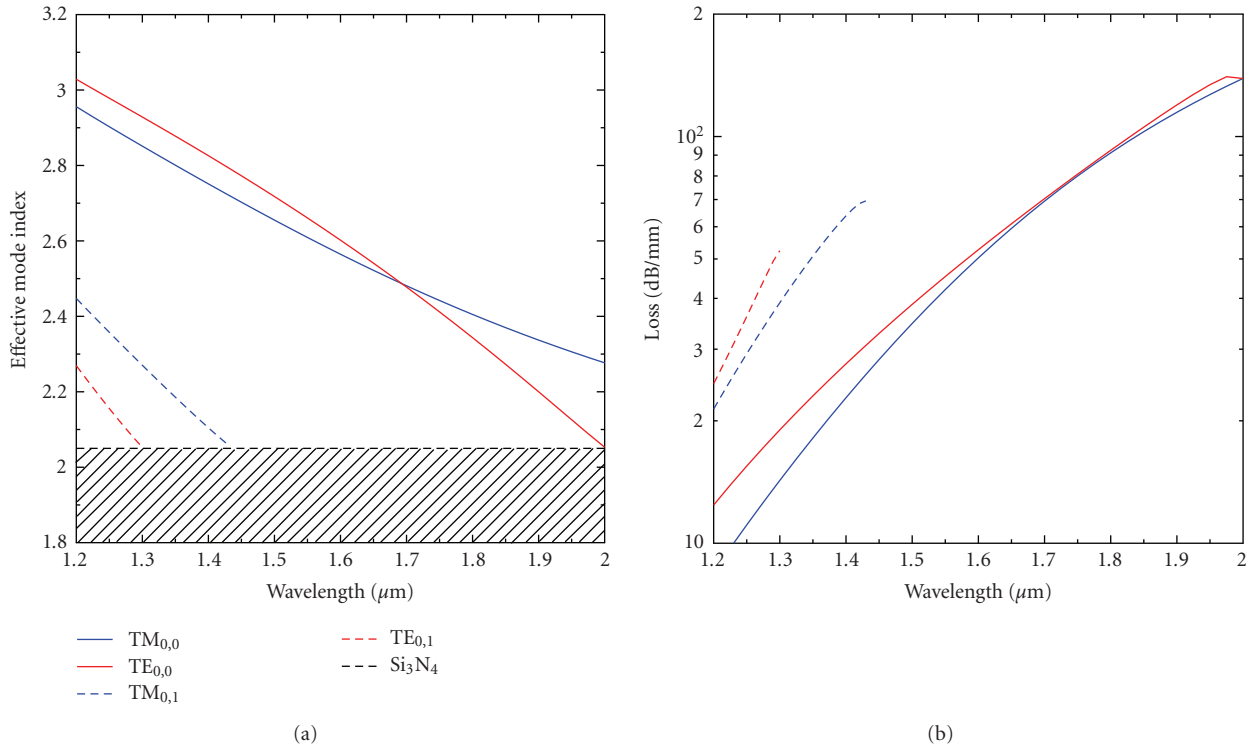


FIGURE 7: Dispersion (a) and loss (b) curves for guided modes in a waveguide with $d = 340$ nm and $h = 480$ nm. $\lambda = 1550$ nm.

difficult to understand that the field overlapping of such two modes will be smaller, as compared to waveguides without metal claddings.

### 3.2. *Waveguide for quasi-TM operation*

In this subsection, we look into waveguides that can operate with a relatively low-loss $TM_{0,0}$ mode. We follow the previous sub-section by setting $w = 500$ nm. To get rid of the odd Fano mode shown in Figure 2(b), we can choose Silicon Nitride ($Si_3N_4$, whose index is assumed to be 2.05 for $\lambda = 1.2{\sim}2\,\mu$m) as both the substrate and the superstrate. The $Si_3N_4$ layers are not placed in direct contact with the metals in order to avoid the high loss induced by Ag-$Si_3N_4$ SPP. In the present study, the $Si_3N_4$ materials 200 nm away from the metal surfaces. See Figure 8 insets for the waveguide cross-section.

First, according to Figure 2(b), we choose $d = 340$ nm in order to minimize the absorption loss. Again, using EIM we estimate that the height $h$ of the core layer should be kept less than 500 nm. In this investigation, we select $h = 480$ nm. In Figure 7, we show variation of the $n_{\text{eff}}$ and loss values with respect to wavelength. Similar to previously designed waveguide, the current waveguide supports both $TE_{0,0}$ and $TM_{0,0}$ two modes at $\lambda = 1.55\,\mu$m. Losses of the two modes are comparable at 45.3 dB/mm and 42.0 dB/mm, respectively. The birefringence at $\lambda = 1.55\,\mu$m is noticed to be 0.052, which is smaller as compared to the value possessed by the waveguide shown in the previous subsection. Still, the birefringence is significantly larger than those in commercial HI-BI fibers, which are normally in the order of $10^{-4}$. Therefore, a carefully launched polarization state is likely to be preserved at the output end of the waveguide.

To examine the coupling strength between such two waveguides placed in parallel, we show the beat length $L_p$ as a function of their separation $S$ in Figure 8. The same curve for an identical waveguide but without the metal cladding is also superimposed. With the metal cladding, the beat length is increased to its 5.0 times at $S = 600$ nm and 10.7 times at $S = 1400$ nm. At the same level of cross-talk requirement, the proposed hybrid waveguide can be placed up to 25% closer as compared to the waveguides without metal claddings (examined around $S = 700$ nm). The major magnetic field $H_y$ supported by an individual waveguide for both with and without metal claddings are shown as insets in Figure 8. Comparing the two fields, it can be seen that the mode guided by the hybrid waveguide is better confined laterally due to the presence of metal claddings. In fact, the major field components $H_y$ and $E_x$ are antiresonant with the horizontal Ag-$SiO_2$ interfaces; therefore, a quicker field decay along the surfaces is resulted.

## 4. DISCUSSION AND CONCLUSION

The losses of the designed waveguides are in the range of 40∼50 dB/mm. Such a loss value allows a signal to be transmitted for a ∼100 $\mu$m distance before its power is dropped to its $1/e$. Since the cross-sections of the waveguides are around $0.5 \times 0.5\,\mu\text{m}^2$, the functioning waveguides have a length-to-cross-section aspect ratio of ∼200. This value is reasonably

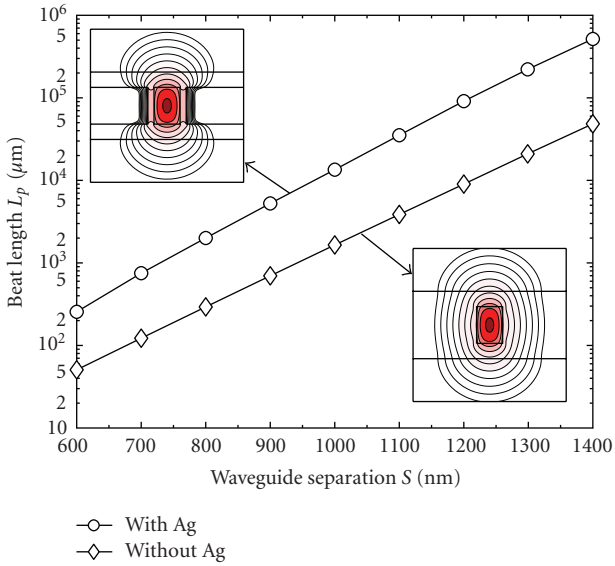


FIGURE 8: Beat length variation as a function of waveguide separation for the quasi-TE mode at $\lambda = 1550$ nm. The inset in the upper-left corner gives the $TM_{0,0}$ mode supported by an individual waveguide with metal cladding, while that in the bottom-right corner gives the mode supported by a waveguide without metal cladding. The field contour lines are in 3 dB separation. The first contour line is an exception, which is at 90% of the maximum value. Domain size of the field plots: $2 \times 2\,\mu m^2$.

large for achieving a wide varieties of photonic applications (e.g., ring resonators, couplers, etc.).

The designed waveguides have confirmed that it is possible to obtain both reasonably low-loss propagation as well as good confinement by combining both index-guiding and SPP-guiding mechanisms. There are several ways to achieve even lower loss, probably at the expense of field confinement. First, the propagation loss can be reduced by using some dielectric material with a lower epsilon value (e.g., air), in replacement of the $SiO_2$ material in the proposed structures. A drop in propagation loss is expected because that the SPP guided by an Ag-air interface has a significantly lower loss than that guided by an Ag-$SiO_2$ interface. However, planar waveguides with their core exposed in air are relatively more vulnerable to environmental changes. Notably, contamination of water molecules will affect the guided modes significantly. Second, propagation loss can be drastically reduced if the gap size is allowed to increase to some higher value. Finally, waveguides with lower loss may be possible by applying the same design methodology to other waveguide structures, other than based on the MIM structure.

In conclusion, we have proposed the deployment of waveguides which propagate light by both index-guiding and SPP-guiding principles. With the hybrid guidance mechanism, it is possible to realize low-loss, compact-optical waveguides using commonly available materials. As a simple illustration, we have designed waveguides with their cross-sections at $\sim 500 \times 500\,nm^2$ functioning around the 1550 nm telecommunication wavelength. The waveguides can be optimized for low-loss quasi-TE or quasi-TM guidance. An increase in packaging density by up to 25% is observed compared to using waveguides without metal claddings. The waveguide in quasi-TM operation deserves some special attention, since a down-tailoring of the waveguide does not lead to a cutoff of the guided quasi-TM mode, even when the waveguide's high-index inner core ceases to exist. We are currently exploring the possibility of coupling light efficiently from a waveguide proposed in this paper to a deep-subwavelength metal-gap SPP waveguide without an inner dielectric core though such a tailoring.

## ACKNOWLEDGMENTS

This work is supported by the Swedish Foundation for Strategic Research (SSF) through the INGVAR program, the SSF Strategic Research Center in Photonics, and the Swedish Research Council (VR).

## REFERENCES

[1] H. A. Atwater, "The promise of plasmonics," *Scientific American*, vol. 296, no. 4, pp. 56–63, 2007.
[2] P. Berini, "Figures of merit for surface plasmon waveguides," *Optics Express*, vol. 14, no. 26, pp. 13030–13042, 2006.
[3] M. Yan and M. Qiu, "Guided plasmon polariton at 2D metal corners," *Journal of the Optical Society of America. B, Optical Physics*, vol. 24, no. 9, pp. 2333–2342, 2007.
[4] L. Liu, Z. Han, and S. He, "Novel surface plasmon waveguide for high integration," *Optics Express*, vol. 13, no. 17, pp. 6645–6650, 2005.
[5] F. Kusunoki, T. Yotsuya, J. Takahara, and T. Kobayashi, "Propagation properties of guided waves in index-guided two-dimensional optical waveguides," *Applied Physics Letters*, vol. 86, no. 21, Article ID 211101, 3 pages, 2005.
[6] J. A. Dionne, L. A. Sweatlock, H. A. Atwater, and A. Polman, "Plasmon slot waveguides: towards chip-scale propagation with subwavelength-scale localization," *Physical Review B—Condensed Matter and Materials Physics*, vol. 73, no. 3, Article ID 035407, 9 pages, 2006.
[7] G. Veronis and S. Fan, "Guided subwavelength plasmonic mode supported by a slot in a thin metal film," *Optics Letters*, vol. 30, no. 24, pp. 3359–3361, 2005.
[8] D. F. P. Pile, T. Ogawa, D. K. Gramotnev, et al., "Two-dimensionally localized modes of a nanoscale gap plasmon waveguide," *Applied Physics Letters*, vol. 87, no. 26, Article ID 261114, 3 pages, 2005.
[9] L. Chen, J. Shakya, and M. Lipson, "Subwavelength confinement in an integrated metal slot waveguide on silicon," *Optics Letters*, vol. 31, no. 14, pp. 2133–2135, 2006.
[10] E. D. Palik, *Handbook of Optical Constants of Solids*, Academic Press, Boston, Mass, USA, 1985.
[11] G. Agrawal, *Nonlinear Fiber Optics*, Academic Press, Boston, Mass, USA, 3rd edition, 2001.

Hindawi Publishing Corporation
Active and Passive Electronic Components
Volume 2007, Article ID 78602, 5 pages
doi:10.1155/2007/78602

*Research Article*

# Subwavelength-Diameter Silica Wire and Photonic Crystal Waveguide Slow Light Coupling

**Ziyang Zhang,[1] Ulf Andersson,[2] and Min Qiu[1]**

[1] *Department of Microelectronics and Applied Physics, Royal Institute of Technology (KTH), Electrum 229, 164 40 Kista, Sweden*
[2] *Center for Parallel Computers, Royal Institute of Technology (KTH), 100 44 Stockholm, Sweden*

Received 28 August 2007; Accepted 21 October 2007

Recommended by Yalin Lu

Counter-directional coupling between subwavelength-diameter silica wire and single-line-defect two-dimensional photonic crystal slab waveguide is studied numerically using parallel three-dimensional finite-different time-domain method. By modifying silica wire properties or engineering photonic crystal waveguide dispersion band, the coupling central wavelength can be moved to the slow light region and the coupling efficiency improves simultaneously. One design gives 82% peak power transmission from silica wire to photonic crystal waveguide over an interacting distance of 50 lattice constants. The group velocity is estimated as 1/35 of light speed in vacuum.



## 1. INTRODUCTION

There have been extensive studies of slow light in two-dimensional photonic crystal slab waveguide (PCSW) [1–3]. The applications include compact delay lines for photonic signal processing, dispersion management, enhanced light/matter interaction for lasing, and so forth. To couple slow light efficiently, a special interface or a mode converter is usually needed between PCSW and connected dielectric waveguides [4, 5]. Alternatively, we investigate the evanescent counter-directional coupling between subwavelength-diameter silica wire ($SiO_2$-Wr) and PCSW for slow light generation. A convenient way to draw such $SiO_2$-Wrs can be found in [6]. There has been previous work on this type of directional coupler [7, 8]. However, the models are mostly two-dimensional and the coupling at slow light region is not investigated. In this paper, we show that the coupling efficiency can be improved greatly when the coupling central wavelength (work point) is moved to the slow light region. The work point can be altered either by changing the refractive index of $SiO_2$-Wr, or more realistically by modifying the geometries of PCSW. Coupled mode theory is applied to compare the group velocity, coupling efficiency, and coupling bandwidth of the modified PCSWs.

The numerical work is done by parallel three-dimensional finite-difference time-domain method (P3D FDTD). The code, MBfrida, is part of the GEMS suite from Efield AB [9] and is fully parallelized using message passing interface. The simulations are run on Lucidor cluster located at Center for Parallel Computers, Royal Institute of Technology (KTH), Sweden.

## 2. COUNTER-DIRECTIONAL COUPLING BETWEEN SILICA WIRE AND PHOTONIC CRYSTAL WAVEGUIDE

The schematic of $SiO_2$-Wr and PCSW directional coupler is shown in Figure 1. The silicon photonic crystal slab has index 3.6 and thickness $0.6a$, where $a$ is the lattice constant. The air-hole diameter is $0.6a$. PCSW is formed by removing one row of air holes along ΓK direction. The PCSW dispersion band can be modified by changing $\delta$, that is, varying the width of the waveguide. For $\delta = 0$, we name the waveguide $PCSW_0$. The index of $SiO_2$-Wr is 1.5 and the diameter is $1\,\mu$m. We choose to place $SiO_2$-Wr 500 nm above the slab. $SiO_2$-Wr and $PCSW_0$ are center-aligned in $x$ and go parallel along $y$. $SiO_2$-Wr can also be placed on the side of $PCSW_0$ [7]. However, this side coupling risks generating unwanted photonic crystal surface modes [10] and furthermore lowering the coupling efficiency. Another issue is that the photonic crystal lattice between the line-defect and the silica wire is limited to only a few row of air holes in order to achieve sufficient side coupling, This might weaken the in-plane light confinement of $PCSW_0$ and lead to larger propagation loss.

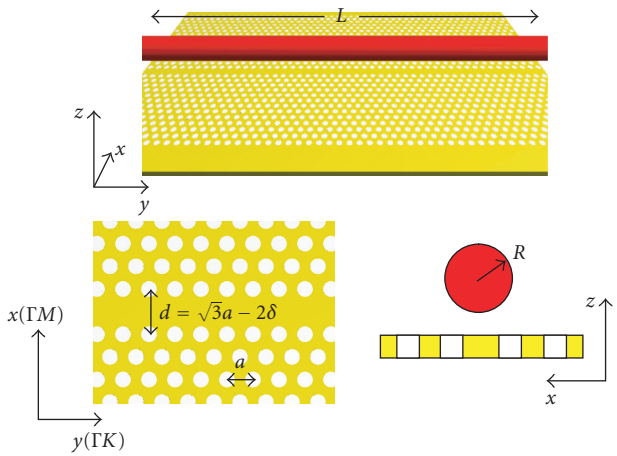


FIGURE 1: Schematic of $SiO_2$-Wr and PSCW directional coupler.

Figure 2(a) shows the band diagram of $PCSW_0$, calculated using plane wave expansion method (PWE). The zero-order even mode is shown in diamond marker. The fundamental $SiO_2$-Wr mode dispersion curve is approximately a straight line within the band-gap. Cross point $P$ is the work point, where $PCSW_0$ and $SiO_2$-Wr share the same propagation constant. The opposite slope sign of the two dispersion curves decides that the evanescent coupling between these two waveguides is counter-directional. Note that since the system is symmetric along $x$, there is no coupling between fundamental $SiO_2$-Wr mode and first-order odd $PCSW_0$.

The P3D FDTD transmission simulation is shown in Figure 2(b) with $L = 50a$. The peak power transmission is only 25%, indicating a small coupling coefficient. Also note that the central frequency from P3D FDTD simulation differs slightly from the $P$ point in Figure 2(a). This discrepancy may result from numerical errors in P3D FDTD and PWE methods. Another reason is that the actual dispersion curves for both $SiO_2$-Wr and $PCSW_0$ are slightly modified for the weakly-coupled system compared to their unperturbed counterparts.

## 3. SLOW LIGHT GENERATION

We would like to see the coupling behaviour when the work point $P$ moves to the flat band region of PCSW. One easy solution is to change the $SiO_2$-Wr properties such as wire diameter and material refractive index. For numerical tests we keep the diameter of $SiO_2$-Wr as 1 $\mu$m and change its refractive index from 1.5 to 1.92, 2.0, and 2.1, respectively. The work points move from $P_0$ to $P_1$, $P_2$, and $P_3$ accordingly, as shown in Figure 3(a). The power simulations are shown in Figure 3(b). As the work point moves further into the slow light region, the peak power transmission goes up, indicating an increase in the coupling coefficient. The coupling bandwidth goes down as the line-width of the transmission spectra decreases.

This interesting phenomenon leads us to more investigation. We keep the index of $SiO_2$-Wr as 1.5 while modifying PSCW geometry in order to achieve flat-band operation at the coupling point. There are a number of ways to modify the dispersion curve of PSCW. After many trials, we find that one effective way is to reduce the PSCW width $d$. As shown in Figure 1, $d = \sqrt{3}a - 2\delta$, and we increase $\delta$ from 0 to $0.1a$, $0.2a$, and $0.3a$. Accordingly we name the waveguides as $PCSW_0$, $PCSW_1$, $PCSW_2$, and $PCSW_3$. The band diagrams for $PCSW_1$, $PCSW_2$, and $PCSW_3$ are shown in Figure 4. Note that higher-order modes are pulled up from the lower-band edge for these waveguides.

Figure 5 shows the normalised transmission for the modified waveguides in comparison to $PCSW_0$. The coupling length $L$ remains $50a$ for all cases. When $\delta = 0.2a$, the peak transmission reaches 82%. When $\delta = 0.3a$, the coupling with higher-order even mode comes into the frequency window ($Q_{III}$). From $P_0$ to $P_{II}$, we have again observed an improvement of coupling efficiency when the work point moves to the slow light region. At work point $P_{III}$, the power transmission drops to 58%, despite an increase of group index compared to $P_{II}$. To understand the coupling behavior better, we have carried out the coupled mode analysis for this system.

## 4. COUPLED MODE ANALYSIS

We assume weak coupling between $SiO_2$-Wr mode and PCSW zero-order even mode. At the work point ($\omega = \omega_0$), the power of $SiO_2$-Wr mode, $P_A$, and the power of PCSW zero-order even mode, $P_B$, are related by [11]

$$P_A(y) = P_A(0)\frac{\cosh^2[\kappa(y-L)]}{\cosh^2(\kappa L)}, \qquad P_B(y) = P_A(0)\frac{\sinh^2[\kappa(y-L)]}{\cosh^2(\kappa L)}, \quad 0 \le y \le L. \tag{1}$$

$P_A(0)$ is the input light power from $SiO_2$-Wr and $P_B(0)$ is the backward transferred (output) power in $PCSW_0$ at the initial point. The coupling coefficient $\kappa$ is determined by $SiO_2$-Wr and PCSW vertical spacing as well as their individual mode profile. We define the coupling efficiency $\eta$ as

$$\eta = \frac{P_B(0)}{P_A(0)} = \frac{\sinh^2(\kappa L)}{\cosh^2(\kappa L)}. \tag{2}$$

The coupling efficiency depends on the product of $\kappa$ and interacting distance $L$. When $\kappa L \to \infty$, $\eta \to 1$. For finite $\kappa$, complete power transfer from $SiO_2$-Wr to PCSW is possible when their coupling distance $L$ goes to infinity.

To verify the validity of weak coupling assumptions and (2), we take $\delta = 0.2a$, which gives the highest peak transmission, and vary $L$ from $20a$ to $30a$, $40a$, $50a$, and $70a$. Since the vertical coupling structure is fixed, $\eta$ is only dependant on $L$. We run simulations for all cases and take $\eta$ as the peak value of the power transmission spectra. The values are plotted in Figure 6(a) as discrete data points. The theoretical relation from (2) is plotted as solid curve in Figure 6(a). The average deviation of the simulation values from the theoretic curve is only 3.3%, indicating a good agreement.

Figure 6(b) gives the $E_x$ mode profile in the central slab plane for $PCSW_2$ waveguide first-order even mode ($P_{II}$) generated from the counter-directional coupling. The power

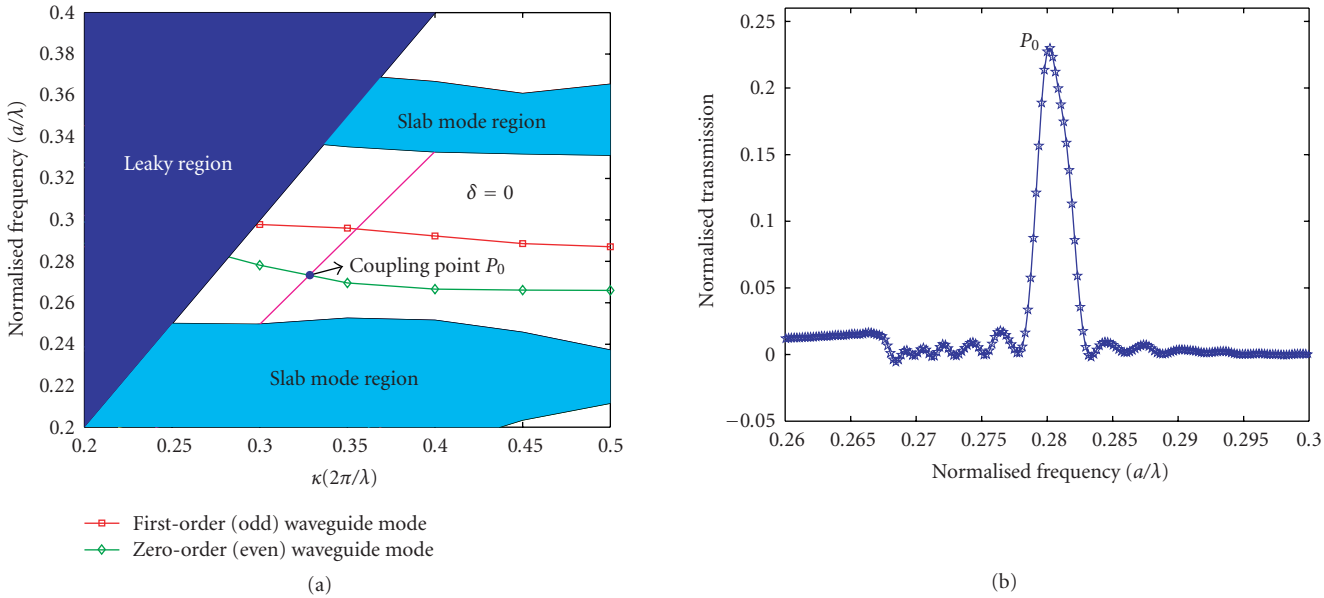


FIGURE 2: (a) Band diagram of $PCSW_0$. The blue curve with diamond marker shows the zero-order even $PCSW_0$ mode. The coupling point is indicated as the blue dot $P$. Due to modal and structural symmetry, $SiO_2$-Wr mode will not couple with the first-order odd mode of $PSCW_0$ (red curve with square marker). (b) Normalised power transmission in $PSCW_0$ over coupling distance of 50 lattice constants.

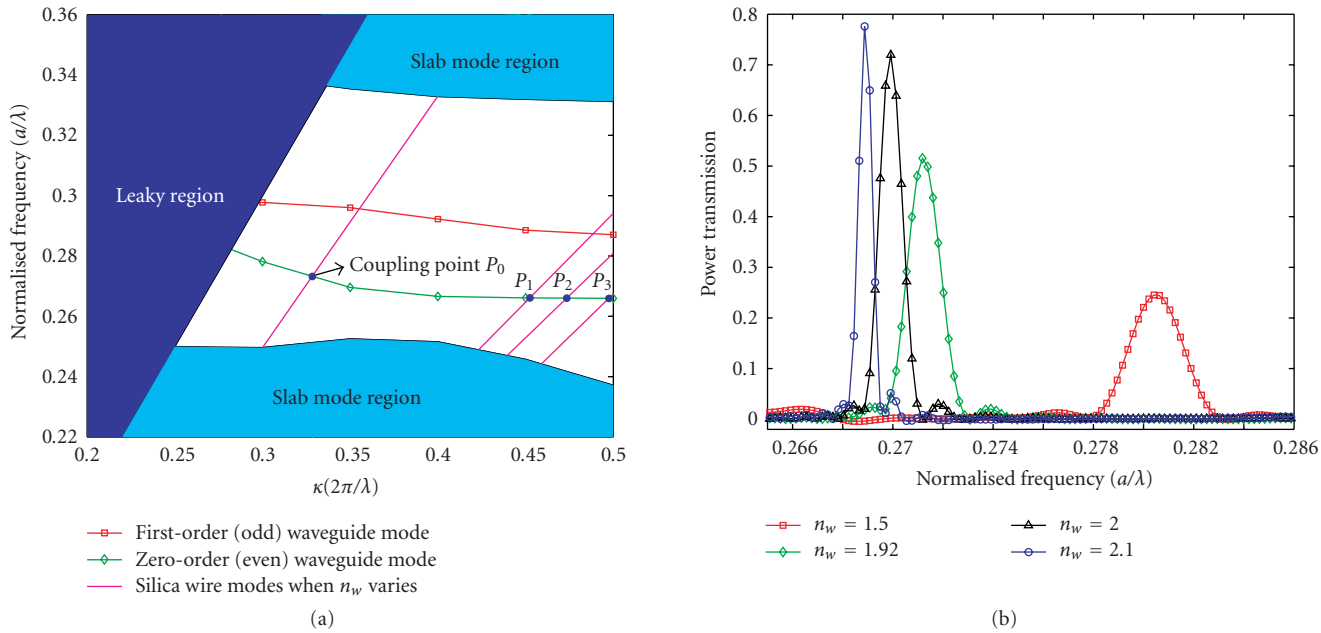


FIGURE 3: (a) The coupling points shift when the refractive index ($n_w$) of $SiO_2$-Wr varies from 1.5 ($P_0$) to 1.92 ($P_1$), 2.0 ($P_2$), and 2.1 ($P_3$). (b) The transmission comparison. As the coupling point moves to the flat band region, the coupling efficiency goes up while the bandwidth shrinks.

TABLE 1: Comparison of $PCSW_{0-3}$

| | $PCSW_0$ | $PCSW_1$ | $PCSW_2$ | $PCSW_3(P_{III})$ |
|---|---|---|---|---|
| Peak transmission $\eta$ | $\eta_0 = 0.25$ | $\eta_1 = 0.46 = 1.84\eta_0$ | $\eta_2 = 0.81 = 3.24\eta_0$ | $\eta_3 = 0.58 = 2.32\eta_0$ |
| Coupling bandwidth $\Delta\omega$ ($a/\lambda$) | 0.0029 | 0.0020 | 0.0013 | 0.0008 |
| Group index $n_g$ | 5.6 | 12.1 | 35.0 | 40.2 |
| Coupling coefficient $\kappa$ ($a/c/\lambda$) | $\kappa_0 = 0.0064$ | $\kappa_1 = 0.0109 = 1.70\kappa_0$ | $\kappa_2 = 0.022 = 3.44\kappa_0$ | $\kappa_3 = 0.0156 = 2.44\kappa_0$ |
| Figure of merit FOM = $n_g\ \Delta\omega$ | 0.0162 | 0.0242 | 0.0455 | 0.0322 |

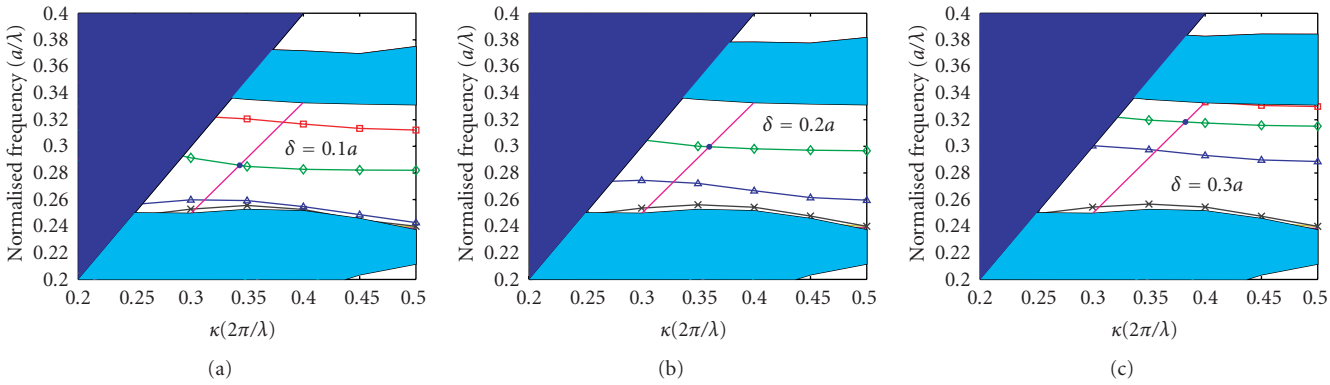


Figure 4: Band diagrams for modified PCSW. (a) $PCSW_1$ with $\delta = 0.1a$; (b) $PCSW_2$ with $\delta = 0.2a$; (c) $PCSW_3$ with $\delta = 0.3a$. Note that higher-order modes (blue curve with triangle marker and black curve with cross marker) are pulled up from the lower band edge.

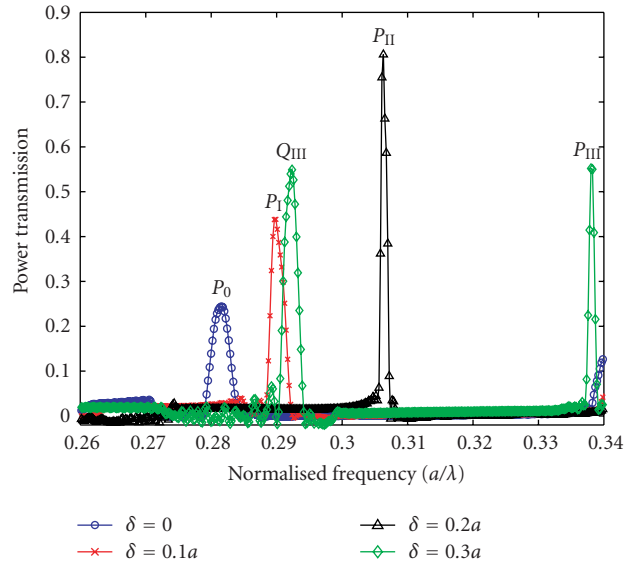


Figure 5: The transmission comparison for modified waveguides. $\delta = 0.2a$ ($P_{II}$) gives the highest peak transmission, indicating a sharp increase of coupling coefficient. When $\delta = 0.3a$, coupling with higher-order even mode ($Q_{III}$) comes into the frequency window.

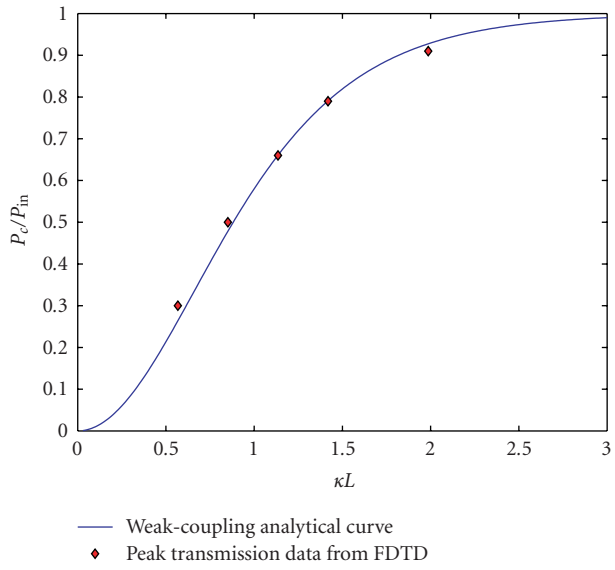


(a)

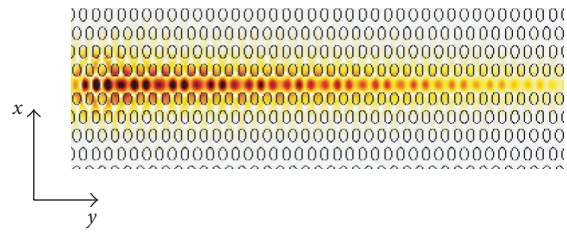


(b)

Figure 6: (a) Verification of weak-coupling (2). Only the coupling length $L$ is varied in the $PCSW_2$ case. The peak transmission data from FDTD matches the analytical curve of (2). (b) $E_x$ field profile in $PCSW_2$ generated by counter-directional coupling for $L = 40a$.

flow in the $SiO_2$-Wr above is along $+y$ direction. The power increases gradually in $PCSW_2$ along $-y$ direction.

From coupled mode theory, the coupling bandwidth $\Delta\omega$ is related to $\kappa$ and the group velocity $v_g$ of the individual waveguide modes by

$$\Delta\omega = \frac{2\kappa}{1/v_{gB} - 1/v_{gA}} = \frac{2\kappa}{n_{gB} - n_{gA}}c. \quad (3)$$

The group index of $SiO_2$-Wr mode $n_{gA}$ is 1.2, and $n_{gB}$ is the group index of PCSW mode at coupling point $P$. The first two rows of Table 1 give the comparison of peak power transmission and coupling bandwidth (full width half maximum) obtained from P3D FDTD simulations, and the third row shows the PCSW group index at the coupling point obtained from PWE method. From the second and third rows of data and (3), the coupling coefficient is calculated. In the last row, we take the figure of merit (FOM) as the product of coupling bandwidth and group index.

From Table 1 and (3), we see that there is a balance between group index and coupling bandwidth in order to

achieve optimal efficiency. Though $PCSW_3$ offers the highest group index at the coupling point, the fast reduction in the coupling bandwidth still brings down the coupling coefficient and the peak transmission. $PCSW_2$ is the preferred design with highest FOM, as well as the best coupling coefficient.

## 5. SUMMARY

To conclude, we have studied the counter-directional coupling between $SiO_2$-Wr and PCSW using P3D FDTD simulations and coupled mode analysis. It is shown that the coupling efficiency can be improved by moving the work point into the slow light region. This is achieved by changing the properties of $SiO_2$-Wr or shortening the width of PCSW. There is also a balance between the coupling bandwidth and group velocity. For $PCSW_2$, the peak power transmission is 82% over 50 lattice constants, and the group velocity is 1/35 of light speed in vacuum. $SiO_2$-Wrs offer an alternative way to couple slow light efficiently into PCSWs.

## ACKNOWLEDGMENTS

This work is supported by the Swedish Foundation for Strategic Research (SSF) through the INGVAR program, the SSF Strategic Research Center in Photonics, and the Swedish Research Council (VR).

## REFERENCES

[1] M. Notomi, K. Yamada, A. Shinya, J. Takahashi, C. Takahashi, and I. Yokohama, "Extremely large group-velocity dispersion of line-defect waveguides in photonic crystal slabs," *Physical Review Letters*, vol. 87, no. 25, Article ID 253902, 4 pages, 2001.

[2] H. Gersen, T. J. Karle, R. J. P. Engelen, et al., "Real-space observation of ultraslow light in photonic crystal waveguides," *Physical Review Letters*, vol. 94, no. 7, Article ID 073903, 4 pages, 2005.

[3] L. H. Frandsen, A. V. Lavrinenko, J. Fage-Pedersen, and P. I. Borel, "Photonic crystal waveguides with semi-slow light and tailored dispersion properties," *Optics Express*, vol. 14, no. 20, pp. 9444–9450, 2006.

[4] Y. A. Vlasov and S. J. McNab, "Coupling into the slow light mode in slab-type photonic crystal waveguides," *Optics Letters*, vol. 31, no. 1, pp. 50–52, 2006.

[5] P. Pottier, M. Gnan, and R. M. De La Rue, "Efficient coupling into slow-light photonic crystal channel guides using photonic crystal tapers," *Optics Express*, vol. 15, no. 11, pp. 6569–6575, 2007.

[6] L. Tong, R. R. Gattass, J. B. Ashcom, et al., "Subwavelength-diameter silica wires for low-loss optical wave guiding," *Nature*, vol. 426, no. 6968, pp. 816–819, 2003.

[7] W. Kuang, C. Kim, A. Stapleton, and J. D. O'Brien, "Grating-assisted coupling of optical fibers and photonic crystal waveguides," *Optics Letters*, vol. 27, no. 18, pp. 1604–1606, 2002.

[8] P. E. Barclay, K. Srinivasan, and O. Painter, "Design of photonic crystal waveguides for evanescent coupling to optical fiber tapers and integration with high-$Q$ cavities," *Journal of the Optical Society of America B*, vol. 20, no. 11, pp. 2274–2284, 2003.

[9] Efield AB http://www.efieldsolutions.com/.

[10] Z. Zhang, M. Dainese, L. Wosinski, et al., "Optical filter based on two-dimensional photonic crystal surface-mode cavity in amorphous silicon-on-silica structure," *Applied Physics Letters*, vol. 90, no. 4, Article ID 041108, 3 pages, 2007.

[11] A. Yariv, *Optical Electronics in Modern Communications*, chapter 13, Oxford University Press, New York, NY, USA, 5th edition, 1997.

Hindawi Publishing Corporation
Active and Passive Electronic Components
Volume 2007, Article ID 17692, 7 pages
doi:10.1155/2007/17692

*Research Article*

# The Structural Engineering Strategy for Photonic Material Research and Device Development

**Yalin Lu**

*The Physics Department, Laser and Optics Research Center (LORC), 2354 Fairchild Dr. 2A31, USAF Academy, CO 80840, USA*

Received 19 August 2007; Accepted 14 October 2007

Recommended by Min Qiu

A new structural engineering strategy is introduced for optimizing the fabrication of arrayed nanorod materials, optimizing superlattice structures for realizing a strong coupling, and directly developing nanophotonic devices. The strategy can be regarded as "combinatorial" because of the high efficiency in optimizing structures. In this article, this strategy was applied to grow ZnO nanorod arrays, and to develop a new multifunctional photodetector using such nanorod arrays, which is able to simultaneously detect power, energy, and polarization of an incident ultraviolet radiation. The strategy was also used to study the extraordinary dielectric behavior of relaxor ferroelectric lead titanate doped lead magnesium niobate heterophase superlattices in the terahertz frequencies, in order to investigate their dielectric polariton physics and the potential to be integrated with tunable surface resonant plasmonics devices.



## 1. INTRODUCTION

The combinatorial strategy for materials science and engineering, an experimental concept developed in the 1960s for alloy development and later for new medicine identification, has been reviving in materials science in the recent decade because of the significant advances in material synthesis amethods [1, 2]. In general, a combinatorial strategy includes the development of advanced approaches for both high-throughput material synthesis and efficient parallel characterization of those resulting multicompositional samples [3]. High-throughput syntheses include the fabrication of such combinatorial samples (so-called libraries) using various film deposition methods such as sputtering, pulsed laser deposition (PLD), inkjet delivery, and so forth, and these resulting material libraries can be binary (so-called spreadsheets) or ternary (for simulating a ternary phase diagram), in the format of either "digital" (discrete composition distribution) or "analog" (continuously varying composition). Efficient parallel characterizations require the development of very special tools [4] responding to the property of the research interest, such as structural lattice [5], dielectric constant, luminescence, loss, and so forth, which usually lag behind the high-throughput material synthesis development. Normally, such special tools are required to have capabilities of high-speed scanning and efficient data processing, while the measurement accuracy can still be maintained.

In general, high-throughput syntheses of oxide material libraries are relying on the principle of overlapping thin layers of oxide materials with different compositions as a multilayer under relatively lower synthesis temperature, and a subsequent post-annealing processing on the library will compositionally interdiffuse them into a uniformly solid-state reacted material with either a single-phase or a multiphase structure, depending on their composition stoichiometry. In recent years, this combinatorial principle has been successfully used for rapid discovery of many new materials or fine compositional tuning of oxides including phosphors [6], dielectrics [4], electro-optic materials [7], superconductors [1], and so forth. In Figure 1(a), the schematic for both binary and ternary analog libraries is depicted, which have been mainly used for identifying or fine-tuning the material composition in the past. Figure 1(b) shows the solid state reaction principle through post-annealing processing widely used for making those oxide combinatorial libraries.

Fabrication of a superlattice via alternatively stacking two structurally similar oxide materials offers a unique capability to tailor the property of the research interest via changing its

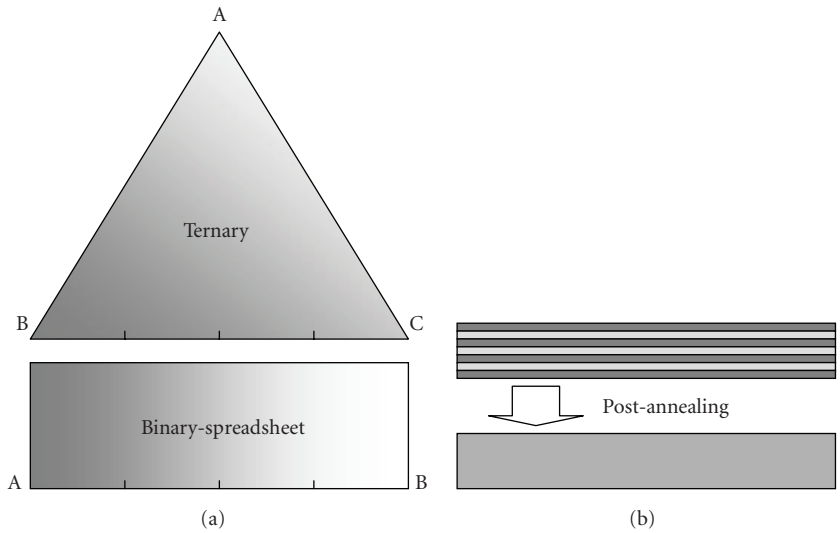


Figure 1: Schematic of ternary (upper) and binary (lower) analog combinatorial libraries (a) and the solid state reaction principle through post-annealing processing the libraries (b).

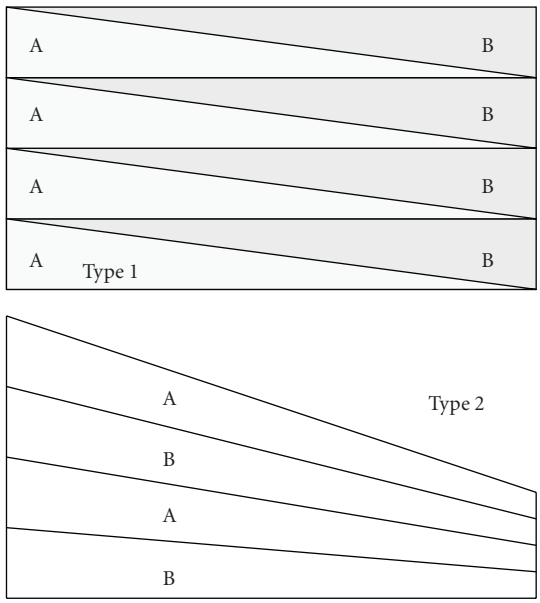


Figure 2: Schematic of two types of structural combinatorial spreadsheets: Type I and type II.

periodicity [8]. Because of the single crystalline structure of a superlattice, frequency-dependent lattice resonances (dispersion of phonons) will occur and will present resonant behaviors at certain frequencies. Such resonant frequencies are mainly determined by the superlattice periodicity and properties of those materials as layers such as piezoelectric coefficients [9]. Interaction of such phonons with incident electromagnetic (EM) radiations (photons) via energy transferring will then result in many new kinds of polaritons, which are responsible for many new and interesting physical phenomena including structurally tailorable band-edge absorption, negative refraction, tunable dielectric constant, nonlinear optics, and so forth. As one of their potential application examples, proper integration of a highly tunable dielectric superlattice with certain nanostructures such as surface resonant plasmonics may realize a large range of frequency tuning in long wavelengths, which will be useful for terahertz (THz) optics.

In this research, such a structural engineering strategy is discussed. It was applied to optimize the growth condition of ZnO nanorod arrays, to develop a new multifunctional UV photodetector using such ZnO nanorod arrays able to simultaneously distinguish power, energy, and polarization of an incident UV light. Furthermore, this strategy was used to study the dispersion behavior of new ferroelectric relaxor lead titanate doped lead magnesium niobate (PMN-PT) heterophase superlattices in the THz frequency range with a goal to investigate some new physical phenomena including the dispersion of the dielectric polaritons and their tunable behaviors. Potential application of such a strategy for negative index materials (NIM) and nonlinear optics are also slightly discussed.

## 2. THE STRUCTURAL ENGINEERING STRATEGY

The structural engineering strategy is easily applicable to cases where analog binary libraries (spreadsheets) can be fabricated. Key point to implement this strategy will be to keep the as-grown spreadsheet as a superlattice, instead of the previously discussed reacted film. This difference will result in significant challenges in fabrication. For example, post-annealing processing will be omitted in order to suppress the interdiffusion between those adjunct layers if as superlattices. Growth of each superlattice layer through atomic epitaxy is required, and the process should satisfy conditions generally required for a single crystalline epitaxy growth—lattice matching among substrate and two stacking layers, the two layers' similarity in growth characteristics, and so

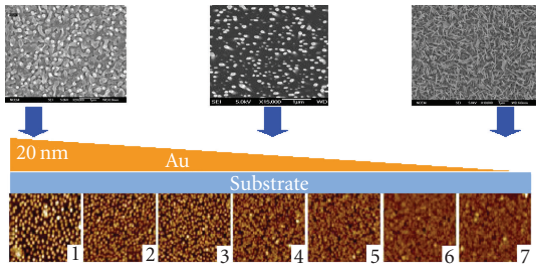


Figure 3: The spreadsheet approach used for optimizing the Au catalyst thickness for ZnO nanorod array growth.

forth. Figure 2 shows two possible formats of the analog spreadsheets: each interlayer has a linearly varying composition (Type I) and each interlayer has a linearly varying thickness (Type II). In terminology, if this strategy is used for high-throughput optimization, it can be referred as "structural combinatorial strategy," in comparison to previously mentioned compositional combinatorial strategy. Otherwise, this strategy will remain as the structural engineering strategy.

In this research, the structural engineering strategy will be used to optimize growth condition for fabricating ZnO nanorod arrays. For further making them into imaging photodetectors, ZnO nanorod arrays are required to be vertically aligned with suitable rod size and rod surface density (nanorods per surface area). The Type I structural engineering concept was used to the (Zn,Mg)O material via a pulsed laser deposition (PLD) growth. The fabricated ZnMgO/ZnO/ZnMgO quantum well (QW) spreadsheet will be integrated with a ZnO nanorod array-based photodetector [10] for simultaneously sensing energy, power, and polarization of an incident UV light, without the use of any additional wavelength dispersive components and optical polarization controller. Such new UV photodetectors can find wide applications in biology, environmental protection, and so forth, because of their compactness and cost effectiveness. The Type II strategy was used to the PMN-PT material for realizing heterophase superlattice spreadsheets fabricated by the modified chemical liquid deposition (CLD) approach [11]. "Heterophase" indicates an alternatively stacking of PMN-PT rhombohedral ($R$) and tetragonal ($T$) phases, by maintaining their average composition right at the "$R$" and "$T$" phases' morphology phase boundary (MPB) [12]. Such superlattices could present minimal interfacial strains and are then suitable for studying their polariton physics and tunable behaviors for long wavelengths.

## 3. OPTIMIZATION OF ZnO NANOROD ARRAYS

The qualities of ZnO nanorod arrays as potential photodetectors can be evaluated according to nanorod density (nanorods per area), nanorod size, size uniformity, and the degree of their vertical alignment against the substrate, and so forth. The spatial resolution for imaging will be determined by the nanorods' density, size, and uniformity. Good verticality of nanorods is also required to enhance the polar-

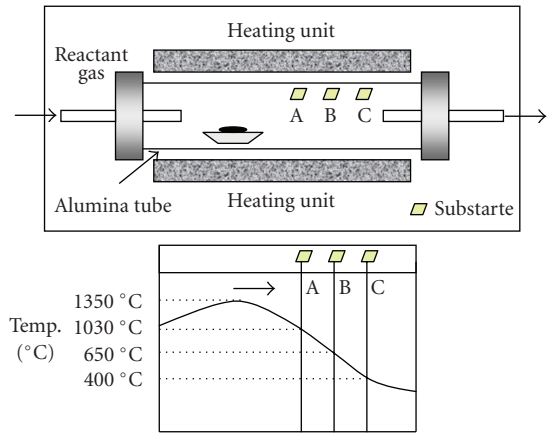


Figure 4: Schematic drawing of the CLS growth system with a gradient temperature field.

ization discrimination. In common nanorod growths, phenomena such as spiral growth of nanorods and appearance of nanowires and nanobelts can become very competitive. The growth will be determined by selecting suitable lattice matching, catalyst specie, catalyst thickness, and other processing conditions including growth temperature and catalyst postprocessing. The use of routine trying-error method will be time-consuming and inefficient. However, availability of such a structural engineering approach can solve this issue in a very effective way. In this research, this strategy was used to optimize Au catalyst's thickness, ZnO nanorod growth temperature, and so forth.

The effort to find the best suitable catalyst thickness when using gold (Au) as the catalyst material for growing ZnO nanorod arrays was performed using the (11 $\bar{2}$0) sapphire substrate. An Au thin layer, which has a varying thickness from 0 nm at one end of the spreadsheet to approximately 20 nm at the other end, was sputtered on the sapphire substrate with the help of a moving mask. ZnO nanorod arrays were grown at temperature around 900°C using a standard vapor-liquid-solid (VLS) deposition system. Figure 3 shows the SEM images of the as-grown ZnO nanorod arrays taken from different locations on the spreadsheet. Obviously, dense ZnO nanorod arrays can be obtained when the Au catalyst has a thickness from 5 to 10 nm. When the Au catalyst layer is very thin, it presents typical nanowire growth morphology. Through the use of a thicker Au catalyst layer, the nanorod growth becomes coarser.

Growth temperature optimization of those ZnO nanorods was done using approximately 5 nm thick Au-coated (11 $\bar{2}$0) sapphire wafer in a VLS system having a gradient temperature distribution, as shown in Figure 4. Through identifying the as-grown ZnO nanorods morphology on the wafer via SEM, we found that a suitable growth temperature range from 890 to 950°C. Certain controllability over size and density of ZnO nanorods has been found when selecting a proper growth temperature. Lower growth temperature tends to provide sparser and bigger nanorods. This may be understandable by the nature

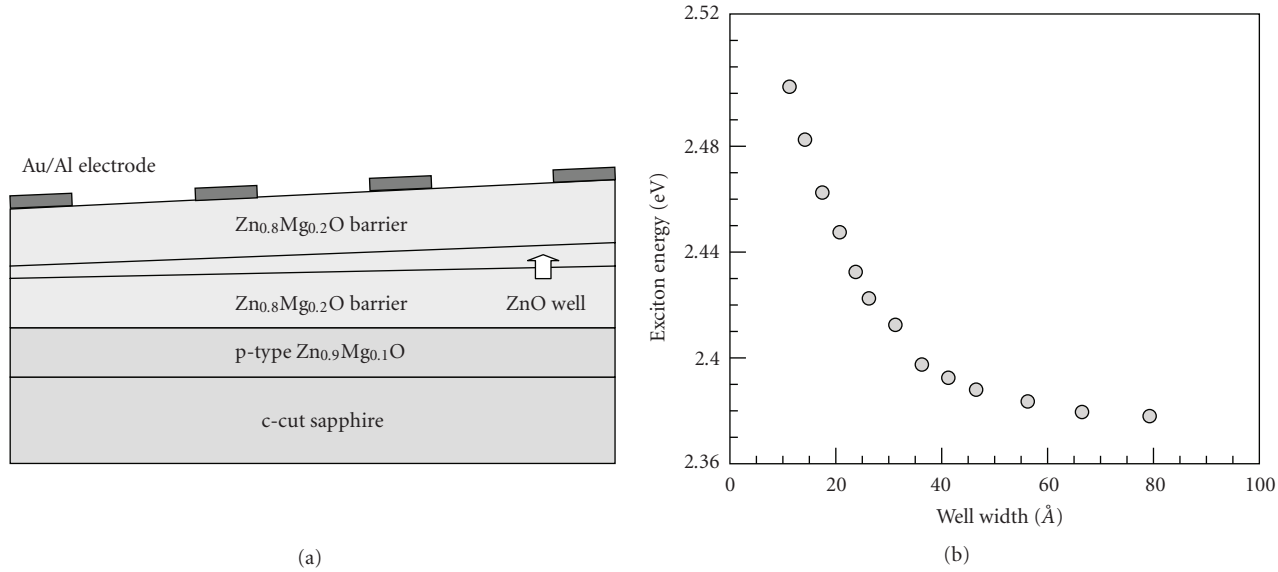


Figure 5: Wavelength distinctive UV photodetectors using a ZnMgO/ZnO/ZnMgO quantum well spreadsheet (a) and the dependence of the exciton energy on the well width (b).

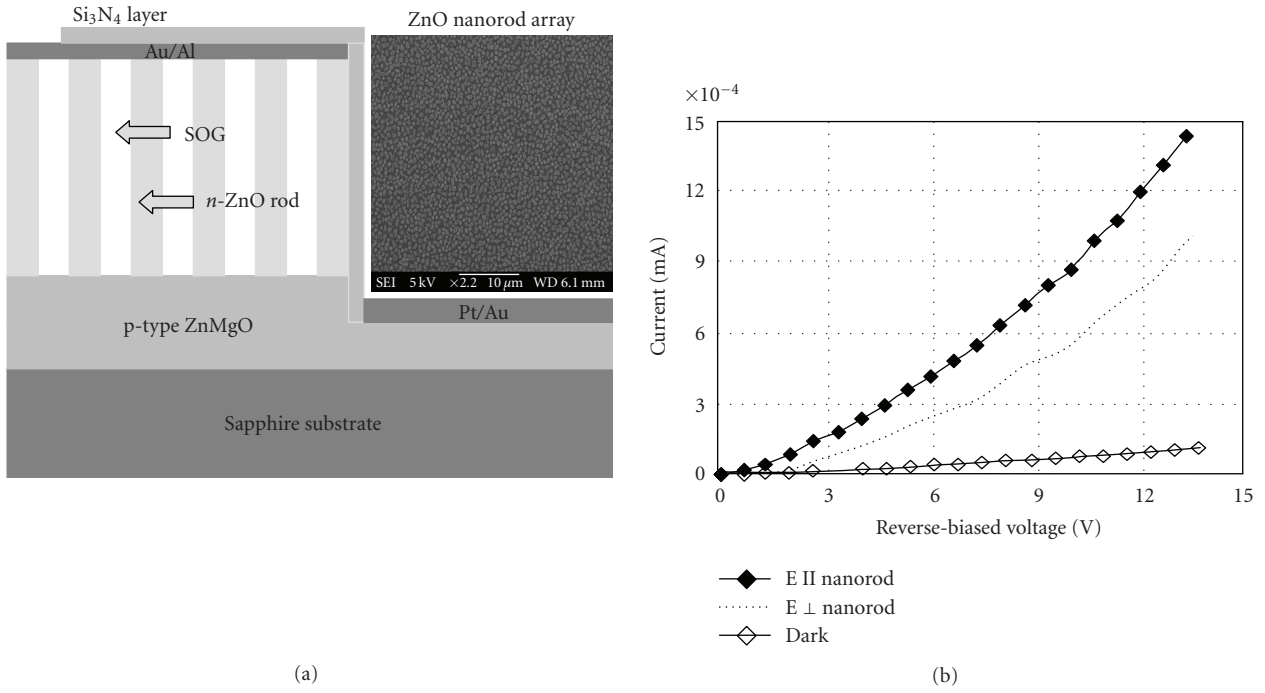


Figure 6: Power and polarization distinctive UV photodetectors using ZnO nanorod arrays grown on the $Zn_{0.9}Mg_{0.1}O$-coated $Al_2O_3$ (0001) substrate by PLD (a) and typical current-voltage measurements under dark, bright, and different polarizations (b).

of catalyst-assisted ZnO nanorod growth. At the initial stage, Zn vapor dissolves into the Au catalyst to form an alloy droplet. After reaching the saturation, Zn precipitates from the droplet and oxides as the ZnO nanorod grows [13]. During this process, the growth temperature definitely has an impact on Zn partial vapor pressure, its dissolvability into Au, and the degree of saturation, and so forth. Good controllability over nanorods size and density is required for the suggested photodetector to be discussed below, which indicates the necessary of a continuing effort along this research direction.

## 4. UV PHOTODETECTOR

With a purpose to develop a new type of UV photodetector, which can simultaneously sense power, energy, and

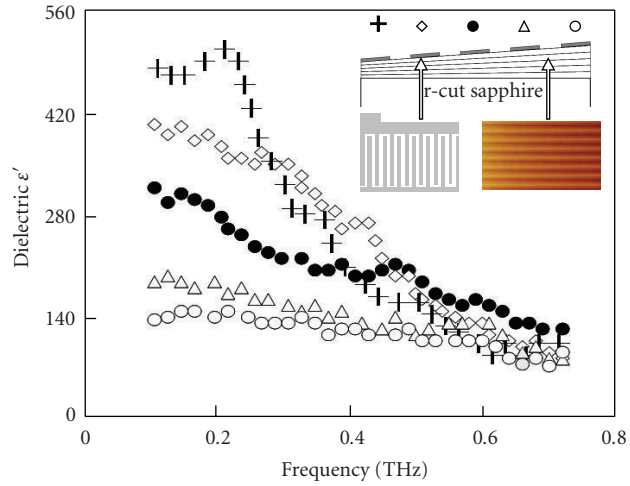


Figure 7: THz dielectric spectra of the PMN-PT heterophase superlattice spreadsheet measured by the time-domain THz measurement technique.

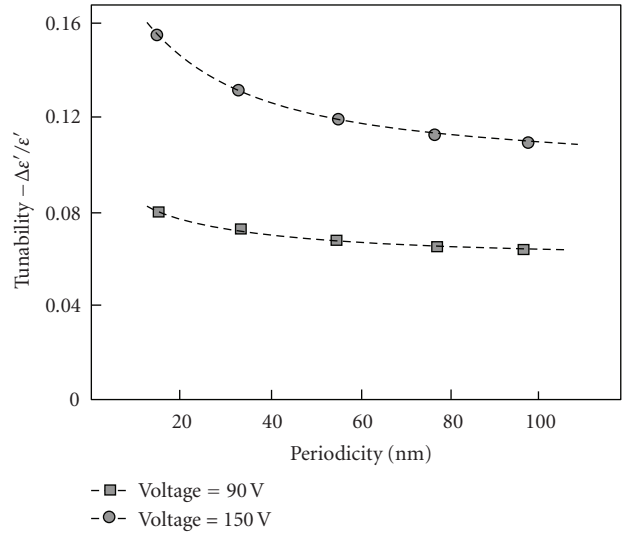


Figure 8: Dielectric tunability of the PMN-PT heterophase superlattice spreadsheet under different applied voltage of 90 V and 150 V, measured at 0.2 THz.

polarization without use of external optical components, a monolithic integration of structurally engineered ZnMgO/ZnO/ZnMgO QW spreadsheet and a well-defined ZnO nanorod array on a p-type $Zn_{0.9}Mg_{0.1}O$-coated c-cut sapphire substrate will be used. As the first part of the photodetector, the spreadsheet is intended for distinguishing wavelength (sensing wavelength). In this part, the p-type $Zn_{0.9}Mg_{0.1}O$ layer is used as a buffer layer for subsequent epitaxial growth via PLD of $Zn_{0.80}Mg_{0.2}O/ZnO/Zn_{0.80}Mg_{0.2}O$ barrier/well/barrier QW spreadsheet, and also as a bottom electrode for making an array of parallel photodetectors, when a linear array of the top Au/Al electrodes was lithographically made (Figure 5(a)). Inside the spreadsheet, both barriers aside the well and the ZnO well maintain a constant thickness ratio of 1.5 : 1, and the ZnO well thickness changes from a few Å at one end of the spreadsheet to over 80 Å at the other. In this case, an incident wavelength can be roughly determined by finding the position of the effective photodetection inside the parallel made photodetector array. Figure 5(b) shows a dependence of ZnO well exciton energy on the well width, which indicates reasonable wavelength detectivity according to the position on the linear detector array responsive to the incident wavelength.

In the second part of the UV photodetector where ZnO nanorod arrays are designed for sensing both optical power and the incident polarization status, the p-type $Zn_{0.9}Mg_{0.1}O$ layer is used to form p-n junctions with those vertically aligned n-type ZnO nanorods grown by the standard vapor-liquid-solid (VLS) deposition (Figure 6(a)), and the growth is catalyzed by a thin layer of sputtered Au (10 nm thick) [14]. Free space among ZnO nanorods was filled by sputtered spin-on-glass (SOG). n-type Au/Al contact was then made on top of ion-etched SOG, and p-type Pt/Au contact was made directly on the bare p-type $Zn_{0.9}Mg_{0.1}O$ aside the ZnO nanorod arrays. Because of the formed nanoscale p-n junctions and each nanorod's large aspect ratio responsive to different polarization statuses [15], this UV photodetector is highly sensitive to the incident UV beam's power and to its polarization status respective to the ZnO nanorod's alignment (Figure 6(b)).

## 5. PMN-PT HETEROPHASE SUPERLATTICE

In order further to demonstrate the structural engineering strategy's capability, in this section a new complex oxide heterophase superlattice was studied. This new superlattice was found with the potential to have a large dielectric tunability for THz frequencies, because of resonant dielectric polaritons associated with strong coupling between superlattice structure (phonons) and the incident electromagnetic (EM) photons.

A PMN-PT heterophase superlattice spreadsheet was made by linearly varying the dipping speed of a 10 mm wide and 50 mm long r-cut sapphire substrate during the CLD process. The periodicity of the spreadsheet changes from approximately 10 nm at one end to approximately 100 nm at the other, revealed by the SEM cross-section examination. On tope of the spreadsheet, five equally spaced interdigital Ti/Au electrodes (each has an area of $6 \times 6\,mm^2$) were lithographically fabricated (inset in Figure 7). Each interdigital electrode composes of 5 $\mu$m wide Ti/Au (25/250 nm) lines separated by 20 $\mu$m wide gaps. Dielectric behavior of such superlattices in THz range was measured using the time-domain THz technique [16], in which the transmittance in the time domain is then Fourier-transformed into an absorption spectrum in the frequency domain [17]. By subtracting the substrate's contribution, the net value then represents the anticipated dielectric spectrum. The dielectric tunability was determined by measuring the relative THz electrical field change, $[E_{THz}(V) - E_{THz}(0)]/E_{THz}(0)$, with an applied voltage, $V(t) = V_{max}\sin(2\pi\omega t)$. Here $V_{max}$ is 180 V and $\omega$ is 150 Hz. The used THz beam was limited to approximately 1 mm in diameter. All the measurements were locked at $2\omega$

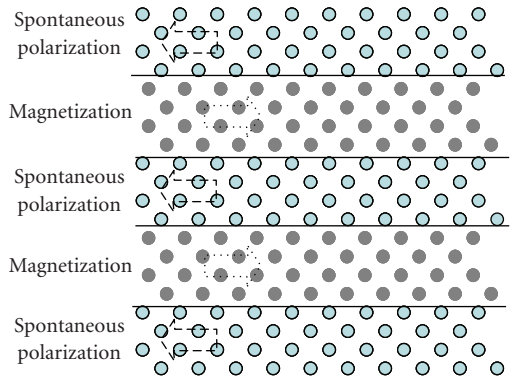


Figure 9: Schematic of the suggested piezoelectric and peizomagnetic (PE/PM) superlattice.

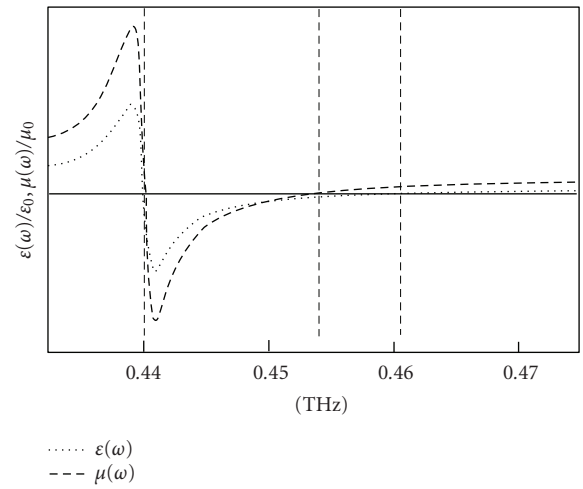


Figure 10: Simulated dielectric spectrum of a PE/PM superlattice in the terahertz frequency range.

by a lock-in amplifier at the room temperature in order to enhance the measurement sensitivity.

Figure 7 shows the THz dielectric spectra of five interdigital electrodes on the spreadsheet. It indicates a significant contribution from both polar nanoclusters relaxation and the variation of mean relaxation frequency respective to the superlattices maximum phase transition temperatures. They are strongly dependent on the interface area per superlattice volume. A small resonance peak can be seen in the spectrum from the superlattice having an average periodicity approximately 60 nm. This represents the existence of dielectric polariton close to one of the sideband resonance frequencies. Dependence of the dielectric tunability on superlattice periodicity under applied voltages of 90 V and 150 V on the spreadsheet measured at 0.2 THz is shown in Figure 8. The results indicate that smaller periodicity and higher voltage are required for achieving a larger tunability. The largest dielectric tunability in the THz frequency range reaches approximately 15%. We believe that this tunability can be further enhanced when the operation is close to the resonance frequency.

## 6. PIEZOELECTRIC AND PIEZOMAGNETIC SUPERLATTICE

Figure 9 suggests a novel piezoelectric and piezomagnetic (PE/PM) superlattice, in which the interaction between photons and phonons has a possibility to present a frequency range having both permittivity and permeability negative, so-called negative index materials (NIMs) [18]. This frequency range usually occurs immediately after the main resonance band or other sidebands (Figure 10). The structural engineering (combinatorial) strategy can be very useful in locating those resonance frequencies in actual superlattice materials, which are usually hard to be identified because of the lack of knowledge of material parameters of those complex oxides. Without knowing those material parameters with certain accuracies, simulations can only provide very approximated results.

The structural engineering strategy can also be useful for identifying new nonlinear optical (NLO) materials if the structural engineering is simultaneously associated with intentionally ordering the spontaneous polarizations inside ferroelectric materials [19]. This opens up the potential to explore either extraordinarily large optical nonlinearity or new phase matching approach.

## 7. CONCLUSION

A structural engineering (combinatorial) strategy was introduced, and was used to fabricate highly integrated UV photodetectors with multifunctioning capabilities and to study dielectric polaritons frequency behaviors of PMN-PT heterophase superlattices. Effort in this research not only indicates the high efficiency of the structural engineering (combinatorial) strategy, but also its wide applicability to versatile new research areas of current interests.

## ACKNOWLEDGMENT

The author acknowledges the support from the United States Air Force Office of Scientific Research (AFOSR) and the Air Force Research Laboratories (AFRL) at both Wright Patterson and Kirtland.

## REFERENCES

[1] X.-D. Xiang, X. Sun, G. Briceño, et al., "A combinatorial approach to materials discovery," *Science*, vol. 268, no. 5218, pp. 1738–1740, 1995.

[2] I. Takeuchi, J. Lauterbach, and M. J. Fasolka, "Combinatorial materials synthesis," *Materials Today*, vol. 8, no. 10, pp. 18–26, 2005.

[3] X.-D. Xiang and I. Takeuchi, *Combinatorial Materials Synthesis*, Marcel Dekker, New York, NY, USA, 2003.

[4] Y. Lu, T. Wei, F. Duewer, et al., "Nondestructive imaging of dielectric-constant profiles and ferroelectric domains with a scanning-tip microwave near-field microscope," *Science*, vol. 276, no. 5321, pp. 2004–2006, 1997.

[5] F. Tsui and Y. S. Chu, "The combinatorial approach: a useful tool for studying epitaxial processes in doped magnetic semiconductors," *Macromolecular Rapid Communications*, vol. 25, no. 1, pp. 189–195, 2004.

[6] J. Wang, Y. Yoo, C. Gao, et al., "Identification of a blue photoluminescent composite material from a combinational library," *Science*, vol. 279, no. 5357, pp. 1712–1714, 1998.

[7] J. Li, F. Duewer, C. Gao, H. Chang, X.-D. Xiang, and Y. Lu, "Electro-optic measurements of the ferroelectric-paraelectric boundary in $Ba_{1-x}Sr_xTiO_3$ materials chips," *Applied Physics Letters*, vol. 76, no. 6, pp. 769–771, 2000.

[8] Y. Lu, "Dielectric and ferroelectric behaviors in $Pb(Mg_{1/3}Nb_{2/3})O_3$-$PbTiO_3$ rhombohedral/tetragonal superlattices," *Applied Physics Letters*, vol. 85, no. 6, pp. 979–981, 2004.

[9] Y.-Q. Lu, Y.-Y. Zhu, Y.-F. Chen, S.-N. Zhu, N.-B. Ming, and Y.-J. Feng, "Optical properties of an ionic-type phononic crystal," *Science*, vol. 284, no. 5421, pp. 1822–1824, 1999.

[10] Y. Lu, I. A. Dajani, and R. J. Knize, "ZnO nanorod arrays as p-n heterojunction ultraviolet photodetectors," *Electronics Letters*, vol. 42, no. 22, pp. 1309–1310, 2006.

[11] Y. Lu, G.-H. Jin, M. Cronin-Golomb, et al., "Fabrication and optical characterization of $Pb(Mg_{1/3}Nb_{2/3})O_3$-$PbTiO_3$ planar thin film optical waveguides," *Applied Physics Letters*, vol. 72, no. 23, pp. 2927–2929, 1998.

[12] Y. Lu and R. J. Knize, "Enhanced dielectric and electro-optic effects in relaxor oxide heterostructured superlattices," *Journal of Physics D*, vol. 37, no. 17, pp. 2432–2436, 2004.

[13] X. Liu, X. Wu, H. Cao, and R. P. H. Chang, "Growth mechanism and properties of ZnO nanorods synthesized by plasma-enhanced chemical vapor deposition," *Journal of Applied Physics*, vol. 95, no. 6, pp. 3141–3147, 2004.

[14] Y. Lu, I. A. Dajani, W. J. Mandeville, R. J. Knize, and S. S. Mao, "New p-n junction photodetector using optimized ZnO nanorod array," *Solid State Phenomena*, vol. 121-123, p. 809, 2006.

[15] Z. Fan, P.-C. Chang, J. G. Lu, et al., "Photoluminescence and polarized photodetection of single ZnO nanowires," *Applied Physics Letters*, vol. 85, no. 25, pp. 6128–6130, 2004.

[16] P. C. M. Planken and H. J. Bakker, "Towards time-resolved THz imaging," *Applied Physics A*, vol. 78, no. 4, pp. 465–469, 2004.

[17] P. Kužel, F. Kadlec, H. Němec, R. Ott, E. Hollmann, and N. Klein, "Dielectric tunability of $SrTiO_3$ thin films in the terahertz range," *Applied Physics Letters*, vol. 88, no. 10, Article ID 102901, 3 pages, 2006.

[18] J. B. Pendry, "Negative refraction makes a perfect lens," *Physical Review Letters*, vol. 85, no. 18, pp. 3966–3969, 2000.

[19] Y. Lu, L. Mao, S.-D. Cheng, N.-B. Ming, and Y.-T. Lu, "Second-harmonic generation of blue light in $LiNbO_3$ crystal with periodic ferroelectric domain structures," *Applied Physics Letters*, vol. 59, no. 5, pp. 516–518, 1991.